DISSERTAÇÃO DE MESTRADO

IDENTIFICATION OF CONSTITUTIVE PARAMETERS BY USING FULL-FIELD MEASUREMENTS: AN EXAMPLE OF APPLICATION TO AN ELASTOPLASTIC DAMAGE MODEL

PAULO BASTOS DE CASTRO

FLORIANÓPOLIS

2012

Paulo Bastos de Castro

IDENTIFICATION OF CONSTITUTIVE PARAMETERS BY USING FULL-FIELD MEASUREMENTS: AN EXAMPLE OF APPLICATION TO AN ELASTOPLASTIC DAMAGE MODEL

IDENTIFICAÇÃO DE PARÂMETROS CONSTITUTIVOS BASEADA NA MEDIÇÃO DE CAMPOS DE DESLOCAMENTOS: EXEMPLO DE APLICAÇÃO PARA UM MODELO DE DANO ELASTOPLÁSTICO

Dissertação submetida à
Universidade Federal de Santa Catarina
como parte dos requisitos para a
obtenção do grau de
Mestre em Engenharia Mecânica.
Orientador:
Prof. D. Sc. Eduardo Alberto Fancello
Coorientador:
Prof. Dr. Eng. Jakson Manfredini Vassoler

Florianópolis

2012

Ficha de identificação da obra elaborada pelo autor,
através do Programa de Geração Automática da Biblioteca Universitária da UFSC.

Castro, Paulo Bastos de
Identification of constitutive parameters by using full-field measurements: an example of application to an elastoplastic damage model=Identificação de parâmetros constitutivos baseada na medição de campos de deslocamentos: exemplo de aplicação para um modelo de dano elastoplástico [dissertação] / Paulo Bastos de Castro ; orientador, Eduardo Alberto Fancello ; co-orientador, Jakson Manfredini Vassoler. - Florianópolis, SC, 2012.
134 p. ; 21cm

Dissertação (mestrado) - Universidade Federal de Santa Catarina, Centro Tecnológico. Programa de Pós-Graduação em Engenharia Mecânica.

Inclui referências

1. Engenharia Mecânica. 2. Identificação de parâmetros constitutivos. 3. Dano elastoplástico. 4. Correlação de imagens digitais. 5. Medição de campos de deslocamentos. I. Fancello, Eduardo Alberto. II. Vassoler, Jakson Manfredini. III. Universidade Federal de Santa Catarina. Programa de Pós-Graduação em Engenharia Mecânica. IV. Título.

Paulo Bastos de Castro

IDENTIFICAÇÃO DE PARÂMETROS CONSTITUTIVOS BASEADA NA MEDIÇÃO DE CAMPOS DE DESLOCAMENTOS: EXEMPLO DE APLICAÇÃO PARA UM MODELO DE DANO ELASTOPLÁSTICO

Esta Dissertação foi julgada adequada para obtenção do Título de Mestre em Engenharia Mecânica, Área de concentração Análise & Projeto Mecânico, e aprovada em sua forma final pelo Programa de Pós-Graduação em Engenharia Mecânica da Universidade Federal de Santa Catarina.

Florianópolis, 18 de Junho de 2012

Prof. Júlio César Passos, Dr.
Coordenador do Curso

Banca Examinadora:

Prof. Eduardo Alberto Fancello, D. Sc.
Orientador
Universidade Federal de Santa Catarina

Prof. Rogério José Marczak, Dr. Eng.
Universidade Federal do Rio Grande do Sul

Prof. Armando Albertazzi Gonçalves Jr., Dr. Eng.
Universidade Federal de Santa Catarina

Prof. Clovis Sperb de Barcellos, Ph.D
Universidade Federal de Santa Catarina

Aos meus pais.

AGRADECIMENTOS

Inicialmente gostaria de agradecer ao Prof. Eduardo A. Fancello por sua orientação; inestimável contribuição à minha formação acadêmica e profissional.

Também gostaria de agradecer ao Prof. Jakson M. Vassoler por sua colaboração na revisão do texto, suas sugestões e sua orientação na execução de meus experimentos com o método de Correlação de Imagens Digitais.

Agradeço aos professores Rogério José Marczak, Armando Albertazzi Gonçalves Jr. e Clovis Sperb de Barcellos por aceitarem participar da banca examinadora desta dissertação; e por suas valiosas observações, correções e sugestões.

Sou grato a todos aqueles do Departamento de Engenharia Mecânica e POSMEC da Universidade Federal de Santa Catarina que contribuiram direta ou indiretamente para a realização deste trabalho, em especial, aos professores do Grupo de Análise e Projeto Mecânico (GRANTE).

Agradeço à Coordenação de Aperfeiçoamento de Pessoal de Nível Superior (CAPES) pelo amparo financeiro por meio de concessão de bolsa de estudo.

Agradeço a Armin Sonnenhohl e Luiz Botega por sua assistência durante meus experimentos.

Finalmente, eu gostaria de agradecer aos meus colegas de laboratório pela amizade, pelos momentos compartilhados nos intervalos para o cafezinho e almoço, e pelo convívio durante os últimos dois anos.

RESUMO

A identificação de parâmetros constitutivos é usualmente realizada através da minimização de uma função objetivo, função essa que considera a diferença (erro) entre valores calculados numericamente e aqueles obtidos experimentalmente. Embora, em geral, apenas a força total registrada em testes uniaxiais de tração e/ou compressão seja utilizada no cálculo do erro, alguns autores têm incluido dados adicionais provenientes de medições completas de campos de deslocamento e/ou deformação. Como consequência desse fato, o Método de Correlação de Imagens Digitais (do inglês *Digital Image Correlation*, DIC) tem sido amplamente empregado como uma impotante ferramenta nesse processo devido a sua capacidade de fornecer medidas confiáveis de campos de deslocamento e/ou deformação. Nesse trabalho é proposto um método de identificação que faz uso de campos de deslocamento obtidos por meio de DIC. Tal método consiste no cálculo da energia de deformação interna e das forças internas, a cada passo de tempo, diretamente do campo de deslocamanto obtido por meio do método DIC. Dessa forma, uma função objetivo baseada no erro, a qual quantifica a diferença entre as forças internas e o carregamento medido, pode ser definida. Essa função objetivo é então minimizada em relação aos parâmetros constitutivos do material. A fim de avaliar tal proposição, vários testes de identificação de parâmetros foram realizados por meio de experimentos numéricos e mecânicos. Sendo que, nesse último caso, um corpo de prova não padronizado e fabricado em aço baixo-carbono foi projetado e submetido a um ensaio de tração monotônico. Durante esse teste, o histórico do campo de deslocamento foi registrado por meio do método DIC. Devido às características do material, a versão simplificada do modelo de Lemaitre para dano-elastoplástico foi escolhida como modelo constitutivo a ser empregado. Finalmente, duas funções objetivo foram definidas e então minimizadas por meio de um algoritmo de otimização, o que levou à solução do problema de identificação. A seção de resultados mostra o desempenho e aplicabilidade do procedimento descrito. As vantagens, dificuldades e propostas para trabalhos futuros são então discutidas.

Palavras-chave: identificação, parâmetros de materiais, problema inverso, medidas de campos de deslocamento, correlação de imagens digitais, DIC, elementos finitos, dano.

ABSTRACT

The identification of material parameters is usually accomplished through the minimisation of an objective function that takes into account the error between computed and measured quantities. Although, in general, only the total force of a tensile and/or compression test is used in the calculation of the error, several authors have included additional data, obtained from full-field measurements. As a consequence of this fact, the Digital Image Correlation (DIC) method has been widely employed as an important tool in this process, due to its capacity of supplying reliable displacement and/or strain fields. In this work, an identification method that uses the full-field data obtained by means of DIC is proposed. The internal strain energy and internal forces at each time step is calculated directly from the displacement field supplied by the DIC method. Thus, an error-based objective function that quantifies the difference between internal forces and measured loads can be defined. This objective function is then minimised with respect to the constitutive material parameters. In order to assess this proposition, several identification tests were carried out by means of numerical and mechanical experiments. In the latter, a non-standard low-carbon steel specimen was designed and submitted to a uniaxial monotonic tensile test. During the test, the history of the displacement field was recorded by means of DIC. Due to the characteristics of the material, the simplified version of Lemaitre's elatoplastic damage model was chosen as the constitutive model for the simulations. Finally, two objective functions were defined and called within an optimisation algorithm, which led to the solution of the identification problem. The results section shows the performance and applicability of the procedure described. Advantages, difficulties and proposals for future work are then discussed.

Keywords: identification, material parameters, inverse problem, full-field measurement, digital image correlation, DIC, finite element, damage.

LIST OF FIGURES

LIST OF TABLES

SYMBOLS

$\boldsymbol{\tau}$	Stress field based on a set of admissible fields
$\hat{\mathbf{u}}$	Experimentally measured displacement field
$\boldsymbol{\varepsilon}(\cdot)$	Strain field
$\mathbf{C}$	Elasticity tensor
$\mathbf{u}$	Displacement vector field
$\boldsymbol{\sigma}$	Admissible stress field, Cauchy stress tensor
$\mathbb{C}$	Set of admissible elasticity tensors
$\mathcal{K}$	Set of admissible displacement
$\mathcal{S}$	Set of admissible stresses
$\delta\mathbf{u}$	Admissible virtual field
$\mathbf{u}^t$	Discrete equilibrium displacement (history)
$\boldsymbol{\varepsilon}^t$	Discrete equilibrium strain (history)
$\mathbf{t}$	Surface traction
$A(x)$	Scalar field that modifies a reference tensor
$\mathbf{C}_0$	Reference elasticity tensor
$d(x)$	Damage field
A^e	Constant scalar field over a finite element
$\mathbf{K}^e$	Stiffness matrix of a finite element
$\mathbf{K}_0^e$	Reference stiffness matrix of a finite element
$\mathbf{u}^e$	Vector of DOFs of a finite element
E^e	A finite element
$\boldsymbol{e}_m$	m-th unit vector
$(\cdot)^T$	Transpose of a vector, matrix or tensor
$\boldsymbol{a}$	Logarithm form of A^e
$\mathbf{M}$	Matrix dependent on the measured displacement field
$\boldsymbol{q}$	Vector dependent on the measured displacement field
$\mathbf{W}$	Weighting matrix
d	Scalar damage variable
A_0	Original area without voids
A	Damaged area, i.e. an area with voids
σ	Scalar true stress
σ_{eff}	Scalar effective stress
$\mathscr{B}$	Generic body
Ω	Open region on Euclidean space
Γ	Regular boundary
ρ	Density (mass per volume)
$\nabla\cdot(\cdot)$	Divergence operator

$\mathbf{b}$	Body force (force per unit volume)
$\mathbf{n}$	Outward unit vector normal to a surface
e	Specific internal energy
$\boldsymbol{D}$	Rate of deformation tensor
r	Density of heat production
$\mathbf{q}$	Heat flux vector
s	Specific entropy
θ	Absolute temperature
ψ	Helmholtz free energy per unit mass
$\boldsymbol{\varepsilon}$	Infinitesimal strain tensor
$\boldsymbol{\varepsilon}^e$	Elastic contribution of the infinitesimal strain tensor
$\boldsymbol{\varepsilon}^p$	Plastic contribution of the infinitesimal strain tensor
$\breve{\varepsilon}^p$	Damage accumulated plastic strain
$\mathbf{X}$	Back strain tensor
ψ^e	Elastic-damage contribution of the free energy potential
ψ^p	Plastic contribution of the free energy potential
$\bar{\rho}$	Reference mass density
$\mathbf{C}^e$	Isotropic elastic tensor
Y	Thermodynamic conjugate force related to the damage variable d, $-Y$ is the energy density release rate due to damage
q	von Mises effective stress
$\mathbf{s}$	Deviatoric stress tensor
$\mathbf{I}$	Second-order identity tensor
p	Hydrostatic stress
E	Young's modulus
ν	Poisson ratio
G	Shear Modulus
K	Bulk Modulus
ψ^I	Isotropic contribution of the plastic free energy potential
ψ^K	Kinematic contribution of the plastic free energy potential
κ	Conjugate force related to isotropic hardening
$\boldsymbol{\beta}$	Conjugate force related to kinematic hardening (back-stress tensor)
Φ	Yield function related to Lemaitre's damage model
σ_y	Hardening function
J_2	Second stress deviator invariant
σ_{y0}	Uniaxial yield stress of a virgin material
k	Material constant
n	Material constant

Ψ	Flow potential
a	Material constants related to Armstrong-Frederick's model
b	Material constants related to Armstrong-Frederick's model
r	Material constants related to damage evolution
S	Material constants related to damage evolution
$\boldsymbol{N}$	Flow vector
$\dot{\gamma}$	Damage-pasric rate multiplier
$(\cdot)_n$	Current state
$(\cdot)_{n+1}$	Updated state
$(\cdot)^{trial}$	Trial condition
$\Delta\gamma$	Algorithm counterpart of the damage-plastic multiplier
$\tilde{p}$	Effective hydrostatic stress
$\tilde{s}$	Effective deviatoric stress
$\tilde{q}$	Effective von Mises equivalent stress
$F(\Delta\gamma)$	Single-equation return-mapping function
ω	Material integrity $= 1 - d$
$\mathbf{I}_\mathrm{d}$	Fourth-order deviatoric projection tensor
$\bar{\mathbf{s}}_{n+1}$	Normalised stress deviator
M	Number of pixels
C_{ZNCC}	Zero-Nomalized Cross-Correlation
C_{ZNSSD}	Zero-Nomalized Sum of Squared Differences
$f(x_i, y_j)$	Grey intensity in a reference subset
$g(x'_i, y'_j)$	Grey intensity in a deformed subset
(x_i, y_j)	Coordinates of subset pixels before deformation
(x'_i, y'_j)	Coordinates of subset pixels after deformation
f_m	Mean value of grey intensity in a reference subset
g_m	Mean value of grey intensity in a deformed subset
Δf	Normalised value of grey intensity in a reference subset
Δg	Normalised value of grey intensity in a deformed subset
ξ	Mapping function x-direction
η	Mapping function y-direction
Δx	Coordinate variation in x-direction
Δy	Coordinate variation in y-direction
(x_0, y_0)	Coordinate of the centre of a subset (marker)
$\mathbf{p}$	Vector of variables
u	Displacement in x-direction
v	Displacement in y-direction
$\mathbf{p}_0$	Initial guess for a vector of variables $\mathbf{p}$
f_C	Correlation function

$\nabla(\cdot)$	First-order partial derivatives with respect to the unknown parameters $\mathbf{p}$
$\nabla^2(\cdot)$	Second-order partial derivatives with respect to the unknown parameters $\mathbf{p}$
ε_z	Out-of-plane strain
$\mathrm{t}(\varepsilon_x, \varepsilon_y)$	Thickness function
t_0	Initial thickness
ε_x	In-plane strain component x-direction
ε_y	In-plane strain component y-direction
u_z	Out-of-plane displacement
δR	Residual (Virtual work equilibrium)
δF	Internal virtual work
δQ	External virtual work
$\mathcal{V}$	Set of virtual displacements
Ω^t	Deformed configuration
∇^s	Symmetric gradient
$\mathbf{x}$	Spatial coordinates in the deformed configuration
$\mathbf{N}$	Finite element shape fuction
NDOF	Number of degrees of freedom.
$\mathbf{R}$	Residual Vector
$\mathbf{F}$	Vector of internal forces
$\mathbf{Q}$	Vector of external forces
$\mathbf{B}$	Matrix containing the strain associated with $\mathbf{N}$
$\mathcal{D}$	Strain operator
Ω_0	Reference (Undeformed) configuration
Ψ	Objective function
$\mathbf{p}^\star$	Vector of minimising variables
$\mathcal{P}$	Set of admissible values of material parameters
Γ^T	Set of nodes on the top egde of an ROI
Γ^B	Set of nodes on the bottom egde of an ROI
Γ^L	Set of nodes on the left egde of an ROI
Γ^R	Set of nodes on the right egde of an ROI
Γ^A	Set of nodes on the surface of an ROI
P^t	External force measured at time t
α_i^t	Weighting parameter
Γ^i	Set of nodes on the top-boundary of a row of elements
nip	Number of integration points
$\mathbf{f}^e$	Element's internal force vector
H	Slope of the hardening function

$\mathbf{I}_{\mathrm{S}}$	Fourth-order symmetric identity tensor
δ_{ik}	Krönecker delta
$\{s_k\}$	Sequence of points $\{(u_k, t_k)\}$
u_k	Displacement of a marker at the time t_k
s_n	Subsequence of $\{s_k\}$
$u_k^\star$	Smoothed value of u_k
χ_n	Sets of nodes defined in a grid of markers, where n is the number of nodes in the set
$u_{(i,j)}^\star$	Smoothed displacement of $u_{(i,j)}$

CONTENTS

1 INTRODUCTION

The development of increasingly sophisticated constitutive models, appropriate to simulate the thermo-mechanical behaviour of a vast range of new materials, has brought about the necessity of new numerical techniques. These techniques are able to extract suitable information from mechanical tests. This information usually consists of a set of constants, frequently called *material parameters* or *constitutive parameters*. These parameters sometimes have a mechanical significance and are easily related to a particular experiment (e.g. elasticity modulus or Poisson ratio). However, they frequently have more obscure or non mechanical meanings (e.g. the parameters of Ogden's hyperelasticity model).

In the simplest cases, analytical equations, such as uniaxial stress-strain relationships, are commonly employed to fit experimental data. Thus, linear or nonlinear regression schemes may be successfully employed. However, when the phenomenon to be represented increases in complexity, as a result of nonlinear effects, finite strains, anisotropy, history dependence, etc simple mechanical tests might not be appropriate for the identification of parameters of the corresponding material models. As a consequence, two complementary approaches are currently employed: the execution of a higher number of different tests, and the use of experimental techniques that provide more and improved information from a single test. Full-field measurements techniques like Digital Image Correlation (DIC) and interferometric ones are able to offer the whole displacement and/or strain field in an observable region of a sample. This is of major interest in many cases, like for example the observation of a necking process in a tensile test, where highly non homogeneous strains are present. An immediate consequence of this data availability is the search for appropriate techniques capable of processing the acquired information and identifying the material parameters of the chosen representation model.

In the present work a particular method is proposed and tested, for the identification of constitutive material parameters, making use of data provided by full-field measurements. Elastic and plastic strains as well as damage are the mechanical phenomena in focus, represented here with Lemaitre's classic elastoplastic damage model [1, 2].

1.1 IDENTIFICATION OF MATERIAL PARAMETERS

Several approaches can be employed to deal with the identification of material parameters, which are also referred to as techniques for inverse problems. A huge group of these methods is based on the minimisation of the difference between experimental and the corresponding data which are produced by means of the constitutive model. Clearly, different quantities may be compared. The most usual is the force or history of force recorded during experiments, compared to the force produced by the model for a given known displacement. Conversely, the comparison between experimental and modelled displacement (or its history) is frequently given for a known applied load. Such data are frequently made available by carrying out many experiments or by extracting as much information as possible from a single one.

The increasing use of non-contact and optical measurement techniques has expanded the possibilities for new identification procedures, mainly due to their ability to handle non homogeneous strain fields. Since the information retrieved is not a single value but a whole field over a region, it enhances the quality and quantity of the experimental data even for a single experimental test.

On the other hand, constitutive models have progressively become more and more sophisticated, frequently at the cost of an increasing number of material parameters, many times with no clear mechanical interpretation.

This scenario points to the need to improve the available identification techniques in order to explore the opportunities offered by the full-field measurements and its association with present and forthcoming constitutive laws.

In the next section, a brief review of different techniques developed, which take advantage of full-field optical measurements, is presented. Most of this review is based on article [3] and references therein. Many of these references can be understood as a theoretical framework in which different operational techniques can be cast. The present study proposes a possible identification technique that may be classified, from a theoretical point of view, within one of the reviewed techniques.

1.2 IDENTIFICATION METHODS BASED ON FULL-FIELD MEASUREMENTS

1.2.1 Finite Element Model Updating

The Finite Element Model Updating (FEMU) is one of the commonest class of methods employed in the identification of constitutive parameters. This method can be summarised as follows. Given the experimental data, e.g. the field of displacements and the total force applied, the equivalent ones are obtained by simulation with a model that depends on the material parameters. The minimisation of an error function that measures the difference between experimental and simulated data with respect to a set of unknown parameters, completes the identification operation.

Two of the most important features of this approach are simplicity and flexibility. For this reason, this method is suitable for almost any case related to the identification of constitutive parameters. Another relevant aspect of this method is that the sets of experimental and simulated data are both independently acquired. Furthermore, there are no limitations on characteristics or, on the complexity of the model to be evaluated. On the other hand, such positive features, which allow this method to be employed in a wide range of applications, may lead to relatively large computational costs. For instance, the computation of a single value of the objective function requires a whole simulation of the experimental test which is generally nonlinear and possibly incremental in time. As examples of the use of this technique see [4, 5]

1.2.2 Constitutive Equation Gap Method

The Constitutive Equation Gap Method (CEGM) measures the distance between a given stress field $\boldsymbol{\tau}$ and another stress field. The latter is computed from a measured (history of) displacement field by using a constitutive equation. Proposed within the context of linear elasticity [6, 7], the constitutive equation gap (CEG) is defined as

$$\mathscr{E}\left(\hat{\mathbf{u}}, \boldsymbol{\tau}, \mathbf{C}\right) = \frac{1}{2}\int_{\Omega} \left[\boldsymbol{\tau} - \mathbf{C} : \boldsymbol{\varepsilon}(\hat{\mathbf{u}})\right] : \mathbf{C}^{-1} : \left[\boldsymbol{\tau} - \mathbf{C} : \boldsymbol{\varepsilon}(\hat{\mathbf{u}})\right] \mathrm{d}V \qquad (1.1)$$

where $\hat{\mathbf{u}}$ is an experimentally measured displacement field and $\boldsymbol{\varepsilon}(\cdot)$ is the corresponding strain field, while $\mathbf{C}$ is the elasticity tensor dependent on the material parameters. Again, in the context of linear elasticity, $\mathbf{u}$ and $\boldsymbol{\sigma}$ are the arguments of the following minimisation problem [3]

$$
\begin{aligned}
(\mathbf{u},\boldsymbol{\sigma}) &= \underset{(\hat{\mathbf{u}},\boldsymbol{\tau})\in\mathcal{K}\times\mathcal{S}}{\arg\min}\ \mathscr{E}(\hat{\mathbf{u}},\boldsymbol{\tau},\mathbf{C}) \quad , \\
\mathscr{E}(\mathbf{u},\boldsymbol{\sigma},\mathbf{C}) &= 0 \, , \qquad (1.2)
\end{aligned}
$$

and the identification of the material constants present in the elasticity tensor $\mathbf{C}$ comes from the following minimisation procedure

$$
\begin{aligned}
\mathbf{C} &= \underset{\mathbf{C}^\star\in\mathbb{C}}{\arg\min}\, \mathscr{F}(\mathbf{C}^\star) \ \text{ with} \\
\mathscr{F}(\mathbf{C}^\star) &= \min_{(\hat{\mathbf{u}},\boldsymbol{\tau})\in\mathcal{K}\times\mathcal{S}} \mathscr{E}(\hat{\mathbf{u}},\boldsymbol{\tau},\mathbf{C}^\star) \ . \qquad (1.3)
\end{aligned}
$$

In (1.3) $\mathbb{C}$ is the set of admissible elasticity tensors, $\mathcal{K}$ is the set of admissible displacement, and $\mathcal{S}$ is the set of admissible stresses. This implies a constrained minimisation problem (equality constraints) that may be enforced by Lagrange multipliers or penalisation.

The extension of this method to nonlinear problems is addressed in [8], among others.

1.2.3 Virtual Field Method

The Principle of Virtual Work consists of finding the stress field $\boldsymbol{\sigma}$ that satisfies the virtual work balance [1]

$$
\int_\Omega \boldsymbol{\sigma} : \boldsymbol{\varepsilon}(\delta\mathbf{u})\, \mathrm{d}\Omega = \int_\Gamma \mathbf{t}\cdot\delta\mathbf{u}\, \mathrm{d}\Gamma \qquad (1.4)
$$

for any admissible virtual field $\delta\mathbf{u}$. Conventional Finite Element Method uses this balance equation, the constitutive and kinematic equations in order to identify the appropriate discrete equilibrium displacement (history) $\mathbf{u}^t$.

The Virtual Field Method (VFM) proposes using the measured displacement or strain within the appropriate constitutive model to compute the stresses: $\boldsymbol{\sigma} = \boldsymbol{\sigma}(\boldsymbol{\varepsilon}^t)$. If the constitutive model is endowed with the appropriate parameters, the stresses should equilibrate the external forces $\mathbf{t}$ and Eq. (1.4) would be satisfied.

This proposition allows different operational approaches, depending

---

[1] For the sake of simplicity, we assume that body forces are not applied.

on the choice of the virtual field $\delta\mathbf{u}$. Polynomial functions, constant functions, finite element shape functions or combinations, all are possible fields, many of them used in well stated strategies shown in [9, 10, 11]. In Chapter 4 a technique is proposed that can be classified within the VFM by using a particular discrete choice of the virtual field $\delta\mathbf{u}$.

1.2.4 Equilibrium Gap Method

The Equilibrium Gap Method (EGM) has been developed in order to model problems in which elastic heterogeneities can be expressed by a scalar field [3]. Thus, the elasticity tensor is written as

$$\mathbf{C}(x) = A(x)\mathbf{C}_0 \,, \tag{1.5}$$

where $A(x)$ is a scalar field that modifies the reference tensor $\mathbf{C}_0$. It is easy to see the similarity between (1.5) and the damage equation (2.23) in which the field $(1-d(x))$ plays the role of $A(x)$.

For a given discrete (nodal) displacement field obtained through experimental measurements, a finite element mesh is built. The nodes of such a mesh coincide in position with those points of the experimental data. Then, assuming a piecewise scalar field $A(x) = A^e$ constant over each element, the stiffness matrix at each element is given by

$$\mathbf{K}^e = A^e\mathbf{K}_0^e \,, \tag{1.6}$$

where $\mathbf{K}_0^e$ is the reference stiffness matrix of the element. Then, the equilibrium equation at the m-th degree of freedom (DOF) of a node which does not support any external load, has the form

$$\sum_{\boldsymbol{e}|m\in E^e} A^e \boldsymbol{e}_m^T \mathbf{K}_0^e \mathbf{u}^e = 0 \,, \tag{1.7}$$

where $\mathbf{u}^e$ is the vector of DOFs on element E^e, $\boldsymbol{e}_m$ is the m-th unit vector, and the summation is carried out for the elements that share the m-th DOF.[1]

Equation 1.7 means that the internal force of a node with no external forces applied will be zero, if the correct field A^e is identified. The identification runs from the minimisation of an objective (error) function expressed as

---

[1] $(\cdot)^T$ denotes the transpose of a vector, matrix or tensor.

$$\mathscr{F}(\boldsymbol{a}) = (\mathbf{M}\boldsymbol{a} - \boldsymbol{q})^T \mathbf{W} (\mathbf{M}\boldsymbol{a} - \boldsymbol{q}) \ , \tag{1.8}$$

where $\boldsymbol{a}$ is given by $\boldsymbol{a} = \ln(A^e)$, $\mathbf{M}$ and $\boldsymbol{q}$ are dependent on the measured displacement field and $\mathbf{W}$ is a weighting matrix.

Complete formulation and applications of the EGM are shown in [12, 13, 14]. In these works, the EGM is formulated aiming to solve the problem of damage field identification, for composite materials undergoing a biaxial loading.

1.2.5 Reciprocity Gap Method

This technique is based on the Maxwell-Betti reciprocity theorem and adjoint fields. The material parameters of the constitutive equation are identified again by minimising (or setting to zero) the reciprocity gap for any adjoint field. This approach uses rather technical concepts and differs substantially from what is applied here. More details and applications can be found in [15, 16, 17, 18].

1.3 ORGANISATION OF THIS TEXT

In order to cover the many subjects involved in this study, this text is organised as follows. In Chapter 2, the basis of Lemaitre's elastoplastic damage model is briefly presented, starting with a short introduction to the so-called, Continuous Damage Mechanics. Then, the text proceeds with the mathematical formulation of the model as well as its implementation in a finite element (FE) code. In Chapter 3, a short review of the Digital Image Correlation (DIC) technique is presented. Furthermore, in Chapter 4, the core of this work, a specific method for the identification of constitutive material parameters by means of displacement fields is proposed. Chapter 5, as a natural extension of Chapter 4, explores the feasibility of the method proposed in the preceding chapter, reporting on a set of numerical and experimental tests. Finally, Chapter 6 presents the conclusions and achievements of this study, as well as proposals for future work.

2 CONTINUUM DAMAGE MECHANICS

In this chapter, a brief description of the damage phenomenon and its modelling within the framework of continuum thermodynamics are presented. In particular, Lemaitre's ductile damage model is detailed, which will be used later within the proposed identification procedures.

The existence (or nucleation) of microvoids and/or microcracks in any solid material as well as their evolution (growth and coalescence) are understood as a damage phenomenon, in which materials have their capability to withstand loads progressively reduced [19].

The damage phenomenon is closely related to the mechanisms of deformation of each kind of material. Type and rate of loading, temperature as well as environment aspects; influence the mechanisms that cause progressive deformation and degradation.

In the last five decades, a branch of Continuum Mechanics called Continuum Damage Mechanics (CDM) has been developed. Within a continuum framework, microvoids and/or microcracks, i.e. damage discontinuities, are considered small enough when compared with the dimensions of a Representative Volume Element (RVE), in such a way, all properties are represented by means of homogenized variables in this element of matter [2]. The dimension of an RVE varies from material to material. For instance, the order of magnitude of an RVE is assumed to be: $\left(10^{-1}mm\right)^3$ for metals and ceramics; $(1mm)^3$ for polymers; and $\left(10^{2}mm\right)^3$ for concrete [1, 2].

According to [1], the mechanical behaviour of materials can be analysed in three scales: micro-, macro- and mesoscale. The microscale is where strain and damage mechanisms are expected to occur. The mesoscale is the scale in which the constitutive equations are proposed. Finally, the macroscale is the scale of engineering structures.

Changes in material properties can occur in the mesoscale (scale of an RVE) or in the microscale (scale of discontinuities in an RVE). In both cases, these changes can be taken as a function of the type of loading and the mechanism of failure.

Damage mechanisms can be classified as follows [1, 2]:

- Ductile damage
- Brittle damage
- Creep damage
- Low cycle fatigue damage
- High cycle fatigue damage

The present work is focused on ductile damage. In this case, damage is intimately related to plastic deformation, which is the main mechanism of damage evolution.

The first mathematical formulation of damage was introduced by Kachanov in 1958 [19]. In order to represent the damage phenomenon, Kachanov proposed the introduction of a scalar variable into a uniaxial creep model. Later, in 1963, Rabotnov presented the concept of an effective area, giving a physical meaning to Kachanov's proposal. He suggested that the development of microvoids and/or microcracks causes the reduction of the area where forces are distributed. Thus, based on the above propositions, the scalar damage variable d has been defined as

$$d = \frac{A_0 - A}{A_0} \tag{2.1}$$

where A_0 is the original area without damage and A is the damaged area (with voids), such as shown in Fig. 2.1 . The value 0 (zero) of the scalar damage variable is related to an undamaged material, whereas 1 (one) is related to a completely damaged material. Furthermore, Kachanov replaced the true stress σ by the effective stress σ_{eff} into the constitutive equation of the uniaxial creep model [19]. The effective stress is related to the true stress by

$$\sigma_{eff} = \frac{\sigma}{1 - d} \tag{2.2}$$

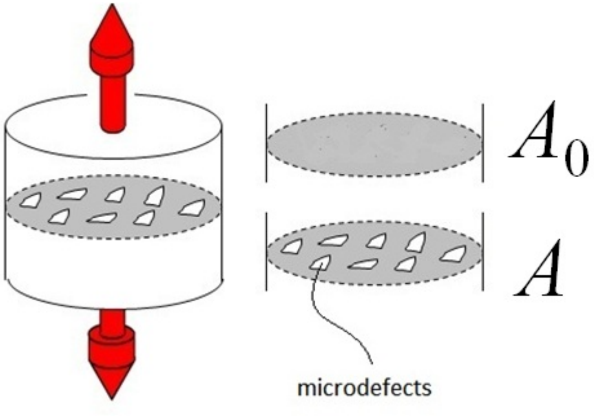

Figure 2.1: Definition of the effective area. Undamaged (A_0) and damaged (A) areas.

Another important concept was presented by Lemaitre in 1971, who proposed the hypothesis of strain equivalence. Such hypothesis is enunciated as follows, “the deformation behaviour of the damaged material can be represented by the constitutive laws of the virgin material in which the usual stress is replaced by the effective stress”([19], p.475). This is one of the bases of Lemaitre’s elastoplastic damage model used in this work.

Besides Lemaitre’s models, many other different formulations are found in literature. Among them, is Gurson’s model for porous materials, in which damage is intrinsically related to the growth of voids due to mechanical actions. The corresponding damage internal-variable is defined as the volume fraction of these voids embedded in the material matrix [20, 21, 22, 23]. Both Lemaitre’s and Gurson’s like models are characterised by scalar variables and apply to isotropic damaging. Further considerations extend these models to anisotropic behaviours, pressure dependence (closure or opening of cracks and voids) etc.

2.1 CONTINUUM THERMODYNAMICS

The damage phenomenon is always associated with an irreversible process. Therefore, its mathematical treatment in continuum mechanics is frequently stated within the framework of thermodynamics with internal variables.

In this section, the main statements of this formalism are briefly shown, with the aim of providing the theoretical basis and the proper notation used in Lemaitre's model. The formulation described here and in sections 2.2 and 2.3 are based on [19, 24].

Conservation of Mass

Let us consider a body $\mathscr{B}$ that occupies an open region Ω bounded by Γ. The principle of mass conservation can be stated for any material point in the body $\mathscr{B}$ by means of the following expression:

$$\dot{\rho} + \rho \nabla \cdot \dot{\mathbf{u}} = 0 \tag{2.3}$$

where ρ is density, $\mathbf{u}$ is a displacement vector field and $\nabla \cdot (\cdot)$ is the divergence operator. Equation 2.3 is referred to as the continuity equation. Its physical meaning is described by [24] as follows, "The divergence of the velocity vector measures the rate of flow of material away from the particle and is equal to the unit rate of decrease of density in the neighbourhood of the particle", (p.207).

Momentum Balance

In the deformed configuration, and for any arbitrary particle of the body $\mathscr{B}$, the balance of momentum (linear and angular) can be expressed in terms of the Cauchy stress tensor $\boldsymbol{\sigma}$ by means of the following differential equations and boundary conditions:

$$\nabla \cdot \boldsymbol{\sigma} + \mathbf{b} = \rho \ddot{\mathbf{u}} \text{ in } \Omega \tag{2.4a}$$

$$\mathbf{t} = \boldsymbol{\sigma} \mathbf{n} \text{ in } \Gamma \tag{2.4b}$$

$$\boldsymbol{\sigma} = \boldsymbol{\sigma}^T \tag{2.4c}$$

where $\mathbf{b}$ is the body force, $\mathbf{n}$ is the unit vector normal to the deformed surface, $\mathbf{t}$ is the traction vector. Equation (2.4a) is the so-called Cauchy's Equations of Motion [24]. The symmetry of $\boldsymbol{\sigma}$ in (2.4c) is the consequence of the balance of angular momentum.

The First Principle of Thermodynamics

This principle postulates the conservation of energy in any physical system, i.e. the sum of the power input and heat input is equal to the rate of change in the total energy of the system.. The power input is the work produced by external traction and body forces over the body $\mathscr{B}$. The heat input is the heat conducted through the boundary Γ and the heat produced by an internal heat source in $\mathscr{B}$. Then, for any point of $\mathscr{B}$, we have

$$\rho \dot{e} = \boldsymbol{\sigma} : \boldsymbol{D} + \rho r - \nabla \cdot \mathbf{q} \tag{2.5}$$

where e is the specific internal energy, $\boldsymbol{D}$ is the rate of deformation tensor, $\boldsymbol{\sigma} : \boldsymbol{D}$ is the stress power per unit volume in the deformed configuration of a body, r is the density of heat production and $\mathbf{q}$ is the heat flux vector.

The Second Principle of Thermodynamics

This principle, which is intimately related to the irreversibility of dissipative processes, postulates that in a body $\mathscr{B}$ the rate of change of entropy is always greater than, or equal to the rate of entropy input due to heating [24]. The local counterpart of this postulate is given by the following inequality, valid for any material point of $\mathscr{B}$:

$$\rho \dot{s} + \nabla \cdot \left[\frac{\mathbf{q}}{\theta} \right] - \frac{\rho r}{\theta} \geq 0 \tag{2.6}$$

where s is the specific entropy and θ is the absolute temperature.

Clausius-Duhem Inequality

By combining the first and second principles, we obtain

$$\rho \dot{s} + \nabla \cdot \left[\frac{\mathbf{q}}{\theta} \right] - \frac{1}{\theta} (\rho \dot{e} - \boldsymbol{\sigma} : \boldsymbol{D} + \rho r + \nabla \cdot \mathbf{q}) \geq 0 \, . \tag{2.7}$$

We further consider Helmholtz free energy per unit mass ψ,

$$\psi = e - \theta s \, , \tag{2.8}$$

and the identity

$$\nabla \cdot \left[\frac{\mathbf{q}}{\theta} \right] = \frac{1}{\theta} \nabla \cdot \mathbf{q} - \frac{1}{\theta^2} \mathbf{q} \cdot \nabla \theta \tag{2.9}$$

to introduce them into Eq. 2.7 in order to obtain the Clausis-Duhem inequality:

$$\boldsymbol{\sigma} : \boldsymbol{D} - \rho(\dot{\psi} + s\dot{\theta}) - \frac{1}{\theta}\mathbf{q} \cdot \nabla\theta \geq 0 \,. \tag{2.10}$$

Assuming that, due to Fourier's law, the last term is always non-positive (heat flows from warmer to colder parts of the body), i.e.

$$-\mathbf{q} \cdot \nabla\theta \geq 0 \,, \tag{2.11}$$

then, we retrieve the Clausius-Planck inequality:

$$\boldsymbol{\sigma} : \boldsymbol{D} - \rho(\dot{\psi} + s\dot{\theta}) \geq 0 \,. \tag{2.12}$$

2.2 LEMAITRE'S DAMAGE MODEL FOR ELASTOPLASTICITY WITH NONLINEAR HARDENING

The following model was developed by Lemaitre in order to represent the behaviour of elastoplastic damage in ductile materials. This constitutive formulation is based on the concept of effective stress and on the hypothesis of equivalent strain. The model presented here takes into account both isotropic and nonlinear kinematic hardening based on Armstrong-Frederick's law [19, 25, 26]. It is assumed that the process being modelled is isothermal. In addition, no differences between tension and compression behaviour is considered.

Since an infinitesimal strain approach has been adopted, the rate of deformation tensor $\boldsymbol{D}$ in Eq. (2.10) is assumed to be equal to the time derivative of the infinitesimal strain tensor $\dot{\boldsymbol{\varepsilon}}$. Furthermore, the additive decomposition can be applied to the strain tensor $\boldsymbol{\varepsilon}$, i.e.

$$\boldsymbol{\varepsilon} = \boldsymbol{\varepsilon}^e + \boldsymbol{\varepsilon}^p \,, \tag{2.13}$$

where $\boldsymbol{\varepsilon}^e$ and $\boldsymbol{\varepsilon}^p$ are respectively the elastic and the plastic contributions.

The initial point of the current constitutive formulation is to define a free energy potential that is a function of a set of state variables (here it is assumed that thermal effects are negligible):

$$\psi = \psi(\boldsymbol{\varepsilon}^e, \breve{\varepsilon}^p, \mathbf{X}, d) \,, \tag{2.14}$$

where $\boldsymbol{\varepsilon}^e$ is the elastic strain tensor, $\breve{\varepsilon}^p$ is the damage accumulated plastic strain, $\mathbf{X}$ is the back strain tensor (related to kinematic hardening) and d is the scalar damage variable.

The free energy is usually split into two parts

$$\psi = \psi^e(\boldsymbol{\varepsilon}^e, d) + \psi^p(\breve{\varepsilon}^p, \mathbf{X}) \,, \tag{2.15}$$

where ψ^e and ψ^p are respectively the elastic-damage and the plastic contributions.

The rate of change of the free energy is given by

$$\dot{\psi} = \frac{\partial \psi}{\partial \boldsymbol{\varepsilon}^e} : \dot{\boldsymbol{\varepsilon}}^e + \frac{\partial \psi}{\partial d}\dot{d} + \frac{\partial \psi}{\partial \breve{\varepsilon}^p}\dot{\breve{\varepsilon}}^p + \frac{\partial \psi}{\partial \mathbf{X}} : \dot{\mathbf{X}} \,. \tag{2.16}$$

Thus, the Clausius-Duhem inequality (2.10) is rewritten as

$$\left(\boldsymbol{\sigma} - \bar{\rho}\frac{\partial \psi}{\partial \boldsymbol{\varepsilon}^e}\right) : \dot{\boldsymbol{\varepsilon}}^e - \rho\frac{\partial \psi}{\partial d}\dot{d} + \boldsymbol{\sigma} : \dot{\boldsymbol{\varepsilon}}^p - \rho\left(\frac{\partial \psi}{\partial \breve{\varepsilon}^p}\dot{\breve{\varepsilon}}^p + \frac{\partial \psi}{\partial \mathbf{X}} : \dot{\mathbf{X}}\right) \geq 0 \,. \tag{2.17}$$

This inequality must be valid for any condition. For a purely elastic process in which dissipative effects are negligible, we have

$$\boldsymbol{\sigma} = \bar{\rho}\frac{\partial \psi}{\partial \boldsymbol{\varepsilon}^e} \,. \tag{2.18}$$

Including this result in (2.17), it leads to a dissipative function which must be positive in order to satisfy the second principle. Such a dissipative function includes two terms. The first is related to the damage phenomenon and the second to the plastic one:

$$\varphi \equiv \varphi^d + \varphi^p \geq 0 \,, \tag{2.19}$$

where

$$\varphi^d = -\rho\frac{\partial \psi}{\partial d}\dot{d} \,, \tag{2.20}$$

and

$$\varphi^p = \boldsymbol{\sigma} : \dot{\boldsymbol{\varepsilon}}^p - \rho\left(\frac{\partial \psi}{\partial \breve{\varepsilon}^p}\dot{\breve{\varepsilon}}^p + \frac{\partial \psi}{\partial \mathbf{X}} : \dot{\mathbf{X}}\right) \,. \tag{2.21}$$

The elastic-damage potential is defined as

$$\bar{\rho}\psi^e(\boldsymbol{\varepsilon}^e,d) = \frac{1}{2}\boldsymbol{\varepsilon}^e : (1-d)\mathbf{C}^e : \boldsymbol{\varepsilon}^e \,, \tag{2.22}$$

where $\bar{\rho}$ is the reference mass density, and $\mathbf{C}^e$ is the isotropic elastic tensor. In this case, the elasticity law is given by

$$\boldsymbol{\sigma} = \bar{\rho}\frac{\partial\psi}{\partial\boldsymbol{\varepsilon}^e} = (1-d)\mathbf{C}^e : \boldsymbol{\varepsilon}^e \,. \tag{2.23}$$

Now, by extending the concept of an effective stress to the three-dimensional case, we have the definition of the effective stress tensor,

$$\boldsymbol{\sigma}_{eff} = \mathbf{C}^e : \boldsymbol{\varepsilon}^e \,. \tag{2.24}$$

Thus, the generalised form of the effective stress (Eq.2.25) is obtained by replacing (Eq. 2.24) into (Eq. 2.23).

$$\boldsymbol{\sigma}_{eff} \equiv \frac{\boldsymbol{\sigma}}{1-d} \,. \tag{2.25}$$

The thermodynamic conjugate force Y related to the damage variable d is given by

$$Y \equiv \bar{\rho}\frac{\partial\psi}{\partial d} = -\frac{1}{2}\boldsymbol{\varepsilon}^e : \mathbf{C}^e : \boldsymbol{\varepsilon}^e \,. \tag{2.26}$$

This expression can also be rewritten by means of the inverse of the elasticity law as

$$\begin{aligned} Y &= -\frac{1}{2\,(1-d)^2}\,\boldsymbol{\sigma} : [\mathbf{C}^e]^{-1} : \boldsymbol{\sigma} \\ &= -\frac{1}{2E(1-d)^2}\left[(1+\nu)\ \boldsymbol{\sigma}:\boldsymbol{\sigma} - \nu\,(\mathrm{tr}\,\boldsymbol{\sigma})^2\right] \\ &= -\frac{q^2}{2E(1-d)^2}\left[\frac{2}{3}\,(1+\nu) + 3\,(1+2\nu)\left(\frac{p}{q}\right)^2\right] \\ &= -\frac{q^2}{6G(1-d)^2} - \frac{p^2}{2K(1-d)^2} \,, \end{aligned} \tag{2.27}$$

where $q \equiv \sqrt{\frac{3}{2}\mathbf{s}:\mathbf{s}}$ is the von Mises effective stress, $\mathbf{s} \equiv \boldsymbol{\sigma} - p\mathbf{I}$ is the deviatoric stress tensor, $\mathbf{I}$ is second-order identity tensor, $p = \frac{1}{3}\boldsymbol{\sigma}$ is the hydrostatic stress, E is the Young's modulus, ν is the Poisson ratio, G and K are respectively the shear modulus and the bulk modulus.

Isotropic and kinematic hardening forces

The plastic contribution of the free energy potential can also be split into two parts. The first one is associated with the isotropic hardening ψ^I, and the second with the kinematic hardening ψ^K.

$$\bar{\rho}\,\psi^p(\breve{\varepsilon}^p,\mathbf{X}) = \bar{\rho}\,\psi^I(\breve{\varepsilon}^p) + \bar{\rho}\,\psi^K(\mathbf{X})\ . \tag{2.28}$$

Thus, the conjugate forces κ and $\boldsymbol{\beta}$, respectively related to the isotropic and kinematic hardening, are given by

$$\kappa \equiv \bar{\rho}\,\frac{\partial\psi^p(\breve{\varepsilon}^p,\mathbf{X})}{\partial\breve{\varepsilon}^p} = \kappa(\breve{\varepsilon}^p)\ , \tag{2.29}$$

while the conjugate force of the tensor $\mathbf{X}$ is the *back-stress* $\boldsymbol{\beta}$:

$$\boldsymbol{\beta} \equiv \bar{\rho}\,\frac{\partial\psi^p(\breve{\varepsilon}^p,\mathbf{X})}{\partial\mathbf{X}} = \boldsymbol{\beta}(\mathbf{X})\ . \tag{2.30}$$

The kinematic hardening is based on the Armstrong-Frederick's law, which leads to

$$\psi^K(\mathbf{X}) = \frac{a}{2}\mathbf{X}:\mathbf{X}\ , \tag{2.31}$$

$$\boldsymbol{\beta}(\mathbf{X}) = a\mathbf{X}\ . \tag{2.32}$$

where a is a material constant related to Armstrong-Frederick's law.

The Yield Function

The yield function used in Lemaitre's damage model has an expression similar to the traditional von Mises function:

$$\Phi = \frac{\sqrt{3J_2(\mathbf{s}-\boldsymbol{\beta})}}{1-d} - \sigma_y\ , \tag{2.33}$$

where $\mathbf{s}$ is the deviatoric stress tensor, $\boldsymbol{\beta}$ is the back-stress tensor, σ_y is a hardening function defined by $\sigma_y = \sigma_y(\breve{\varepsilon}^p)$ and $J_2(\mathbf{s}-\boldsymbol{\beta})$ is the second invariant of $\mathbf{s}-\boldsymbol{\beta}$, being $J_2(\boldsymbol{A}) = \frac{1}{2}\left[(\operatorname{tr}\boldsymbol{A})^2 - \operatorname{tr}\boldsymbol{A}^2\right]$ for any matrix $\boldsymbol{A}$. The hardening function can be defined as follows,

$$\sigma_y(\breve{\varepsilon}^p) = \sigma_{y0} + \kappa, \tag{2.34}$$

where σ_{y0} is the initial yield stress, i.e. the uniaxial yield stress of a virgin material. In the present work, we adopted the following formulation for the hardening function

$$\sigma_y(\breve{\varepsilon}^p) = \sigma_{y0} + \mathrm{k}\left(1 - \mathrm{e}^{-\mathrm{n}\breve{\varepsilon}^p}\right), \tag{2.35}$$

where k and n are material constants.

The Flow Potential and Evolution of Internal Variables

The complete formulation of the current constitutive model depends on the determination of evolution laws for the internal variables. A usual way of doing that is to define a dissipative potential whose derivative, provides the desired laws. Depending on the convexity properties of this potential, the second law is automatically satisfied.

In plasticity, if the yield function takes the role of the dissipative (flow) potential, models are called associative. Otherwise, they are non-associative. The present model is a non-associative one, and the flow potential takes the form

$$\Psi = \Phi + \frac{b}{2a}\boldsymbol{\beta} : \boldsymbol{\beta} + \frac{\mathrm{r}}{(1-d)(\mathrm{S}+1)}\left(\frac{-Y}{\mathrm{r}}\right)^{\mathrm{S}+1}, \tag{2.36}$$

where a, b, r and S are material constants. The constants a and b are related to Armstrong-Frederick's model, and r and S are associated with damage evolution. With this definition, the resulting evolution laws are given by

$$\dot{\boldsymbol{\varepsilon}}^p = \dot{\gamma}\boldsymbol{N} \tag{2.37}$$

$$\dot{\breve{\varepsilon}}^p = \dot{\gamma} \tag{2.38}$$

$$\dot{\boldsymbol{\beta}} = \dot{\gamma}(a\boldsymbol{N} - b\boldsymbol{\beta}) \tag{2.39}$$

$$\dot{d} = \dot{\gamma}\frac{1}{1-d}\left(\frac{-Y}{\mathrm{r}}\right)^{\mathrm{S}} \tag{2.40}$$

where $-Y$ is the energy density release rate due to damage (2.27) and $\boldsymbol{N}$ is the flow vector.

$$\boldsymbol{N} = \sqrt{\frac{3}{2}}\frac{\mathbf{s}-\boldsymbol{\beta}}{(1-d)\,\|\mathbf{s}-\boldsymbol{\beta}\|} \tag{2.41}$$

The rate multiplier $\dot{\gamma}$ is equal to the damage accumulated plastic rate (2.38) and accounts for the amplitude of the plastic flow. Moreover, the plastic flow only occurs for a saturated yield function Φ. In other words, it must satisfy the following complementarity conditions:

$$\Phi \leq 0\ ,\ \dot{\gamma} \geq 0\ ,\ \Phi\dot{\gamma} = 0\ . \tag{2.42}$$

Conditions (2.42) enforce that (a) the yield function is lower than or equal to zero, (b) the plastic multiplier rate is non-negative and (c) both quantities simultaneously, cannot be different from zero.

2.2.1 Integration Algorithm

A temporal integration procedure is needed in order to update incrementally the internal variables. In the present case, a traditional (fully implicit) elastic-predictor/plastic-corrector-mapping is used [19, 27].

Firstly, we establish the elastic predictor. It consists of the initial trial state for both strain and stress elastic tensors, which are respectively defined as [1] [2]

$$\boldsymbol{\varepsilon}^{e\ trial}_{n+1} = \boldsymbol{\varepsilon}^{e}_{n} + \Delta\boldsymbol{\varepsilon} \tag{2.43}$$

$$\sigma^{e\ trial}_{n+1} = (1-d_n)\mathbf{C}^e : \varepsilon^{e\ trial} \tag{2.44}$$

where $\Delta\boldsymbol{\varepsilon} = \boldsymbol{\varepsilon}_{n+1} - \boldsymbol{\varepsilon}_n$

With these values, the plastic consistency must be verified. This is

---

[1] $(\cdot)_n$ and $(\cdot)_{n+1}$ indicate respectively the current and the updated states.

[2] $(\cdot)^{trial}$ denotes a trial condition.

performed by evaluating Φ^{trial},

$$\Phi^{trial} = \frac{\sqrt{3J_2(\mathbf{s}_{n+1}^{trial} - \beta_n)}}{1 - d_n} - \kappa(\breve{\varepsilon}_n^p) - \sigma_{y0} \; . \tag{2.45}$$

If $\Phi^{trial} \leq 0$ then the trial state defines the current value of the state variables. Thus, the following update is set:

$$(\cdot)_{n+1} = (\cdot)_{n+1}^{trial} \tag{2.46}$$

Otherwise, it is necessary to calculate the set of unknowns $(\boldsymbol{\sigma}_{n+1}, \beta_{n+1}, d_{n+1}, \Delta\gamma)$ that satisfies the incremental consistency equations, given by

$$\left\{ \begin{array}{c} \frac{\sqrt{3J_2(\mathbf{s}_{n+1}^{trial} - \beta_n)}}{1-d_n} - \kappa(\breve{\varepsilon}_n^p + \Delta\gamma) - \sigma_{y0} \\ \sigma_{n+1}^{e\ trial} - (1 - d_{n+1})\mathbf{C}^e : (\varepsilon_{n+1}^{e\ trial} - \Delta\gamma \boldsymbol{N}_{n+1}) \\ \beta_{n+1} - \beta_n - \Delta\gamma(a\boldsymbol{N}_{n+1} - b\beta_{n+1}) \\ d_{n+1} - d_n - \frac{1}{1-d_{n+1}} \left(\frac{-Y_{n+1}}{\mathrm{r}} \right)^{\mathrm{S}} \Delta\gamma \end{array} \right\} = \left\{ \begin{array}{c} 0 \\ 0 \\ 0 \\ 0 \end{array} \right\} , \tag{2.47}$$

where

$$\boldsymbol{N}_{n+1} = \frac{3}{2} \frac{\mathbf{s}_{n+1} - \beta_{n+1}}{(1 - d_{n+1})\sqrt{3J_2(\mathbf{s} - \beta)}} \tag{2.48}$$

Once the system has been solved, the remaining internal variables are updated as follows:

$$\breve{\varepsilon}_{n+1}^p = \breve{\varepsilon}_n^p + \Delta\gamma \, , \tag{2.49}$$

$$\varepsilon_{n+1}^{e\ trial} = \varepsilon_{n+1}^e + \Delta\gamma \boldsymbol{N}_{n+1} \; . \tag{2.50}$$

2.3 LEMAITRE'S SIMPLIFIED MODEL

A remarkable simplification of Lemaitre's model is achieved if the kinematic hardening is not considered. In this case, we have $\boldsymbol{\beta} = a = b = 0$, and the return-mapping system (2.47) is reduced to a single nonlinear equation [19, 28]. This fact considerably improves the computational performance of the algorithm. However, it is important to notice that the simplified version of Lemaitre's model is restricted to situations where reverse plastic loadings are not expected to occur.

The yield function 2.33 and evolution laws 2.37, 2.38, 2.39, 2.40 are then simplified to the following expressions

$$\Phi = \frac{\sqrt{3J_2(\mathbf{s})}}{1-d} - \sigma_y \,, \tag{2.51}$$

$$\dot{\varepsilon}^p = \dot{\gamma}\boldsymbol{N} \,, \tag{2.52}$$

$$\dot{\bar{\varepsilon}}^p = \dot{\gamma} \,, \tag{2.53}$$

$$\dot{d} = \dot{\gamma}\frac{1}{1-d}\left(\frac{-Y}{\mathrm{r}}\right)^{\mathrm{S}} \,, \tag{2.54}$$

where

$$\boldsymbol{N} = \sqrt{\frac{3}{2}}\frac{\mathbf{s}}{(1-d)\,\|\mathbf{s}\|} \,. \tag{2.55}$$

Finally, the same consistency conditions required in 2.42 must be satisfied.

$$\Phi \leq 0 \,,\ \dot{\gamma} \geq 0 \,,\ \Phi\dot{\gamma} = 0$$

2.3.1 Integration Algorithm

The integration algorithm that applies to the simplified version of Lemaitre's model has the same structure as the complete one. The detailed mathematical deduction of the current algorithm will not be presented but can be found in [19, 28]. Nevertheless, the incremental procedure is reproduced here for reasons of completeness.

Firstly, the elastic-trial strain is calculated based on their last converged value and on the subsequent strain increment (2.56). The accumulated damage-plastic strain is taken from the last step (2.57). Based on the volumetric and deviatoric contributions of the elastic-trial strain, the corresponding hydrostatic (2.58) and deviatoric (2.59) effective stresses are computed.

After that, the effective von Mises equivalent stress (2.60) is calculated.

$$\varepsilon^{e\ trial}_{n+1} = \varepsilon_n + \Delta\varepsilon \tag{2.56}$$

$$\breve{\varepsilon}^{p\ trial}_{n+1} = \breve{\varepsilon}^{p}_{n} \tag{2.57}$$

$$\tilde{p}^{trial}_{n+1} = K\varepsilon^{e\ trial}_{v\ n+1} \tag{2.58}$$

$$\tilde{s}^{trial}_{n+1} = 2G\varepsilon^{e\ trial}_{d\ n+1} \tag{2.59}$$

$$\tilde{q}^{trial}_{n+1} = \sqrt{\frac{3}{2}}\left\| s^{trial}_{n+1} \right\| \tag{2.60}$$

Once the trial state has been estimated, the plastic consistency must be verified. If

$$\tilde{q}^{trial}_{n+1} - \sigma_y(\breve{\varepsilon}^{p\ trial}_{n+1}) \leq 0 \tag{2.61}$$

then the trial state establishes the current state of the variables, i.e.

$$(\cdot)_{n+1} = (\cdot)^{trial}_{n+1} \tag{2.62}$$

Otherwise, the following single-equation return mapping has to be solved for $\Delta\gamma$:

$$F(\Delta\gamma) \equiv \omega(\Delta\gamma) - \omega_n + \frac{\Delta\gamma}{\omega(\Delta\gamma)}\left(\frac{-Y(\Delta\gamma)}{\mathrm{r}}\right)^{\mathrm{S}} = 0\,, \tag{2.63}$$

where

$$\omega_{n+1} \equiv 1 - d_{n+1} = \omega(\Delta\gamma) = \frac{3G\Delta\gamma}{\tilde{q}^{trial}_{n+1} - \sigma_y(\breve{\varepsilon}^{p}_{n} + \Delta\gamma)}\,, \tag{2.64}$$

$$-Y(\Delta\gamma) \equiv \frac{\left[\sigma_y(\breve{\varepsilon}^{p}_{n} + \Delta\gamma)\right]^2}{6G} + \frac{\tilde{p}^{2}_{n+1}}{2K} \tag{2.65}$$

Once $\Delta\gamma$ has been obtained, the remaining internal variables are updated as follows:

$$\breve{\varepsilon}^{p}_{n+1} = \breve{\varepsilon}^{p}_{n} + \Delta\gamma \tag{2.66}$$

$$p_{n+1} = \omega(\Delta\gamma)\tilde{p}_{n+1} \tag{2.67}$$

$$q_{n+1} = \omega(\Delta\gamma)\sigma_y(\breve{\varepsilon}_n^p) \tag{2.68}$$

$$\mathbf{s}_{n+1} = \frac{q_{n+1}}{\tilde{q}_{n+1}^{trial}}\tilde{\mathbf{s}}_{n+1}^{trial} \tag{2.69}$$

$$\sigma_{n+1} = \mathbf{s}_{n+1} + p_{n+1}\mathbf{I} \tag{2.70}$$

$$\varepsilon_{n+1}^{e} = \frac{1}{2G}\mathbf{s}_{n+1} + \frac{1}{3}\varepsilon_{v\ n+1}^{e\ trial}\mathbf{I} \tag{2.71}$$

The Tangent Operator

In the context of the finite element method, a consistent tangent operator might be needed in order to solve the global equilibrium problem. If the integration algorithm operates within the elastic domain, the tangent operator is directly given by

$$\mathbf{D} = (1 - d_{n+1})\mathbf{C}^e \tag{2.72}$$

However, if the stress solution is inside the plastic domain, the tangent operator can be computed by means of

$$\mathbf{D} = \frac{\mathrm{d}\boldsymbol{\sigma}_{n+1}}{\mathrm{d}\boldsymbol{\varepsilon}_{n+1}^{e\ trial}}\ . \tag{2.73}$$

In the simplified formulation, the tangent operator can be analytically obtained [19, 28] and it takes the following expression:

$$\begin{aligned}\mathbf{D} =& c_1\ \mathbf{I}_\mathrm{d} + c_2\ \bar{\mathbf{s}}_{n+1} \otimes \bar{\mathbf{s}}_{n+1} + c_3\ \bar{\mathbf{s}}_{n+1} \otimes \mathbf{I} \\ &+ c_4\ \mathbf{I} \otimes \bar{\mathbf{s}}_{n+1} + c_5\ \mathbf{I} \otimes \mathbf{I}\end{aligned} \tag{2.74}$$

where, $c_1, c_2, ..., c_5$ are scalar values calculated from the converged variables, $\mathbf{I}_\mathrm{d}$ is the deviatoric projection tensor, $\mathbf{I}$ is the second-order identity matrix and $\bar{\mathbf{s}}_{n+1}$ is the normalised stress deviator

$$\bar{\mathbf{s}}_{n+1} = \frac{\mathbf{s}_{n+1}}{||\mathbf{s}_{n+1}||}\ . \tag{2.75}$$

The complete definition of the elastoplastic operator is shown in Appendix B.

2.4 REMARKS ON FINITE ELEMENT CODE IMPLEMENTATION

In this work, a nonlinear finite element code was implemented which is able to solve the simplified version of Lemaitre's damage model (see Section 2.3). In such a code, three types of finite elements were included: a three-dimensional eight-nodes hexahedron (Hex8); a two-dimensional four-nodes axisymmetric quadrilateral (Q4); and a two-dimensional four-nodes plane stress quadrilateral (Q4). All of them employ a full-integration scheme. The solution of the nonlinear equilibrium equations is computed by using the traditional Newton-Raphson method. The code is based on small displacement-strain formulation, and its implementation is based on [19, 29, 30, 31, 32].

In order to validate the code implementation, some tests were carried out on three different models. To this aim, a mechanical tensile test was numerically simulated on a thin notched sheet model of 0.9 mm thickness, whose geometry is shown in Fig. 2.2. By considering the planes of symmetry, only one-eighth of the geometry was taken into account with the corresponding boundary conditions shown in Fig. 2.2.

A first verification test considered 3-D elements (Hex8) and elastoplastic (no damage) constitutive behaviour. The results obtained were successfully compared with a commercial FE code. A second test considered an identical problem, but this time it was simulated with plane stress elements (Q4), which led again to results which were very close to those obtained with a commercial FE code. Finally, the reliability of the implemented FE code was assessed by considering that the profile shown in Fig.2.2 represents a cylindrical specimen. Then, axisymmetric Q4 elements were used to simulate the tensile test by using Lemaitre's damage model. On this occasion, the implemented code provided results that agreed almost perfectly with those, that were obtained with the FE code HYPLAS [19]. In all cases mentioned above, the absolute difference between stress values, that were computed at integration points, with the implemented FE code, the commercial one, and HYPLAS was lower than 0.001 MPa.

Such an implemented FE code was used to generate sets of numerical data that were employed in order to verify and validate the procedure for identification of constitutive parameters introduced in Chapter 4. Although 2-D and 3-D models have been initially employed in these tests, only results related to 2-D models are presented in Chapter 5.

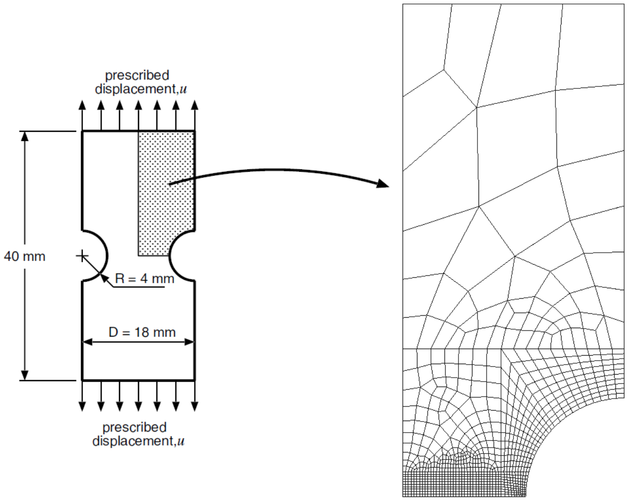

Figure 2.2: Geometry used in the verification of the FE code (proposed by [19]).

3 DIGITAL IMAGE CORRELATION

Digital Image Correlation (DIC) is a non-contact measurement method based on optics, which is used to measure motion and/or deformation of an object by digitally processing a sequence of images. Each image in this sequence records the state of the object at a specific point in time. As a full-field non-contact optical method, DIC has been used in order to replace pointwise measurement techniques, what is specially useful in cases where localised strains are expected to occur [33].

With the emergence of digitalised images, many digital image analysis methods have been developed to be used in the field of experimental solid mechanics. Different interferometric and non-interferometric optical measurement techniques have been proposed in order to obtain experimental information about displacements or strain fields on the surface of specimens.

Each kind of technique has limitations and advantages. Holography, laser speckle, moiré interferometer are some of the few examples of interferometric techniques developed for use with a coherent light source. They are particularly well suited to measure small displacements and strains. On the other hand, Digital Image Correlation has shown its potentialities to measure finite strains (localised or not) that appear in inelastic deformations in metals or polymers.

If a non-coherent light source is used in conjunction with the DIC method, different patterns such as lines, grids, dots and random arrays can be used as reference entities of measurement. One of the most usual approaches is to employ a random pattern [34]. Therefore, it is desirable that the texture of the surface of a specimen has suitable characteristics like a random grey intensity distribution with appreciable contrast. This condition may naturally be found on the surface of the specimen (texture), or be artificially produced as shown in Figure 3.1, where the specimen was painted using an airbrush.

Another important operational aspect related to DIC is the choice of a region of interest (ROI), in which motion and/or deformation are expected to be observed. In this region, a virtual grid formed by points called markers is defined (see Fig. 3.2). The way in which the motion of these markers are tracked along a sequence of images constitutes the DIC procedure, whose main characteristics are explained below.

Consider two images of the ROI, before and after deformation. For each marker of the grid in the undeformed image, a subset of $(2\mathrm{M}+1) \times (2\mathrm{M}+1)$ pixels is defined, having the marker as the central pixel of the subset. This subset, which has its own grey intensity distribution, will occupy a

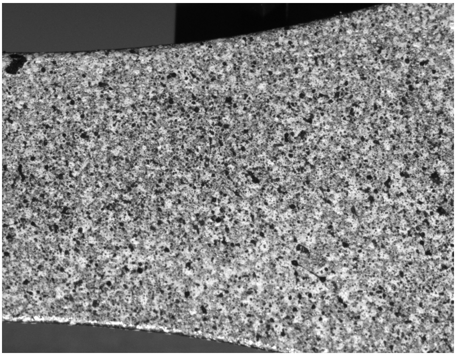

Figure 3.1: An example of a random speckle pattern.

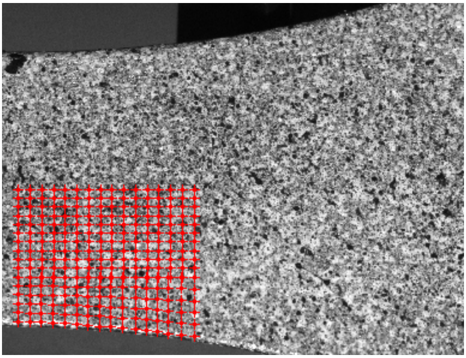

Figure 3.2: An example of an ROI and a grid of markers.

different position in the deformed image. Therefore, the main concept behind the DIC method is to search the appropriate mapping that allows to correlate the subset grey distribution of a first image into a second one to be found.

The correlation procedure is then carried out by means of an optimisation method that looks for the proper mapping parameters at each subset by minimising a correlation criterion, which is also called correlation function.

Two usual families of correlation functions are the cross-correlation (CC) criterion and the sum-squared difference (SSD) correlation criterion. These have been presented under different forms in literature [34], we show here the most robust of each kind:

Zero-Nomalized Cross-Correlation

$$C_{ZNCC} = \sum_{i=-M}^{M} \sum_{j=-M}^{M} \left\{ \frac{[f(x_i, y_j) - f_m] \times [g(x'_i, y'_j) - g_m]}{\Delta f \Delta g} \right\} \tag{3.1}$$

Zero-Nomalized Sum of Squared Differences

$$C_{ZNSSD} = \sum_{i=-M}^{M} \sum_{j=-M}^{M} \left[\frac{f(x_i, y_j) - f_m}{\Delta f} - \frac{g(x'_i, y'_j) - g_m}{\Delta g} \right]^2 \tag{3.2}$$

In Eq.3.1 and Eq. 3.2, $f(x_i, y_j)$ and $g(x'_i, y'_j)$ are respectively the grey intensity in the reference and in the deformed subset; (x_i, y_j) and (x'_i, y'_j) are the coordinates of the subset pixels before and after deformation. And,

$$f_m = \frac{1}{(2M+1)^2} \sum_{i=-M}^{M} \sum_{j=-M}^{M} f(x_i, y_j) \tag{3.3}$$

$$g_m = \frac{1}{(2M+1)^2} \sum_{i=-M}^{M} \sum_{j=-M}^{M} g(x'_i, y'_j) \tag{3.4}$$

$$\Delta f = \sqrt{\sum_{i=-M}^{M} \sum_{j=-M}^{M} [f(x_i, y_j) - f_m]^2} \tag{3.5}$$

$$\Delta g = \sqrt{\sum_{i=-M}^{M} \sum_{j=-M}^{M} [g(x'_i, y'_j) - g_m]^2} \tag{3.6}$$

As the shape of a reference subset changes after deformation, it is necessary to map the displacement of points around the subset centre. For such a purpose, a displacement mapping function is employed. A generic two dimensional mapping function can be set as follows:

$$\begin{aligned} x'_i &= x_i + \xi(x_i, y_j) \\ y'_j &= y_j + \eta(x_i, y_j) \\ (i, j &= -M : M) \end{aligned} \tag{3.7}$$

In the case of a first-order mapping, we have

$$\begin{aligned} \xi &= u + \frac{\partial u}{\partial x}\Delta x + \frac{\partial u}{\partial y}\Delta y \\ \eta &= v + \frac{\partial v}{\partial x}\Delta x + \frac{\partial v}{\partial y}\Delta y \end{aligned} \tag{3.8}$$

or, in the case of second-order mapping

$$\begin{aligned} \xi &= u + \frac{\partial u}{\partial x}\Delta x + \frac{\partial u}{\partial y}\Delta y + \frac{1}{2}\frac{\partial^2 u}{\partial x^2}\Delta x^2 + \frac{1}{2}\frac{\partial^2 u}{\partial y^2}\Delta y^2 + \frac{\partial^2 u}{\partial xy}\Delta x\Delta y \\ \eta &= v + \frac{\partial v}{\partial x}\Delta x + \frac{\partial v}{\partial y}\Delta y + \frac{1}{2}\frac{\partial^2 v}{\partial x^2}\Delta x^2 + \frac{1}{2}\frac{\partial^2 v}{\partial y^2}\Delta y^2 + \frac{\partial^2 v}{\partial xy}\Delta x\Delta y \end{aligned} \tag{3.9}$$

where $\Delta x = x_i - x_0$, $\Delta y = y_j - y_0$ and (x_0, y_0) is the coordinate of the centre of the subset (marker). The set $\mathbf{p} = (u, v, ...)$ is the set of displacements in x- and y-direction of a marker position (x_0, y_0) and the corresponding partial derivatives $(\frac{\partial u}{\partial x}, \frac{\partial v}{\partial x}, \frac{\partial u}{\partial y}, \frac{\partial v}{\partial y}, ...)$ according to the order of the mapping being used. Thus, $\mathbf{p}$ is the set of parameters to be identified during the correlation process.

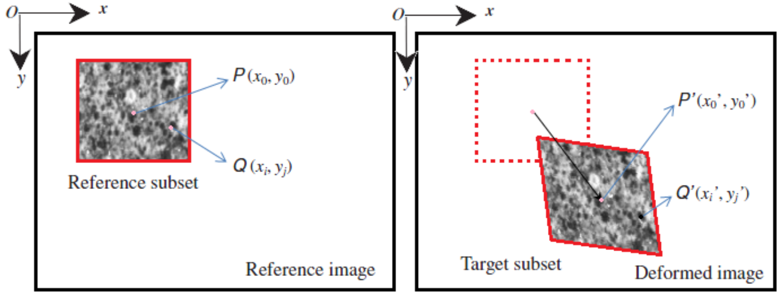

Figure 3.3: Schematic representation of a subset deformation and the displacement vector associated with a marker (adapted from [33]).

The CC criteria can be related to SSD ones. For example, the C_{ZNCC} criterion value is related to the C_{ZNSSD} value by the following expression: $C_{ZNSSD}(\mathbf{p}) = 2[1 - C_{ZNCC}(\mathbf{p})]$. According to [33], the C_{ZNCC} and C_{ZNSSD} criterion have a robust noise-proof performance and they are insensitive to some effects of illumination lighting, such as offset and linear scale effects.

To finalise this brief explanation of the technique used in this work, it is worth mentioning an important technical step. For a given set of mapping parameters, new positions (x'_i, y'_j) are calculated. Since these new coordinates do not necessarily coincide with the integer position of a pixel in the deformed image, the grey value at sub-pixel positions must be provided. To this aim, several grey interpolation schemes can be found in literature. For instance, bilinear interpolation, bicubic interpolation, bicubic B-spline interpolation, biquintic B-spline interpolation, and bicubic spline interpolation. High-order interpolation schemes are recommended, because they provide a higher registration accuracy and better convergence, although increasing computational costs. The minimisation of the correlation function f_C (using a CC or SSD criterion) can be performed by a Newton-Raphson procedure. A single Newton updating of the set $\mathbf{p}$ is given by

$$\mathbf{p} = \mathbf{p}_0 - \frac{\nabla f_C(\mathbf{p}_0)}{\nabla^2 f_C(\mathbf{p}_0)} , \tag{3.10}$$

where $\mathbf{p}_0$ is the initial guess, $\mathbf{p}$ is the updated value, f_C is the correlation function and $\nabla(\cdot)$, $\nabla^2(\cdot)$ are respectively first- and second-order derivatives with respect to the unknown parameters $\mathbf{p}$.

Like in any other measurement method, many factors may influence the DIC performance. It is out of the scope of this work to provide a detailed discussion of metrological aspects related to DIC, but here we briefly point out important issues.

According to [33], the accuracy of DIC is usually affected by factors such as

- numerical error related to the algorithm;
- random speckle pattern characteristics;
- lightning;
- optical characteristics related to the lens being used;
- vibration;
- errors associated with the specimen;
- loading conditions, and so on.

In order to improve the accuracy and precision of measurements, several studies have been conducted aiming at evaluating the errors associated with DIC. For instance, in [35], [36] and [37], the authors evaluate errors related to the DIC algorithm by considering different factors, such as the size of subsets as well as the characteristics of the random speckle pattern. In the earlier stage of development, DIC sub-pixel algorithms were able to provide absolute sensitivities and accuracies between 0.01 and 0.5 pixels, but according to [36], it is possible to achieve absolute errors below 0.002 pixels for sub-pixel algorithms such as those based on gradient or Newton-Raphson methods. It is important to bear in mind that such evaluations consider only numerical aspects of DIC algorithm. Thus, an error of 0.002 pixels might be considered as the maximum error associated with the DIC algorithm. In this work a Newton-Raphson algorithm with robust mapping was used, interpolation and correlation functions. The mapping was performed by using a second order function combined with a spline bicubic interpolation function. We also employed the C_{ZNSSD} correlation criterion due to its robust noise-proof performance. These choices allow the achievement of the resolution observed in high quality DIC algorithms reported in literature.

In the current study, additional assessment of the DIC technique based on metrology and statistics was not carried out.

Remark: Considering the DIC algorithm that was used in the current work and following a similar procedure presented by [33] for an evaluation of the errors related to strain calculation, we can give the following error estimate. If we assume the absolute error for displacement measurements is 0.002 pixels, then based on the image resolution (in pixels) and the dimensions of the ROI/grid (in millimetres, Fig. 5.29) that were employed in this work (Chapter 5), we find that the absolute error of displacement measurements would be 3.337×10^{-5} mm. Thus, by employing a forward difference [33] and taking into account the smallest distance among all markers (0.362 mm), this led to $\left(\left|\pm 3.337 \times 10^{-5}\right| + \left|\pm 3.337 \times 10^{-5}\right|\right)/0.362 = 1.844 \times 10^{-4}$ mm/mm for the measurement of strain errors. Such as mentioned above, this evaluation is based solely on the numerical solution of the DIC algorithm and might be assumed as the maximum error of the measuring instrument, i.e. the lowest error that would be possible to be achieve. Additional sources of error were not evaluated. However, this estimate provides a reasonable way to evaluate the quality of the data obtained by means of DIC.

4 DIRECT IDENTIFICATION OF MATERIAL PARAMETERS FROM OPTICAL DATA

In Section 1.1, several methods that make use of full-field measurement data for the identification of constitutive material parameters are briefly explained. As already pointed out, the classification proposed in [3] is quite general and different operational techniques can be designed for specific problems.

In this chapter, a particular method is proposed. It may be classified within the class of Virtual Field Methods, since its formulation can be obtained by choosing the virtual functions $\delta\mathbf{u}$ (of Eq. (1.4)) as being equal to the shape functions of a convenient finite element mesh, where such a mesh is related to a DIC mesh. From this choice, two objective functions are defined in order to minimise the error between the internal and external forces. In the following sections, a detailed description of such a method is shown. During the development of the present work, a similar proposition appeared in [38]. The latter differs from the current one in the way the objective function is defined.

4.1 PRELIMINARY CONSIDERATIONS ABOUT EXPERIMENTAL DATA

Consider a prismatic specimen and a grid of points (markers) defined over the image of the front surface of this specimen as shown in Fig. 4.1. During a mechanical test, each point of this grid is tracked by using the DIC, while the total loading data are simultaneously recorded. Such a procedure can provide the following information:

- The history of 3-D displacement of each point on the surface or at least, the history of 2-D displacements;
- The history of the applied loading which is measured with the load cell of the testing machine.

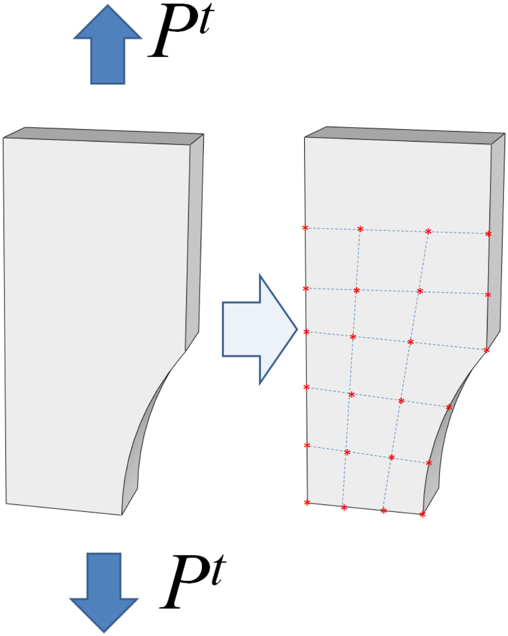

Figure 4.1: A prismatic specimen and a grid of points (markers) defined over the image of the front surface of this specimen.

The displacement data that are measured on the observed surface of the specimen frequently need to be complemented with additional hypotheses. These hypotheses should allow an extrapolation of these data for the whole volume of the specimen. In this case, the following options may be considered:

1. Assumption of a distribution law for the out-of-plane strain field ε_z, where ε_z is based on in-plane information and is in accordance with a suitable transversal displacement distribution. For example, we can mention the case of a constant strain related to a linear distribution of the transversal displacement. Such an assumption provides a complete three-dimensional displacement for the whole domain Ω occupied by the specimen. Another example that can be used to estimate

the thickness variation of a thin plate is suggested by [38] as $\mathrm{t}(\varepsilon_x, \varepsilon_y) = \mathrm{t}_0 \mathrm{e}^{-\varepsilon_x - \varepsilon_y}$, where t_0 is the initial thickness and ε_x and ε_y are in-plane strain components.

2. The DIC method is able to provide the three-dimensional displacement field of the surface. Then, u_z displacements can be used as additional information for out-of-plane strain extrapolations.

3. Use of simplified 2-D models (e.g. plane stress state) that need only in-plane data in order to compute the ε_z field.

4.2 MINIMUM ERROR PROBLEM

Consider the weak equilibrium problem of finding the displacement $\mathbf{u} \in \mathcal{K}$, such that

$$\delta R(\mathbf{u}, \delta \mathbf{u}) = \delta F(\mathbf{u}, \delta \mathbf{u}) - \delta Q(\mathbf{u}, \delta \mathbf{u}) = 0 \qquad \forall \delta \mathbf{u} \in \mathcal{V} \tag{4.1}$$

where $\mathcal{K}$ and $\mathcal{V}$ are respectively the set of kinematically admissible displacements and the set of virtual displacements. Let us make $\mathbf{u} = \mathbf{u}^t$, where the symbol $\mathbf{u}^t$ denotes the history of displacements up to time t. Then, the internal and external virtual works take the general form

$$\delta F(\mathbf{u}^t, \delta \mathbf{u}) = \int_{\Omega^t} \boldsymbol{\sigma}(\mathbf{u}^t) \cdot \nabla^s \delta \mathbf{u} \, \mathrm{d}\Omega^t \tag{4.2}$$

$$\delta Q(\mathbf{u}^t, \delta \mathbf{u}) = \int_{\Omega^t} \mathbf{b}(\mathbf{u}^t) \cdot \delta \mathbf{u} \, \mathrm{d}\Omega^t + \int_{\Gamma^t} \mathbf{f}(\mathbf{u}^t) \cdot \delta \mathbf{u} \, \mathrm{d}\Gamma^t \tag{4.3}$$

where $\boldsymbol{\sigma}(\mathbf{u}^t)$ is the constitutive response of the material model to the history of deformations up to time t. In general, $\boldsymbol{\sigma}(\mathbf{u}^t)$ is nonlinear and time dependent. Note that Eq.(4.2) is not restricted to infinitesimal kinematics since Ω^t denotes the deformed configuration and $\nabla^s = \nabla^s_{ij}(\cdot) = \frac{1}{2}\left(\frac{\partial(\cdot)}{\partial \mathbf{x}_i} + \frac{\partial(\cdot)}{\partial \mathbf{x}_j}\right)$, where $\mathbf{x}$ represents the spatial coordinates in the deformed configuration.

Consider now a finite element mesh attached to the grid shown in Fig.4.1. Take $\delta \mathbf{u} = \mathbf{N}_i$, being $\mathbf{N}_i$, i=1,NDOF the corresponding global shape functions and NDOF the number of degrees of freedom provided by that mesh. Substituting $\delta \mathbf{u}$ in 4.2 and 4.3, the following NDOF residual equations are obtained

$$\mathbf{R}_i(\mathbf{u}^t) = \mathbf{F}_i(\mathbf{u}^t) - \mathbf{Q}_i(\mathbf{u}^t) = \mathbf{0} \tag{4.4}$$

with

$$\mathbf{F}_i(\mathbf{u}^t) = \int_{\Omega^t} \mathbf{B}_i^T \boldsymbol{\sigma}(\mathbf{u}^t)\, \mathrm{d}\Omega^t \tag{4.5}$$

$$\mathbf{Q}_i(\mathbf{u}^t) = \int_{\Omega^t} \mathbf{N}_i^T \mathbf{b}(\mathbf{u}^t)\, \mathrm{d}\Omega^t + \int_{\Gamma^t} \mathbf{N}_i^T \mathbf{f}(\mathbf{u}^t)\, \mathrm{d}\Gamma^t \tag{4.6}$$

The matrix $\mathbf{B}_i = \mathcal{D}\mathbf{N}_i$ contains the strain components associated with the shape functions $\mathbf{N}_i$ and $\mathcal{D}$ which is the usual strain operator. $\mathbf{F}_i$ and $\mathbf{Q}_i$ are then the classical internal and external forces of the i-th DOF of finite-element discrete equations, which leads to a null residual value $\mathbf{R}_i$ if the equilibrium is satisfied.

In particular cases in which infinitesimal kinematics are considered, we have $\Omega^t \simeq \Omega_0 \simeq \Omega$ and all operations are performed in the undeformed configuration. Equation (4.4) states that the equilibrium is attained at the configuration $\mathbf{u}^t$, which provides a balance between internal and external forces.

In a typical numerical simulation, we look for the history of the displacement field $\mathbf{u}^t$ as the unknown variable of the problem. By means of a nonlinear technique, such as Newton's Method, we search for a displacement configuration that reduces the residual vector $\mathbf{R}(\mathbf{u}^t)$ to zero. However, in the present problem, information about the history of the displacement field $\mathbf{u}^t$ is available by experimental measurements. The unknowns are the material parameters of the constitutive model $\boldsymbol{\sigma}(\mathbf{u}^t)$.

The identification problem can then be set as the minimisation of an objective function Ψ based on the error between internal (computed) and external forces (measured):

$$\mathbf{p}^\star = \arg\min_{\mathbf{p}\in\mathcal{P}} \left\|\Psi(\mathbf{p};\mathbf{u}^t)\right\|^2 \tag{4.7}$$

where $\mathbf{p}$ is a vector of material parameters within a set of admissible values $\mathcal{P}$.

To compute the internal forces, let us consider again the specimen shown in Fig. 4.1. From the front surface of the specimen, a grid of points is defined and the history of the displacement $\mathbf{u}^t$ is stored, wherein $\mathbf{u}^t$ is measured by means of DIC. This grid is transformed into an FE one whose nodes are classified in five sets such as shown in Fig. 4.2)and listed in Table 4.1.

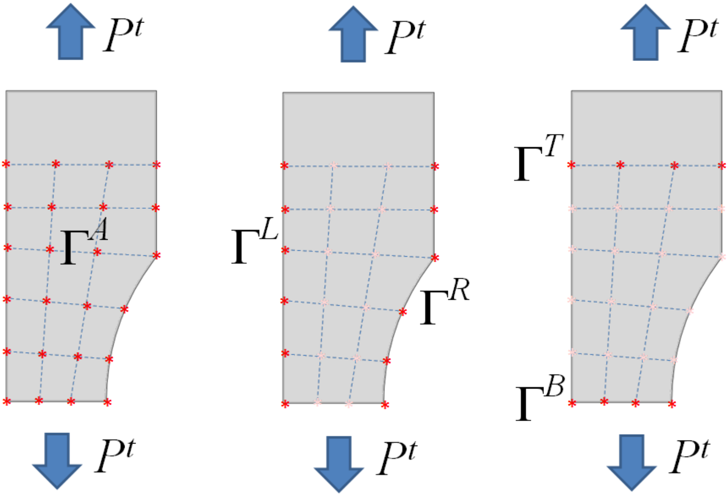

Figure 4.2: FE mesh based on a grid of points and the definition of sets of nodes.

Table 4.1: Definition of suitable sets of nodes for the objective function A.

Γ^T	set of nodes on the top egde of the ROI
Γ^B	set of nodes on the bottom egde of the ROI
Γ^L	set of nodes on the left egde of the ROI
Γ^R	set of nodes on the right egde of the ROI
Γ^A	set of nodes on the surface of the ROI

Based on these sets, and in order to achieve the best solution for the identification problem, different objective functions may be suggested. In this work, two types of objective functions are proposed. Although they are defined in the context of a two-dimensional problem, their extension to three-dimensional cases is straightforward.

4.2.1 Objective Function A

This first objective function combines the residual forces defined in Table 4.2:

Table 4.2: Definition of the objective function A. Residual functions.

Internal force in x-direction at nodes in Γ^A, excluding nodes in Γ^T, Γ^B, Γ^L, Γ^R:	$\mathbf{R}_1^t = \mathbf{F}_x^A(\mathbf{u}^t) = \mathbf{0}$
Internal force in y-direction at nodes in Γ^A, excluding nodes in Γ^T, Γ^B, Γ^L, Γ^R:	$\mathbf{R}_2^t = \mathbf{F}_y^A(\mathbf{u}^t) = \mathbf{0}$
Internal force in y-direction at nodes in Γ^T :	$R_3^t = \sum \mathbf{F}_y^T(\mathbf{u}^t) - P^t = 0$
Internal force in y-direction at nodes in Γ^B:	$R_4^t = \sum \mathbf{F}_y^B(\mathbf{u}^t) + P^t = 0$

The residual vector $\mathbf{R}_1^t$ indicates that the internal force in x-direction $\mathbf{F}_x^A$ at every node of Γ^A (excluding nodes in Γ^T, Γ^B, Γ^L, Γ^R) must be zero if the equilibrium is satisfied. Analogous condition must be satisfied for the internal force $\mathbf{F}_y^A$ in y-direction. The third and fourth expressions verify that the sum of all internal forces of the top and bottom boundaries in y-direction must be equal to the total external force P^t, that is applied to the specimen. Thus a single valued function at time t can be set as

$$\psi^t = \sum_{i=1}^{n} \alpha_i^t \left\|\mathbf{R}_i^t\right\|^2 \tag{4.8}$$

where α_i^t are weighting parameters and in this case $n = 4$ (number of residual functions, see Tab. tab:objfuncs). Finally, the global objective function is established by means of the summation

$$\Psi = \sum_t \psi^t \tag{4.9}$$

4.2.2 Objective Function B

A second proposition for a multi-objective function is defined as follows. In Fig. 4.3, the top boundaries of three rows of elements are identified.

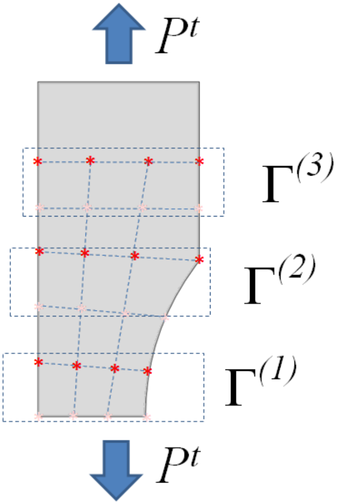

Figure 4.3: Definition of suitable sets of elements/nodes for the objective funtion B. Top-boundaries Γ^i

In each row of elements, the summation of the internal forces F_y^{ij} of all nodes j that belongs to the top-boundary Γ^i of the row must equilibrate the external force P^t. This allows the definition of the out-of-balance force for each set of elements/nodes (being these sets those which define Γ^i); and the difference between the sum of internal forces and the measured loads is computed by means of

$$\mathbf{R}_i^t = \left[\sum_{j=1}^{m} F_y^{(ij)}(\mathbf{u}^t) \right]_i - P^t \tag{4.10}$$

where m is the total number of nodes in Γ^i.

And again, we can make use of Eq. 4.8 and Eq. 4.9

$$\psi^t = \sum_{i=1}^{n} \alpha_i^t \left\| \mathbf{R}_i^t \right\|^2$$

$$\Psi = \sum_t \psi^t$$

where n is the total number of boundaries Γ^i (e.g. in Fig. 4.3, $n = 3$). In the current work, the weighting parameters α_i^t were taken as $\alpha_i^t = 1$, for all cases.

4.3 OBJECTIVE FUNCTION: ALGORITHMIC STRUCTURE

Both objective functions are implemented and coupled with Lemaitre's model simulation code presented in Section 2.3. These objective functions are then minimised by an optimisation code. For the sake of clearness, the structure of the algorithm used to calculate the objective functions is shown in 4.3.

It is well known that Lemaitre's model may face convergence problems during the solution of the damage-plastic multiplier (Eq. 2.63) [19]. Large strain increments usually account for such convergence problems. As these strain increments are defined by the available experimental data, a special algorithm was implemented to reduce such increments, in case of convergence failure.

The idea is simple and consists of an equally distributed subdivision of the incremental deformation of an element, into smaller sub-steps. With a smaller strain increment, it is expected that the convergence of the constitutive equations at each integration point will be achieved. If so, stresses are sequentially computed until the complete time step has been attained. Finally, at the end of the time step, the stress is used for the internal force calculation, as in the usual procedure.

Table 4.3: Objective function algorithm

```
Computation of the objective function $\Psi = \Psi(\mathbf{p}, \mathbf{u})$

**Loop (time increments)** $t \in \{t_0, t_1, \ldots, \mathrm{f}\}$
for $t = t_0$ to $t_\mathrm{f}$

    Load $\mathbf{u}^t$

    **Loop (elements)** $e \in \{1, 2, \ldots, n\}$
    for $e = 1$ to $n$

        **Loop (integration points)** $i \in \{1, 2, \ldots, nip\}$
        for $i = 1$ to $nip$

            Compute $\boldsymbol{\varepsilon}^t_{(e,i)} = \mathbf{B}\mathbf{u}^t_{(e)}$
            Compute the stress $\boldsymbol{\sigma}_{(e,i)}$ at the integration point
            by using the corresponding constitutive model,
            e.g. simplified Lemaitre's model.

        **end loop (integration points)**

        Compute the Element's Internal Force Vector $\mathbf{f}^e = \int_{\Omega^e} \mathbf{N}^e \boldsymbol{\sigma} \mathrm{d}\Omega$
        Store $\mathbf{f}^e$ in the global Internal Force Vector $\mathbf{F}$

    **end loop (elements)**

    Compute and store $\boldsymbol{\psi}^t = \sum_{i=1}^{n} \alpha_i^t \, ||\mathbf{R}_i^t||^2$

**end loop (time increments)**

Compute $\Psi = \sum_t \boldsymbol{\psi}^t$
```

5 RESULTS

In Chapter 4, a method for identification of constitutive material parameters was proposed. Its performance was tested by carrying out the identification of constitutive parameters from full-field data. These data had firstly been obtained from numerical experiments and secondly from physical ones. Then, in the current chapter an evaluation process organised into two parts is presented.

In the first part, the identification method was tested based on numerically generated data (ngd). In such a case, the required history of the full displacement field and loading data was generated by means of a finite element model. The model employs the same constitutive formulation that is used later in the identification of material parameters. The purpose of these initial tests was to evaluate the efficiency of the identification algorithm and of different objective functions, knowing a priori the existence of a zero-error solution. Furthermore, these tests allowed the investigation and solution to possible difficulties of the overall identification procedure. This first part is reported in Section 5.1.1. In the second part, the method was evaluated based on real experimental data that were acquired during a uniaxial tensile test of a low-carbon steel specimen. Section 5.2 presents a general description of the identification procedure for this case, including details related to DIC usage as well as an analysis of the results achieved. Additionally, such as presented in section 5.3, a validation test was conducted, in which the parameters identified in the tests reported in Section 5.2 were used in a finite element simulation of a tensile test.

It is worth mentioning that a non-standard specimen geometry was used in all calculations (Fig. 5.1). This geometry ensures that yielding and damage, start in the central region of the specimen when it is submitted to a tensile test. This induced localisation allows a priori definition of the area subjected to image acquisition, improving the quality of the images, and as a consequence, the DIC accuracy.

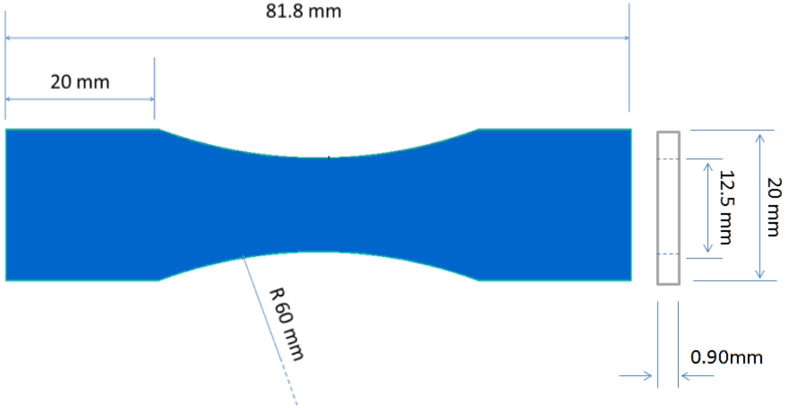

Figure 5.1: Geometry and dimensions of the non-standard specimen employed in the present work.

5.1 IDENTIFICATION BY USING NUMERICALLY GENERATED DATA

5.1.1 Numerical Data Generation

A finite element model was set up to simulate a uniaxial tensile test and to generate the proper data for the numerical experiments. The model was based on the assumption of a plane stress state and took advantage of the symmetry of the problem. Figure 5.2 shows the finite element mesh and the applied boundary conditions. A displacement of $u_y = 0.682$ mm is prescribed in the upper boundary of the model, which is equivalent to a total displacement of $u_y = 1.364$ mm in a typical tensile test.

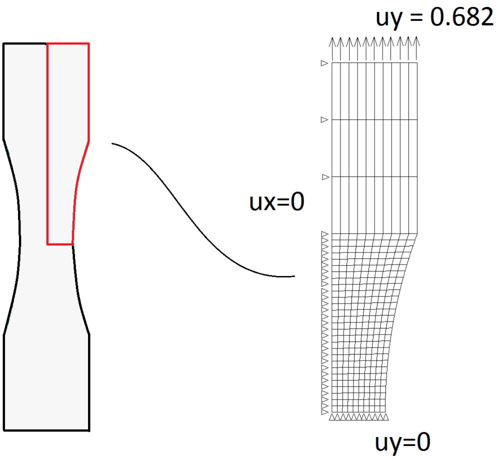

Figure 5.2: The finite element model employed to generate the numerical data for the verification tests.

The simplified version of Lemaitre's model, which is detailed in Section 2.3 and characterised by the set of parameters in Table 5.1, was chosen to represent the mechanical behaviour of a hypothetical material.

Table 5.1: Material parameters chosen to represent the mechanical behaviour of a hypothetical material in numerical tests.

Young's Modulus - (E)	207000 MPa
Poisson's Ratio - (ν)	0.29
Initial Yield Stress - (σ_{y0})	165 MPa
Elastoplastic constant - (k)	300
Elastoplastic exponent - (n)	50
Damage constant - (r)	0.3 MPa
Damage exponent - (S)	4

The uniaxial stress-strain behaviour of this material is shown in Fig. 5.3, wherein two curves are presented. The first curve corresponds to a model of a pure elastoplastic material (without damage), while the second one corresponds to Lemaitre's ductile damage model. Additionally, Fig. 5.4 shows the accumulated damage vs. equivalent plastic strain.

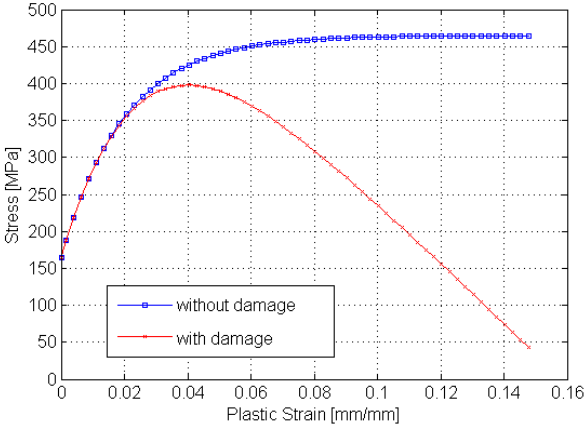

Figure 5.3: Representation of the uniaxial stress-strain behaviour of the testing (hypothetical) material by using Lemaitre's model.

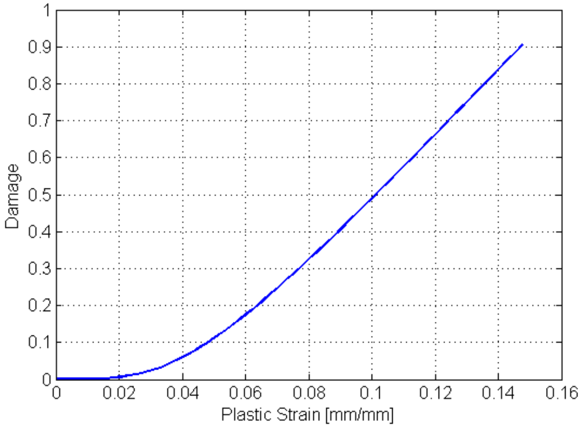

Figure 5.4: Damage vs. plastic strain behaviour of the testing (hypothetical) material by using Lemaitre's model.

With these settings, the generation of the numerical data was carried out. We notice that a prescribed displacement u_y was applied on the upper boundary of the specimen, varying linearly from 0 to 0.628 mm in increments of $\Delta u_y = 0.001$ mm. Figure 5.5 illustrates both y-displacement and damage distribution for the last time-step[1]. The corresponding load vs. displacement curve is presented in Fig.5.6.

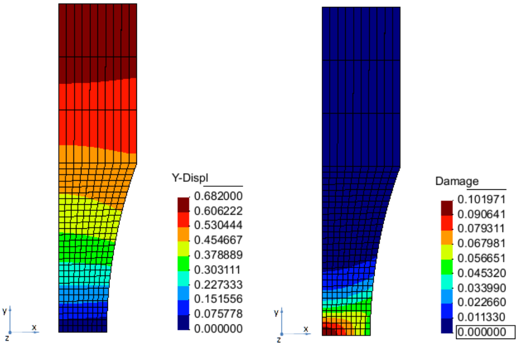

Figure 5.5: Displacement (left) and damage (right) fields from numerically generated data for a hypothetical material (last time-step data computed by means of an FE simulation).

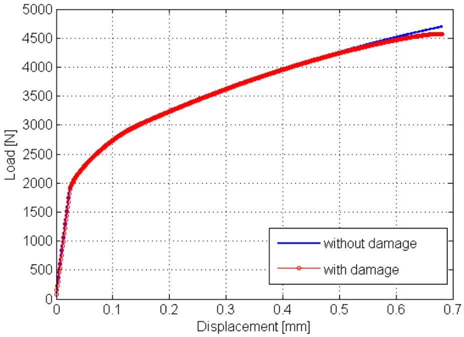

Figure 5.6: Loading vs. Displacement curve. Behaviour of a hypothetical material under undamaged and damage conditions.

---

[1] The term *time step* is employed throughout this text to indicate a point in time in which a full-field displacement measurement is associated with a specific loading state.

In order to emulate the data that are obtained from DIC in real experimental cases, a region of interest (ROI) was defined in a way totally analogous to what is done for a real specimen (Fig. 5.7). Then, the history of nodal internal forces and nodal displacements was recorded for 682 time steps, being both force and displacement related to the mesh within the ROI. The displacement field obtained in the last time step of the numerical simulation is shown in Fig. 5.8.

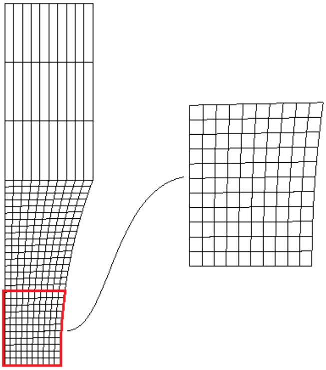

Figure 5.7: Definition of an ROI for numerical tests (definition based on the FE mesh used in the tests).

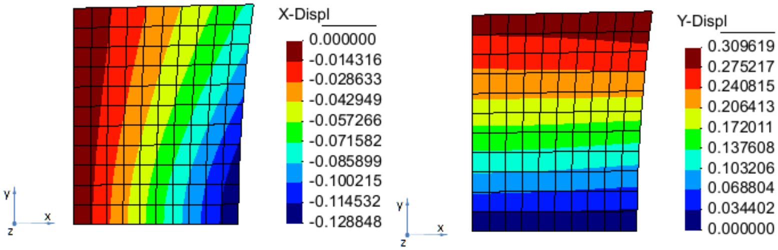

Figure 5.8: Displacement fields in the ROI (last time-step data computed by means of an FE simulation). (Left) $\mathbf{u}_x$ and (Right) $\mathbf{u}_y$ [mm] .

5.1.2 Identification of Constitutive Material Parameter

The minimisation of the objective function was performed by means of an interior point algorithm, based on [39, 40, 41, 42]. As no analytical derivatives were provided they were numerically computed through finite differences. This fact certainly influences the number of iterations needed to achieve convergence and possibly the accuracy of the converged solution. To initiate the tests of the algorithm's performance, a convergence study was carried out, considering two variables. The first is the type of Objective Function (A or B) and the second is the number of time steps used to compute each one.

The tests were run using the exact values of the material parameters as the initial values for the optimisation problem. This was to verify if the algorithm points to the initial solution as the optimum point.

The reason for testing a fewer number of time steps (larger step increments) is to verify the possibility of speeding up the identification process. Thus, it was observed whether a fewer number of time steps could lead to reductions in the accuracy of the solution or even to a failure during the nonlinear calculation of the damage-plastic multiplier.

The tests were all carried out by considering the elastic parameters $(E, \nu, \sigma_{y0}) = (207000, 0.29, 165)$ known and fixed, and the plastic-damage parameters (k, n, r, S) the variables of the optimisation. The initial point was set up (k, n, r, S) $= (300, 50, 0.3, 4)$, i.e. the exact solution. The objective function A is defined according to Tables4.1 and 4.2 and considering the ROI shown in Fig. 5.7. Fig. 5.9 display the rows of elements/nodes corresponding to the objective function B.

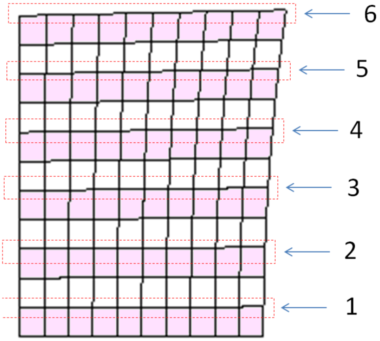

Figure 5.9: Sets of elements/nodes related to the objective function B that were employed in the verification tests.

The results of the tests are then summarised in Table 5.2. It is possible to see that all cases, due to the characteristics of the optimisation algorithm and also due to the absence of analytical derivatives, show iterations before achieving a “converged” new point (theoretically, the best point is the initial one). It is also possible to see the loss of accuracy of the “converged” solution as a result in the reduction of the number of time steps employed in the objective function calculation. Errors of less than 1% were found in the solution. The best one was achieved for Objective Function B, when the data from all 682 time-steps were used.

Table 5.2: Results of the parameter identification from numerical generated data (1).

Analysis	Type	Steps	k	n	r	S	Min	Eval/Iter	Fig.
NA01	A	682	300.0132	49.9979	0.2999	3.9975	100	92/9	5.10
NA02	A	136	300.8047	49.8371	0.2984	3.8692	26	93/12	5.12
NA03	A	60	300.9567	49.8072	0.2994	3.8406	13	88/13	5.14
NB01	B	682	300.0000	50.0000	0.3000	4.000	6	36/2	-
NB02	B	136	300.8398	49.8295	0.2982	3.8722	18	175/21	-
NB03	B	60	301.4717	49.7065	0.2976	3.7566	12	106/15	-

Type - Objective function used according to description in Chapter 4.
Steps - Number of time-steps used from 682 available.
Min - Value of the objective function convergence.
Eval/Iter - Number of objective function evaluations and the total number of iterations for convergence.

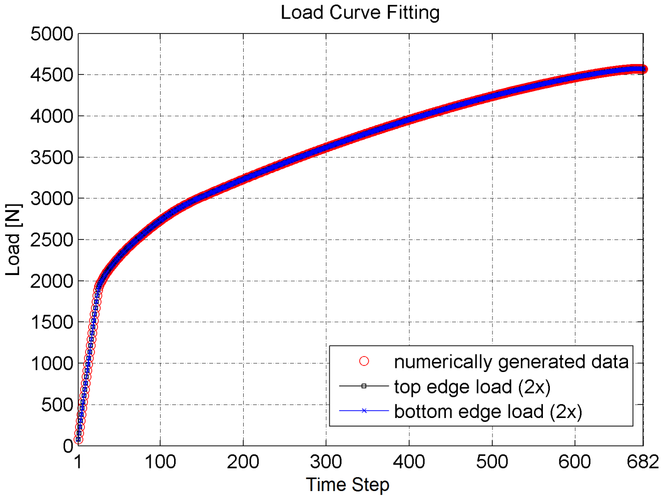

Figure 5.10: Load Curve Fitting - Analysis NA01 (ngd)

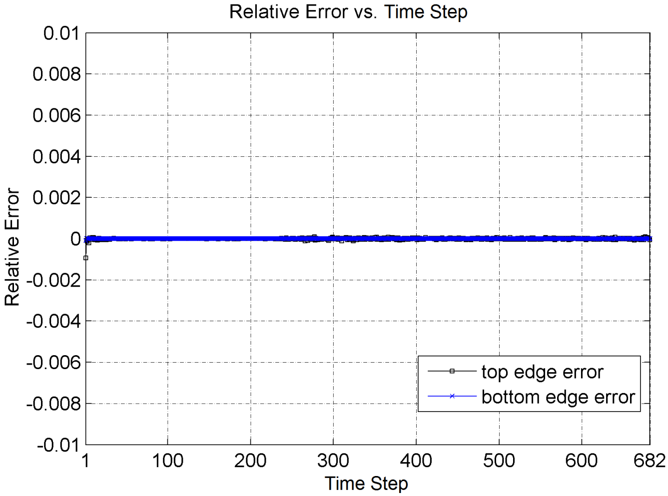

Figure 5.11: Load Relative Error - Analysis NA01 (ngd)

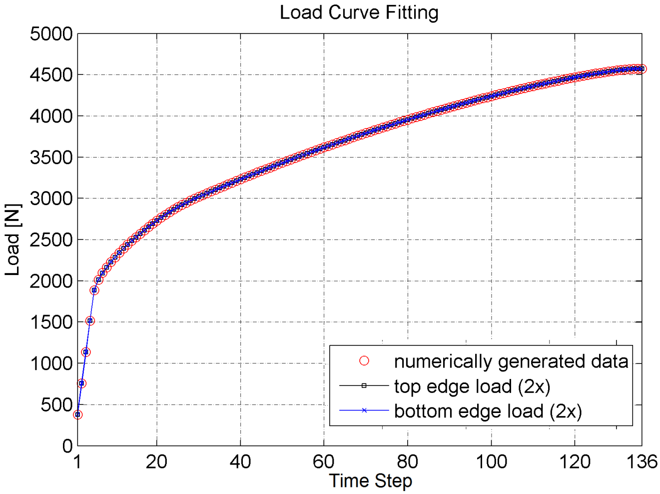

Figure 5.12: Load Curve Fitting - Analysis NA02 (ngd)

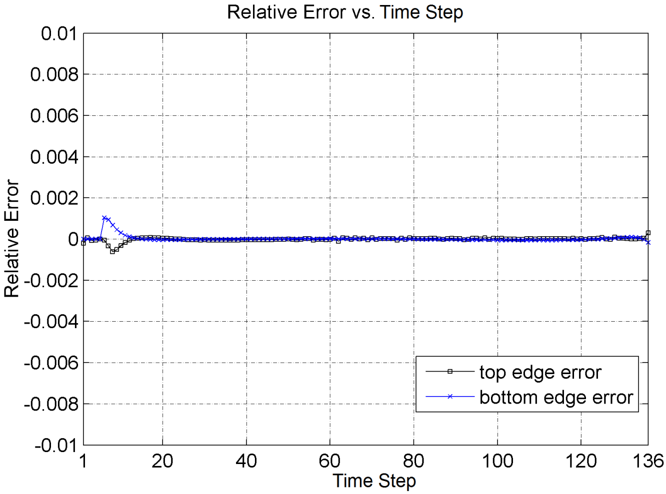

Figure 5.13: Load Relative Error - Analysis NA02 (ngd)

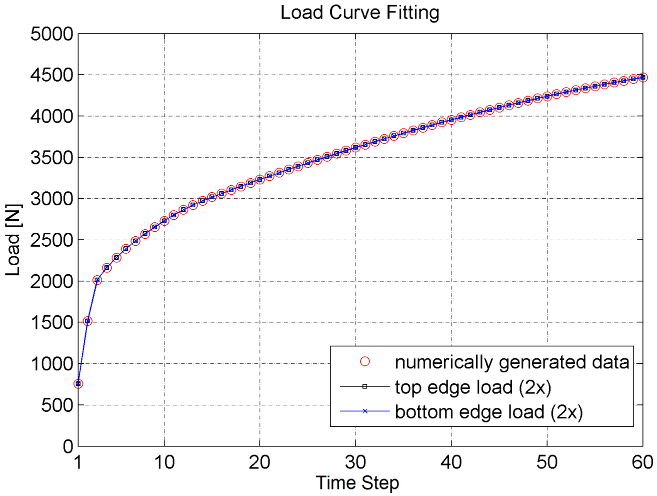

Figure 5.14: Load Curve Fitting - Analysis NA03 (ngd)

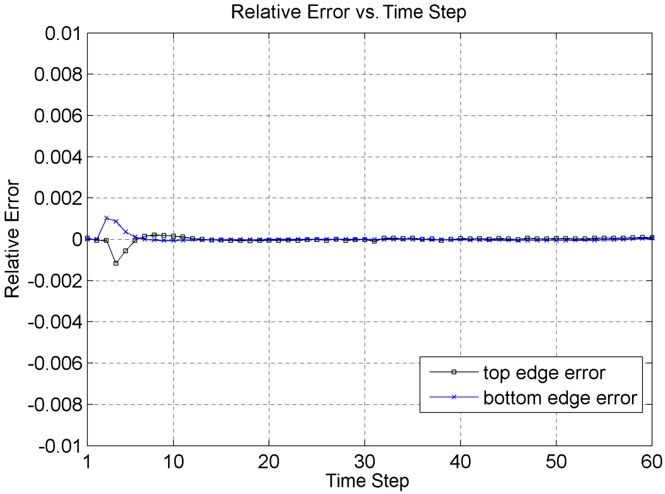

Figure 5.15: Load Relative Error - Analysis NA03 (ngd)

A second set of tests was then carried out, starting with non optimal initial points. In order to speed up the identification procedure, the cost functions were computed by using 136 time steps from the 682 available. As in the previous tests, the elastic coefficients and the yielding limit were considered as known and fixed: $(E, \nu, \sigma_{y0}) = (207000\text{ MPa}, 0.29, 165\text{ MPa})$.

Then, different minimum arguments of the objective function were evaluated. The first test (NA04 and NB04) was run in order to identify only the elastoplastic parameters (k, n), without considering damage effects. In this case, the objective function was computed by using the data of the first 100 time steps from those 136 (damage effects are expected to influence solely for high strain values). A second test (NA06 and NB06) was performed to identify only the damage parameters (r, S) by using the “converged” values (k, n) from the previous test. All 136 time steps were considered. Finally, the last test (NA05 and NB05) identified all the elastoplastic and damage parameters, also by using the data from all 136 time steps.

The summary of the initial values, their testing conditions, and unknown parameters are shown in Table 5.3.

Table 5.3: Initial guess and boundaries for unknowns variables (related to the second set of numerical tests)

Unknowns	Initial Value	Lower Boundary	Upper Boundary
k	100	50	500
n	1	0.1	500
r	1	0.1	10
S	0.1	0.1	10

The three testing conditions with random initial values were evaluated with both proposed objective functions. The results are shown in Table 5.4. It is possible to see that the best results were achieved for both objective functions when all variables (k, n, r, S) are free to find their optimum point. As expected, this fact has implied higher computational costs. A possible optimal procedure may be a separate identification of plastic/damage parameters as a way to find a good initial point for a complete free search.

Figures from 5.16 to 5.25 display the resulting curves of force-displacement and error-displacement for all cases, each showing satisfactory results.

Table 5.4: Results of the parameter identification from numerical generated data (2).

Analysis	Type	Steps	k	n	r	S	Min.	Eval/Iter	Fig.
NA04	A	100	286.18	53.07	-	-	866	68/21	5.16
NA05	A	136	(286.18)	(53.07)	0.33	5.04	6741	121/17	5.18
NA06	A	136	300.80	49.84	0.30	3.87	26	353/63	5.20
NB04	B	100	286.52	52.99	-	-	2127	62/19	5.22
NB05	B	136	(286.52)	(52.99)	0.34	5.06	1671	129/17	5.24
NB06	B	136	300.84	49.83	0.30	3.87	18	437/80	5.26

Type - Objective function used according to description in Chapter 4.
Steps - Number of time-steps used from 136 available.
Min - Value of the objective function convergence.
Eval/Iter - Number of objective function evaluations and the total number of iterations for convergence.

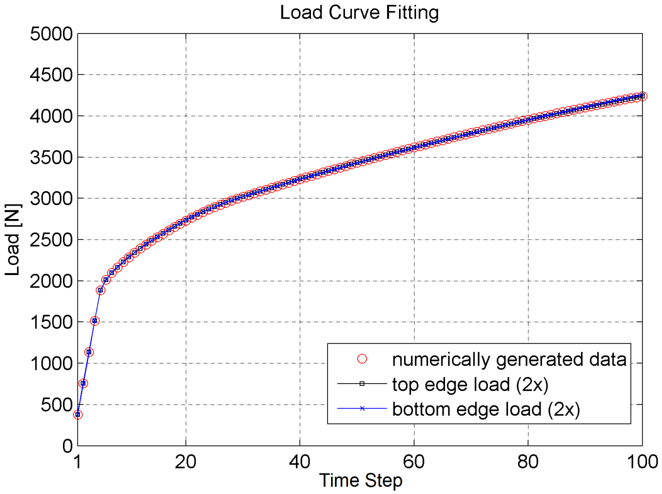

Figure 5.16: Load Curve Fitting - Analysis NA04 (ngd)

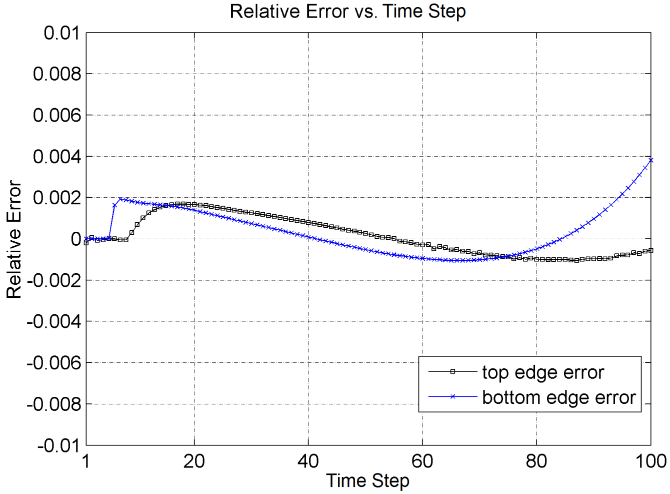

Figure 5.17: Load Relative Error - Analysis NA04 (ngd)

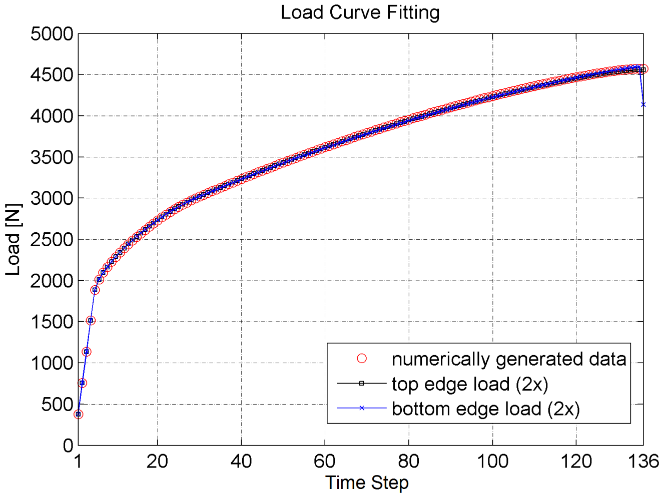

Figure 5.18: Load Curve Fitting - Analysis NA05 (ngd)

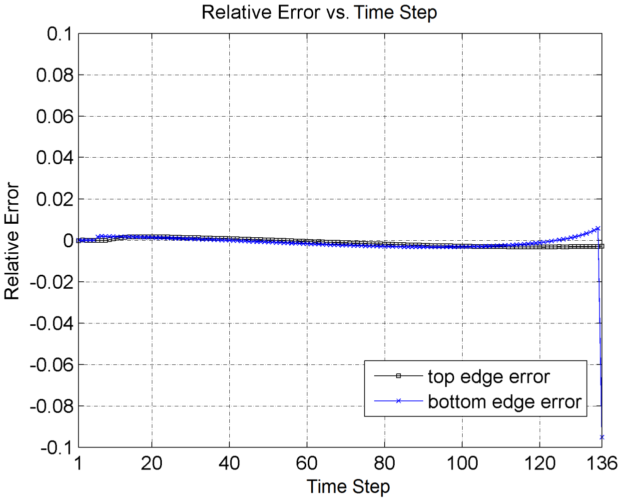

Figure 5.19: Load Relative Error - Analysis NA05 (ngd)

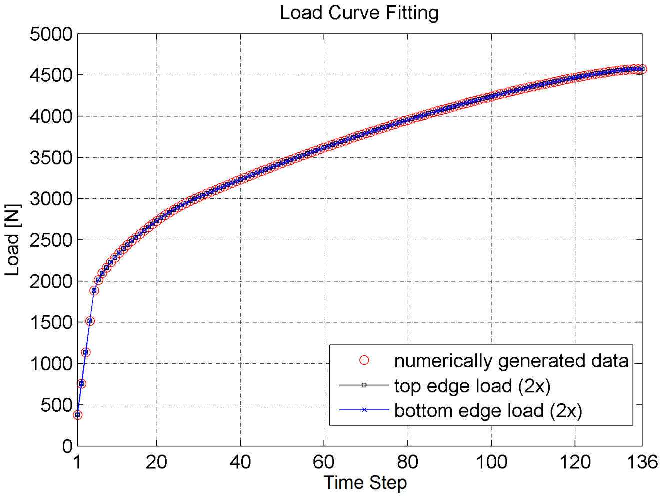

Figure 5.20: Load Curve Fitting - Analysis NA06 (ngd)

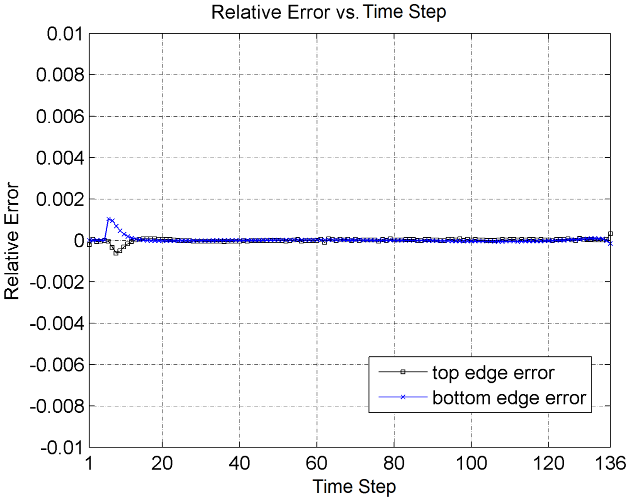

Figure 5.21: Load Relative Error - Analysis NA06 (ngd)

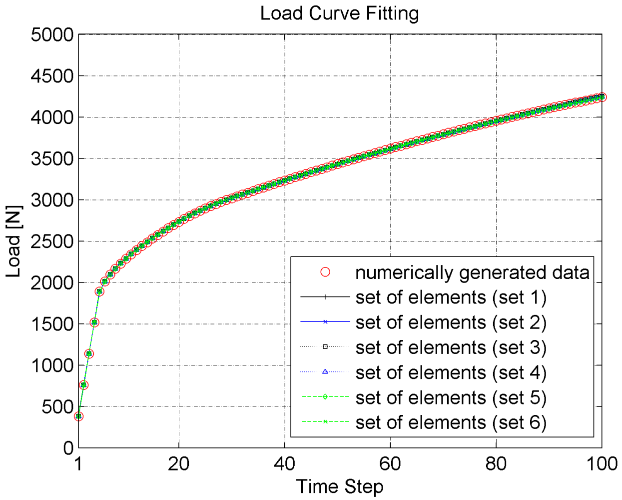

Figure 5.22: Load Curve Fitting - Analysis NB04 (ngd)

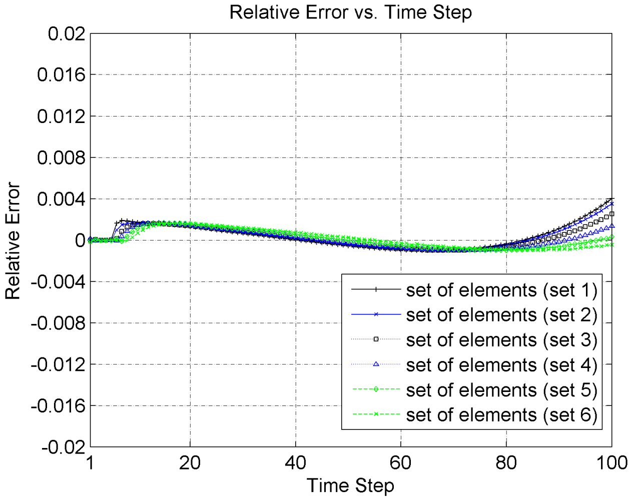

Figure 5.23: Load Relative Error - Analysis NB04 (ngd)

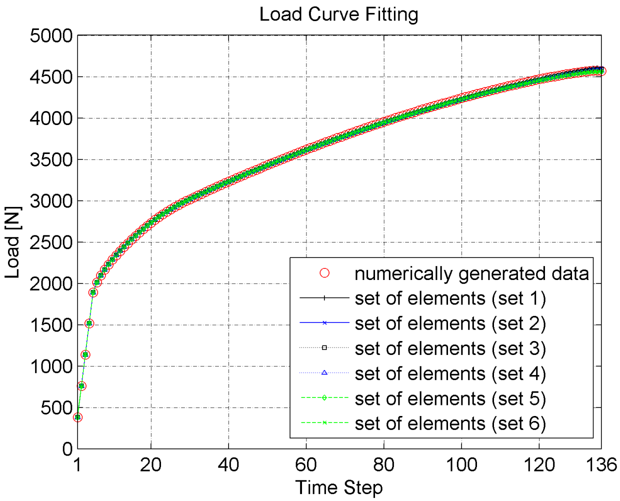

Figure 5.24: Load Curve Fitting - Analysis NB05 (ngd)

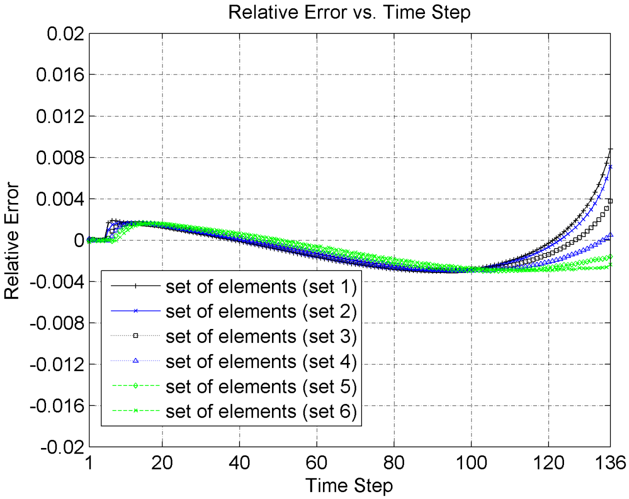

Figure 5.25: Load Relative Error - Analysis NB05 (ngd)

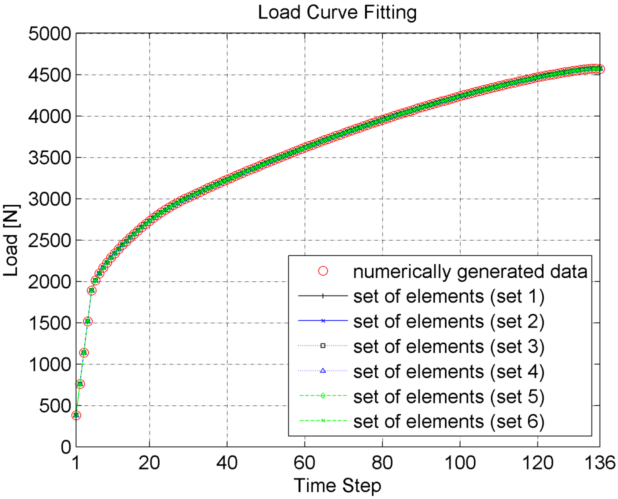

Figure 5.26: Load Curve Fitting - Analysis NB06 (ngd)

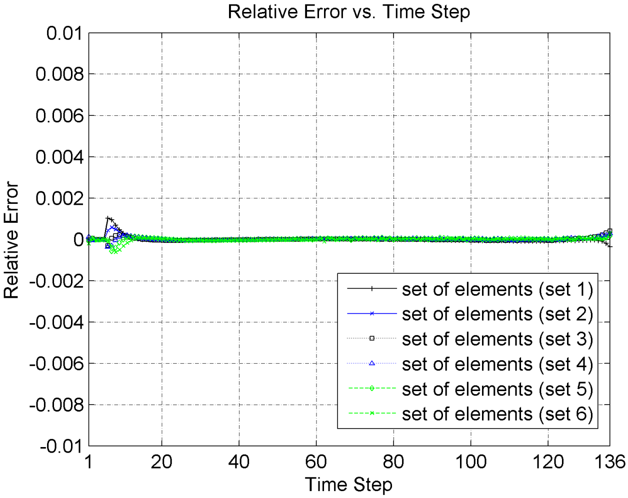

Figure 5.27: Load Relative Error - Analysis NB06 (ngd)

Once the mechanical test had been concluded and the necessary data had been recorded, image processing was carried out by means of DIC, providing the history of the displacement field. The load history was recovered from load-cell registers.

Figure 5.28 shows the ROI and its optical grid for the DIC method. For the sake of simplicity, only a half of the specimen width was considered in order to define the grid. The corresponding 2-D FE mesh is displayed in Fig. 5.29. It is important to mention that the grid markers on the right border are not exactly localised on the edge of the specimen image. This fact causes a slight difference between the dimensions of the specimen and of the model. For instance, while the width of the smallest cross section of the specimen was 12.30 mm, in the model it was 11.80 mm. Such a difference was compensated for in calculations by using a geometric correction factor that is multiplied to the measured load. This factor takes into account the ratio between the corresponding areas of the real specimen and model.

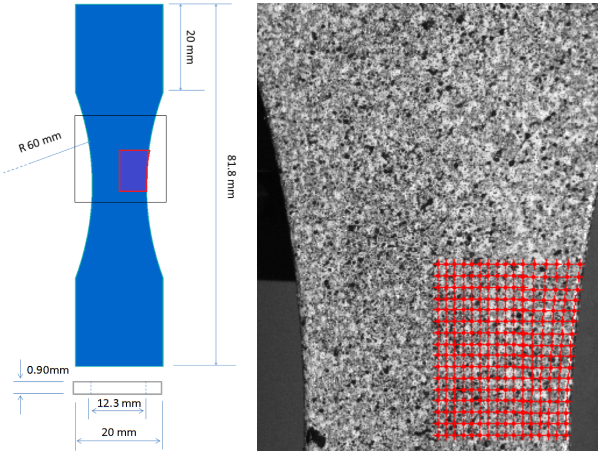

Figure 5.28: Definition of the ROI and the grid of markers for the experimental procedure.

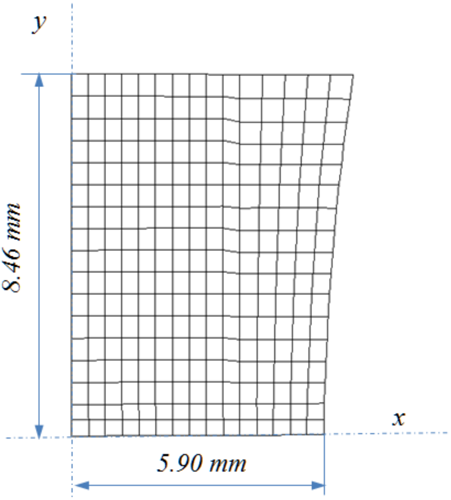

Figure 5.29: Mesh based on the DIC grid used in the procedure for identification of material parameters from experimental data (dimensions and system of coordinates).

It is well known that displacement fields that are measured by means of DIC may contain some noisy data, which requires an appropriate treatment to improve the identification procedure. Two approaches are employed to reduce noise and its undesirable consequences. The first is a proper adjustment of DIC apparatus (hardware) and configuration parameters (software) in order to obtain the best initial data. The second recommended step is to apply a smoothing technique to the noisy displacement field (filtering) before proceeding with the calculation of strains [33]. Several filtering techniques can be employed. In the current analysis, two procedures were sequentially applied to the displacement data. Firstly, the displacement of each marker was smoothed in time by using a moving least-square procedure. Once this procedure had been completed for all markers, a spatial smoothing was applied at each time step. This consisted of the following operations. Given a marker, the patch of elements attached to it is identified. Then, the displacement of the markers belonging to the patch is linearised by means of a least-square technique. Finally, the displacement of the given marker is reset to the value of the linearised function obtained at the marker position. This procedure is repeated for all markers at each time step. Further details of this smoothing technique can be found in Appendix B. Figures 5.30 shows the components of the smoothed displacement of the last time-step, while 5.31 shows the modulus of these displacement components in the reference, and also in the deformed configuration.

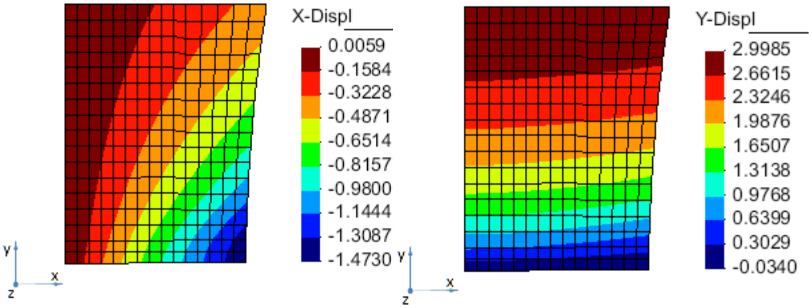

Figure 5.30: Displacement fields measured at the last time step of the mechanical test (u_x left and u_y right)[mm].

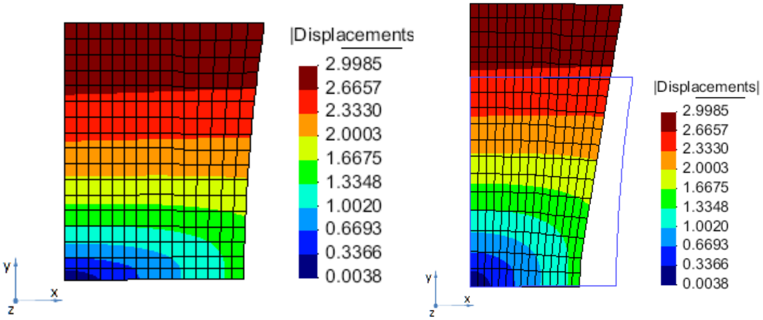

Figure 5.31: Displacement fields (modulus) measured at the last time step of the mechanical test (reference configuration at left and current configuration at right) [mm]

Based on the experimental data produced, two sets of identification tests were performed.

The first set dealt with the identification of the elastoplastic (no damage) parameters k, n by considering the smoothed and non-smoothed experimental data. Similarly, as in the tests reported in Section 5.1.2, only the first 100 time steps were taken into account when damage is not computed.

Both objective functions A and B were tested. The objective function A is defined according to Tables4.1 and 4.2 and considering the ROI shown in Fig. 5.29. The rows of elements/nodes corresponding to Objective Function B are shown in Fig. 5.32.

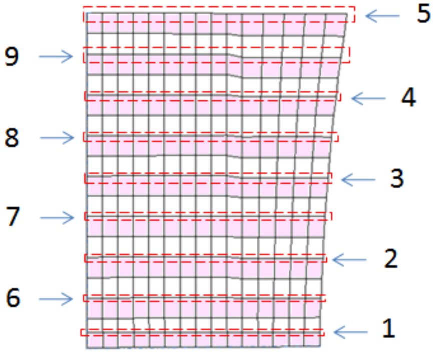

Figure 5.32: Set of elements/nodes related to the second proposal of objective function (objective function B) that were employed in the identification of material parameters from experimental data.

It is important to mention that the constitutive parameters (E,ν,σ_{y0}) are considered to be known variables. They were pre-determined by means of a standard uniaxial test performed according to ASTM E-8 [43], resulting in the following variables $(E,\nu,\sigma_{y0}) = (207000\text{ MPa}, 0.29, 165\text{ MPa})$.

The results are summarised in Table 5.5 for each case. Figures from 5.33 to 5.38 show the comparison between experimental and numerical curves, as well as the corresponding error for each test. By comparing Fig. 5.33 with both Fig.5.35 and Fig.5.37, one can clearly verify the influence of the smoothing process on the accuracy of the results.

Table 5.5: Results of the parameter identification from experimental data (1).

Analysis	Type	Smooth	Steps	k	n	r	S	Min.	Eval/Iter	Fig.
EA00	A	no	100	151.01	19.34	-	-	95.096×10^6	19/63	5.33
EA01	A	yes	100	138.12	28.62	-	-	658678	50/14	5.35
EB01	B	yes	100	138.22	30.70	-	-	882357	51/14	5.37

Type - Objective function used according to description in Chapter 4.
Steps - Number of time steps used from 130 available.
Min - Value of the objective function convergence.
Eval/Iter - Number of objective function evaluations and the total number of iterations for convergence.

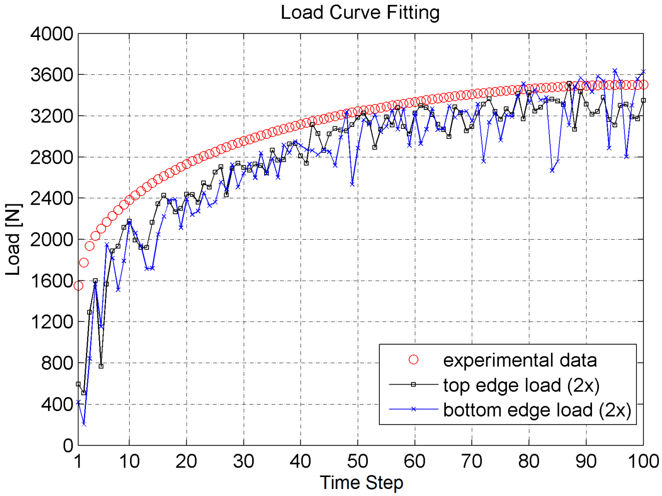

Figure 5.33: Load Curve Fitting - Analysis EA00 (Experimental Data)

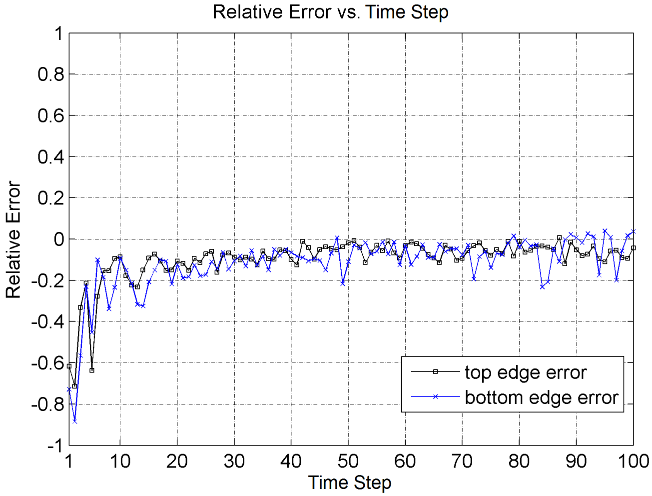

Figure 5.34: Load Relative Error - Analysis EA00 (Experimental Data)

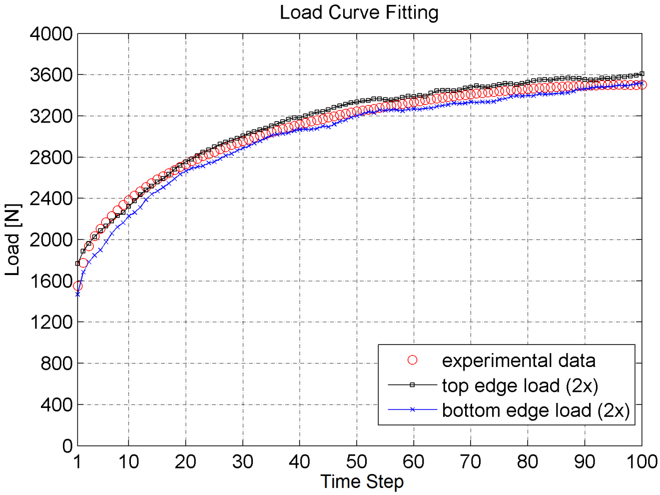

Figure 5.35: Load Curve Fitting - Analysis EA01
(Experimental Data)

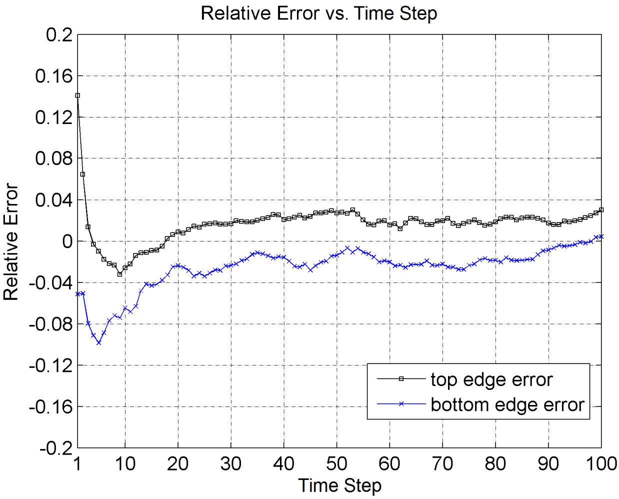

Figure 5.36: Load Relative Error - Analysis EA01
(Experimental Data)

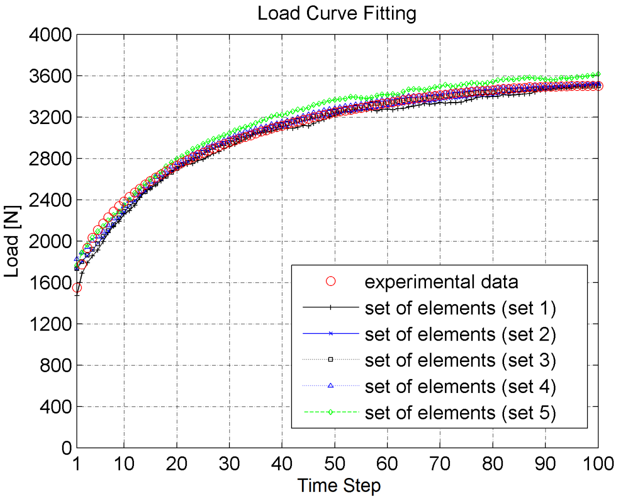

Figure 5.37: Load Curve Fitting - Analysis EB01 (Experimental Data)

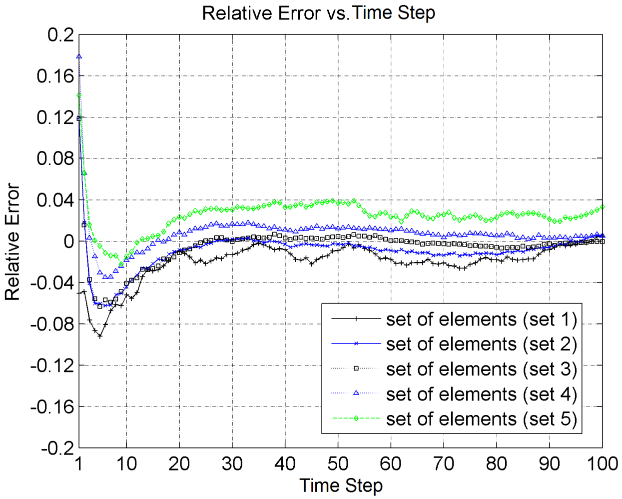

Figure 5.38: Load Relative Error - Analysis EB01 (Experimental Data)

The second set of tests introduced the evaluation of damage on the model and, therefore, the corresponding parameters to be identified. Firstly, a test was run, to search for the appropriate values (r, S) using the parameters (k, n) previously identified in tests EA01 and EB01. Secondly, an identification of all four parameters (k, n, r, S) was performed. The details of each test and the corresponding results are then summarised in table 5.6. Figures from 5.41 to 5.44 show the comparison between experimental and numerical curves as well as the associated error.

Table 5.6: Results of the parameter identification from experimental data (2)

Analysis	Type	Smooth	Points	k	n	r	S	Min.	Eval/Iter	Fig.
EA01	A	yes	100	138.12	28.62	-	-	658678	66/20	5.35
EA02	A	yes	130	(138.12)	(28.62)	5.25	0.69	1.843×10^6	95/12	5.39
EA03	A	yes	130	143.44	24.66	3.95	0.63	1.996×10^6	165/21	5.41
EB01	B	yes	100	138.22	30.70	-	-	882357	60/18	5.37
EB02	B	yes	130	(138.22)	(30.70)	8.06	0.78	1.987×10^6	132/25	5.43
EB03	B	yes	130	139.18	30.59	8.66	0.72	1.980×10^6	260/35	5.45

Type - Objective function used according to description in Chapter 4.
Steps - Number of time steps used from 130 available.
Min - Value of the objective function convergence.
Eval/Iter - Number of objective function evaluations and the total number of iterations for convergence.

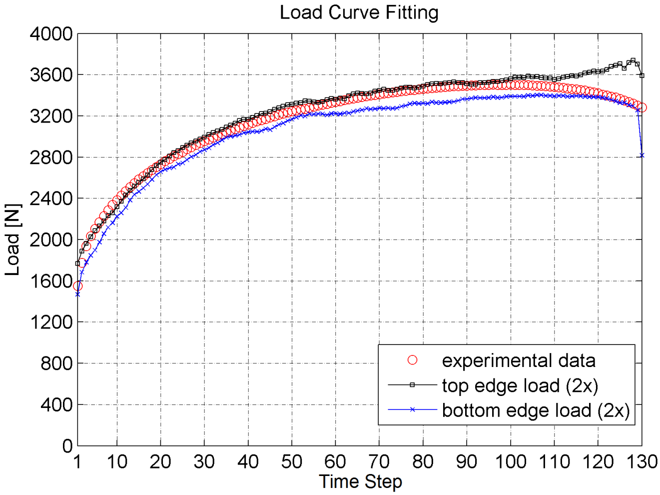

Figure 5.39: Load Curve Fitting - Analysis EA02 (Experimental Data)

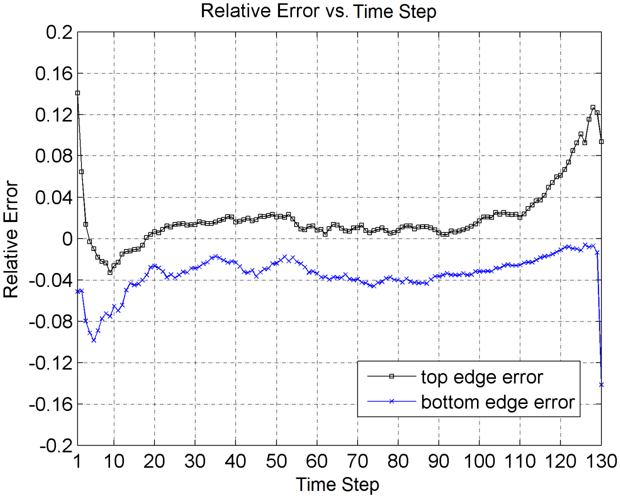

Figure 5.40: Load Relative Error - Analysis EA02 (Experimental Data)

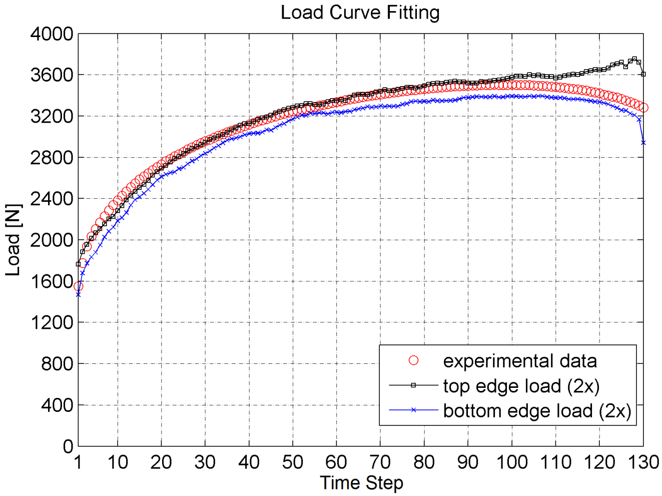

Figure 5.41: Load Curve Fitting - Analysis EA03 (Experimental Data)

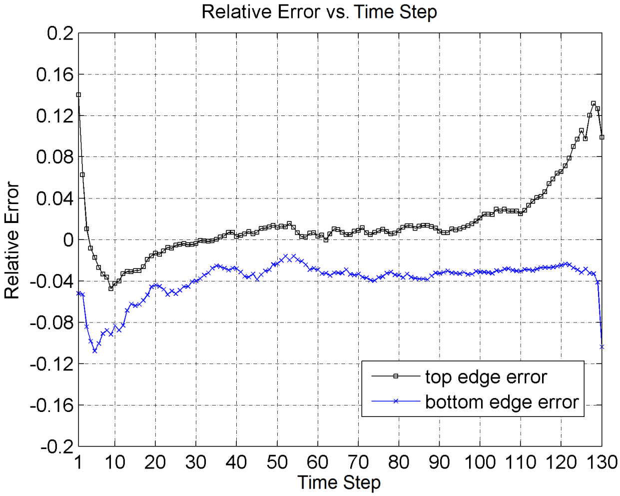

Figure 5.42: Load Relative Error - Analysis EA03 (Experimental Data)

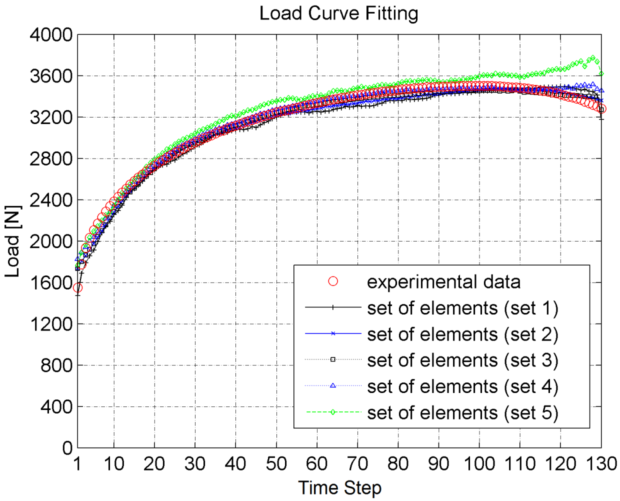

Figure 5.43: Load Curve Fitting - Analysis EB02 (Experimental Data)

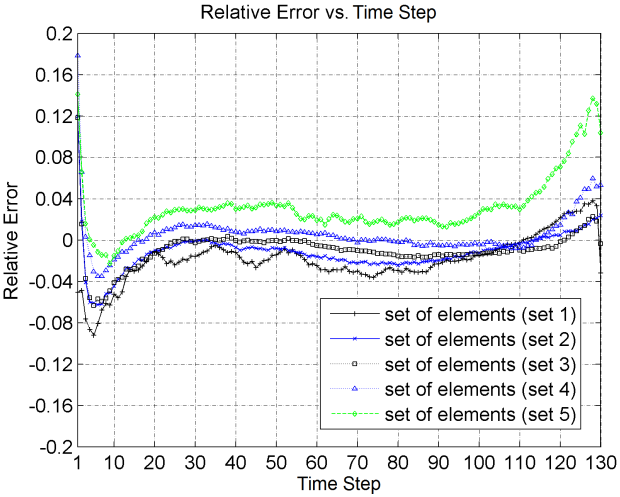

Figure 5.44: Load Relative Error - Analysis EB02 (Experimental Data)

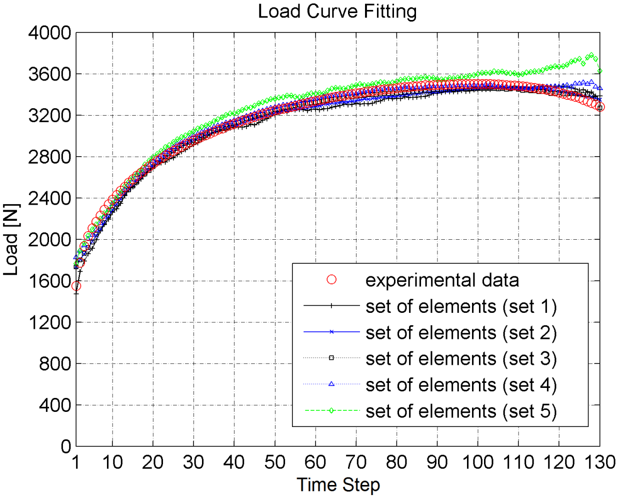

Figure 5.45: Load Curve Fitting - Analysis EB03 (Experimental Data)

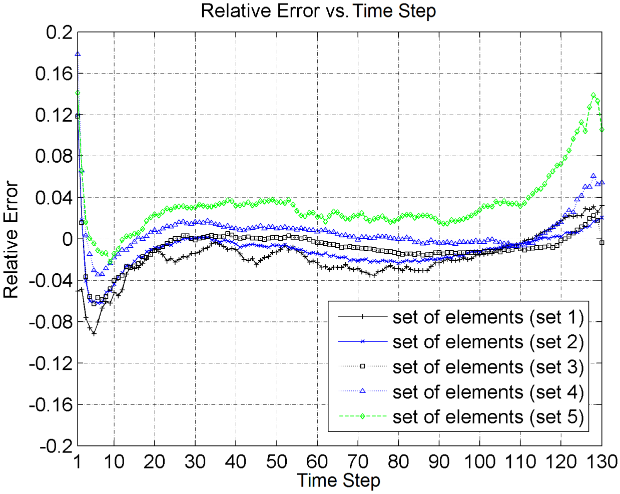

Figure 5.46: Load Relative Error - Analysis EB03 (Experimental Data)

5.3 FINITE ELEMENT ANALYSIS BASED ON THE IDENTIFIED PARAMETERS

In order to conclude the assessment of the proposed procedure, the parameters identified in section 5.2, analyses EA03 (set of parameters 1, Tab. 5.7) and EB03 (set of parameters 2, Tab. 5.7), were used in a complete incremental FE analysis, aiming to reproduce the mechanical tensile test. The same general conditions of the FE model used for the computation of internal forces during the identification process was applied to this simulation. This means the usage of a plane stress hypothesis, Lemaitre's elastoplastic damage model, and a linearised (infinitesimal) kinematics approach. The dimensions of the mesh were adjusted to those of the real specimen (the width of the smaller cross section was equal to 12.30 mm instead of the nominal 12.50 mm). The mesh and the boundary conditions are shown in Fig. 5.47.

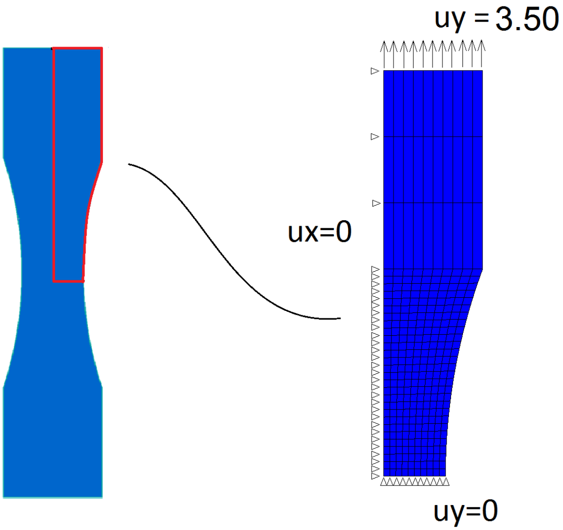

Figure 5.47: FE model used in the evaluation of the identified parameters.

Table 5.7: Set of identified parameters to be evaluated by means of an FE simulation.

Set of parameters	Analysis	k	n	r	S
1	EA03	143.44	24.66	3.95	0.63
2	EB03	139.18	30.59	8.66	0.72

The experimental and the simulated load-displacement curves are shown in Fig. 5.48, wherein a clear disagreement is noticed between them. A relative concordance appears for small displacement values even though it vanishes as soon as the axial displacement increases. This behaviour was surprising, since the agreement between the experimental forces and those computed during the identification procedure is clearly good, as shown in figures 5.35, 5.41, 5.39, 5.37, 5.45, 5.43 for different tests. It is at this point where the incompatibility between the measured displacement values and the linearised kinematics of the model may play a crucial role in explaining the difference between experimental and simulated curves. Although the parameters have been identified by using the same linearised kinematic model, it is suspected that the dimensional variations of the specimen (necking) are hardly handled by adjustments in the material parameters, leading to the discrepancies shown in Fig. 5.48.

The results that were obtained for the displacement field (y-direction), damage field, von Mises stress, the maximum principal strain and the z-component of the total strain are respectively shown in Fig. 5.49 Fig. 5.50, Fig.5.51, Fig. 5.52 and Fig. 5.53. All values are displayed for $u_y = 2.66$ mm (or equivalently 5.32 mm in the physical test).

Again, it is important to mention that these results carry a priori incompatibility of the chosen linearised kinematic approach with the finite deformation considered. From a qualitative viewpoint, a reasonable approximation is achieved, as shown in Fig. 5.54 for the damage distribution. In this figure, the damage field (left) indicates the point where the rupture (visible crack) started in the specimen (right).

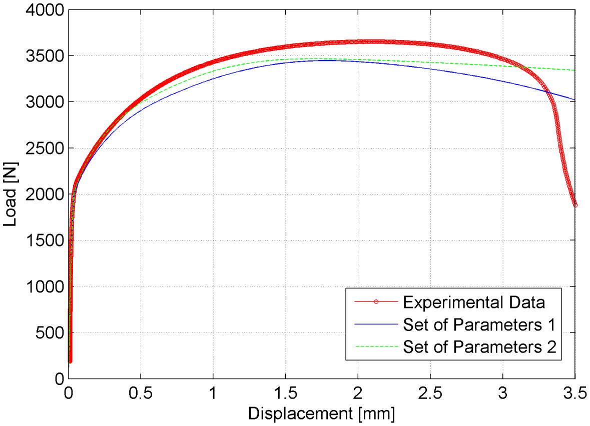

Figure 5.48: Load. vs. Disp. from an FE simulation based on the experimentally identified parameters of a low-carbon steel sample (plane stress FE model with damage).

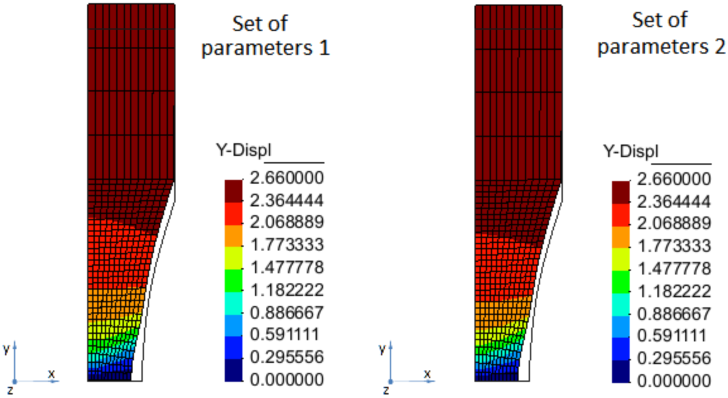

Figure 5.49: Displacement field y-direction [mm] from an FE simulation based on the experimentally identified parameters of a low-carbon steel sample (plane stress FE model with damage, displacement condition $u_y = 2.66$ mm)

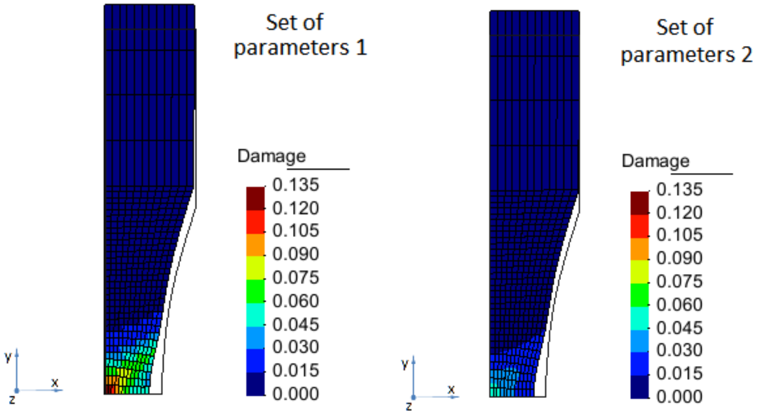

Figure 5.50: Damage field from an FE simulation based on the experimentally identified parameters of a low-carbon steel sample (plane stress FE model with damage, displacement condition $u_y = 2.66$ mm)

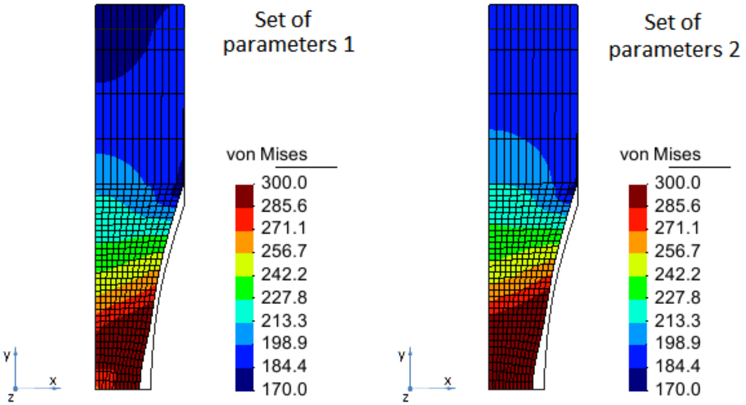

Figure 5.51: von Mises stress [MPa] from an FE simulation based on the experimentally identified parameters of a low-carbon steel sample (plane stress FE model with damage, displacement condition $u_y = 2.66$ mm)

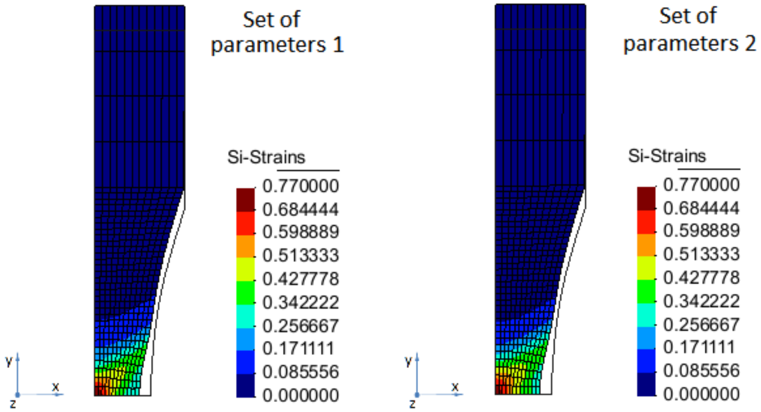

Figure 5.52: Maximum Principal Strain from an FE simulation based on the experimentally identified parameters of a low-carbon steel sample (plane stress FE model with damage, displacement condition $u_y = 2.66$ mm)

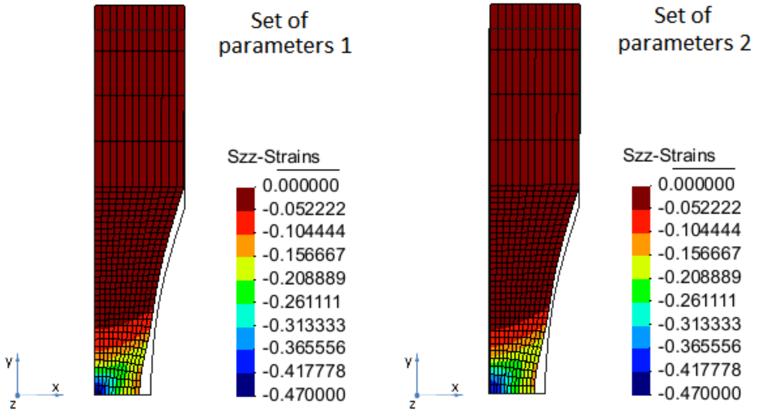

Figure 5.53: Total Strain - $\boldsymbol{\varepsilon}_z$ from an FE simulation based on the experimentally identified parameters of a low-carbon steel sample (plane stress FE model with damage, displacement condition $u_y = 2.66$ mm)

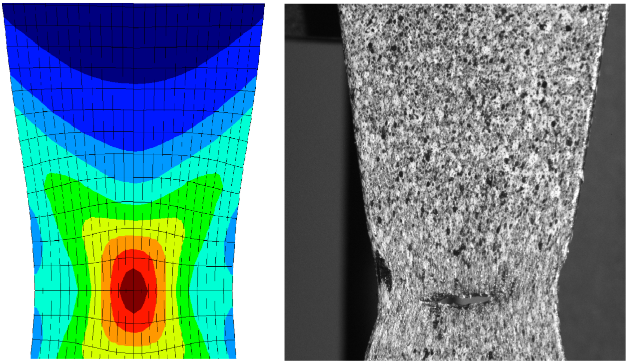

Figure 5.54: A qualitative comparison between the computed damage field and the initial crack observed on the specimen during the mechanical test.

6 CONCLUSIONS AND FINAL REMARKS

This dissertation was focused on the identification of constitutive parameters based on full-field measurements data. In order to fulfil the necessary understanding of the many subjects related to this kind of problem, a comprehensive range of topics has been studied. Firstly, a bibliographical review of several identification methods that employ full-field measurements has brought about a basic comprehension of such techniques, and allowed the proposal of a particular identification procedure. Furthermore, Lemaitre's elastoplastic damage constitutive model was studied and coded, which provided a consistent understanding of the process of formulating a constitutive model based on thermodynamics of internal variables. Additionally, the Digital Image Correlation (DIC) method was studied and employed as an efficient tool to measure full displacement fields. Finally, the proposed identification technique was coded and tested by means of several numerical and experimental examples, which provided a wide range of results that allowed the performance of the current proposition to be analysed.

At this point, some valuable remarks and conclusions can be inferred from the present work.

- Special attention must be paid when defining the DIC grid and markers, relating to the dimensional compatibility of the specimen with the FE model and selection of symmetry planes. This may avoid the the usage of additional adjustments and correction factors, which may be an inconvenient source of uncertainty.

- Although a reasonably good performance has been achieved with the optimisation algorithm used in this work (interior point method), other alternatives must be explored to minimise computational costs.

- The solution of Lemaitre's constitutive model is quite sensitive to the size of the load-step (time-step) increments and, therefore, small time steps are recommended, mainly when large strains are present. This implies that full-field data have to be provided for load increments as small as possible, in such cases.

- The identification results obtained with numerical generated data (ngd) were very successful, in the sense that the proposed algorithm was able to identify the constitutive parameters within an acceptable accuracy.

- When experimental data coming from DIC was used for the identification, the results of the optimisation process were comparably as good as those obtained with numerically generated data, in the sense that small values of the objective functions were obtained. However, the simulation of the whole process by means of the achieved parameters, still reproduced a numerical load curve with appreciable errors, with respect to the experimental one. This behaviour should be investigated in detail, although it is strongly suspected that the usage of an infinitesimal kinematic approach is the main cause of this behaviour.

- The smoothing operations on the experimental data obtained by DIC were essential for the good performance of the identification process. This is an important aspect to be considered and reviewed in further works, since the inappropriate usage of filtering/smoothing algorithms may result in the loss of important local information.

Based on the results achieved and on the previous remarks, the following proposals are pointed out as possible activities for future work:

- Formulation of the presented technique within the framework of finite deformations;

- Evaluation of different kinds of materials, for instance, polymeric ones, and usage of the corresponding constitutive models;

- Improvement of the numerical code in order to speed up the identification process;

- Use of 3-D full-field experimental data, and improvement of the 3-D identification code by using 3-D finite elements;

- Extend the identification procedure for cycled loads;

REFERENCES

[1] LEMAITRE, J. *A course on damage mechanics*. 2nd.. ed. [S.l.]: Springer-Verlag, 1996.

[2] LEMAITRE J. ; DESMORAT, R. *Engineering damage mechanics: ductile, creep, fatigue and brittle Failures.* [S.l.]: Springer-Verlag, 2005.

[3] AVRIL, S. et al. Overview of identification methods of mechanical parameters based on full-field measurements. *Experimental Mechanics*, Springer Boston, v. 48, p. 381–402, 2008.

[4] PAGNACCO, E. et al. Inverse strategy from displacement field measurement and distributed forces using fea. *In: 2005 SEM annual conference and exposition on experimental and applied mechanics*, 2005.

[5] VASSOLER, J.; FANCELLO, E. Identification of elastoplastic parameters under finite strain using a digital image correlation method. *Proceedings of COBEM 2011 21st International Congress of Mechanical Engineering Natal RN Brazil*, October 2011.

[6] FLORENTIN, E.; LUBINEAU, G. Identification of the parameters of an elastic material model using the constitutive equation gap method. *Computational Mechanics*, Springer Berlin / Heidelberg, v. 46, p. 521–531, 2010.

[7] FLORENTIN, E.; LUBINEAU, G. Using constitutive equation gap method for identification of elastic material parameters: technical insights and illustrations. *International Journal on Interactive Design and Manufacturing*, Springer Paris, p. 1–8.

[8] LATOURTE, F. et al. Elastoplastic behavior identification for heterogeneous loadings and materials. *Experimental Mechanics*, Springer Boston, v. 48, p. 435–449, 2008.

[9] GREDIAC, M.; TOUSSAINT, E.; PIERRON, F. Special virtual fields for the direct determination of material parameters with the virtual fields method. 2. application to in-plane properties. *International Journal of Solids and Structures*, v. 39, n. 10, p. 2707 – 2730, 2002.

[10] AVRIL, S. et al. Stress reconstruction and constitutive parameter identification in plane-stress elasto-plastic problems using surface measurements of deformation fields. *Experimental Mechanics*, v. 48, p. 403–419, 2008.

[11] GREDIAC, M.; PIERRON, F. Applying the virtual fields method to the identification of elasto-plastic constitutive parameters. *International Journal of Plasticity*, v. 22, n. 4, p. 602 – 627, 2006.

[12] CLAIRE, D.; HILD, F.; ROUX, S. Identification of damage fields using kinematic measurements. *Comptes Rendus Mecanique*, v. 330, n. 11, p. 729 – 734, 2002.

[13] CLAIRE, D.; HILD, F.; ROUX, S. A finite element formulation to identify damage fields: the equilibrium gap method. *International Journal for Numerical Methods in Engineering*, John Wiley & Sons, Ltd., v. 61, n. 2, p. 189–208, 2004.

[14] CLAIRE, D.; HILD, F.; ROUX, S. Identification of a damage law by using full-field displacement measurements. *International Journal of Damage Mechanics*, v. 16, n. 2, p. 179–197, April 2007.

[15] IKEHATA, M. Inversion formulas for the linearized problem for an inverse boundary value problem in elastic prospection. *SIAM Journal on Applied Mathematics*, Society for Industrial and Applied Mathematics, v. 50, n. 6, p. pp. 1635–1644, 1990.

[16] IKEHATA, M. An inverse problem for the plate in the love-kirchhoff theory. *SIAM Journal on Applied Mathematics*, Society for Industrial and Applied Mathematics, v. 53, n. 4, p. pp. 942–970, 1993.

[17] ABDA, A. B.; AMEUR, H. B.; JAOUA, M. Identification of 2d cracks by elastic boundary measurements. *Inverse Problems*, v. 15, n. 1, p. 67, 1999.

[18] BUI, H. D.; CONSTANTINESCU, A.; MAIGRE, H. Numerical identification of linear cracks in 2d elastodynamics using the instantaneous reciprocity gap. *Inverse Problems*, v. 20, n. 4, p. 993, 2004.

[19] NETO, E.; PERIC, D.; OWEN, D. R. *Computational methods for plasticity: Theory and applications.* [S.l.]: John Wiley & Sons, 2008.

[20] GURSON, A. L. Continuum theory of ductile rupture by void nucleation and growth: Part i—yield criteria and flow rules for porous ductile media. *Journal of Engineering Materials and Technology*, ASME, v. 99, n. 1, p. 2–15, 1977.

[21] TVERGAARD, V. Effect of yield surface curvature and void nucleation on plastic flow localization. *Journal of the Mechanics and Physics of Solids*, v. 35, n. 1, p. 43 – 60, 1987.

[22] ZHANG, Z. On the accuracies of numerical integration algorithms for gurson-based pressure-dependent elastoplastic constitutive models. *Computer Methods in Applied Mechanics and Engineering*, v. 121, p. 15 – 28, 1995.

[23] ZHANG, Z. Explicit consistent tangent moduli with a return mapping algorithm for pressure-dependent elastoplasticity models. *Computer Methods in Applied Mechanics and Engineering*, v. 121, p. 29 – 44, 1995.

[24] MALVERN, L. E. *Introduction to the Mechanics of a Continuous Medium*. Englewood Cliffs, New Jersey: Prentice-Hall, Inc., 1969. (Series in Engineering of the Physical Sciences).

[25] FREDERICK, C.; ARMSTRONG, P. A mathematical representation of the multiaxial bauschinger effect. *Materials at High Temperatures*, v. 24, n. 1, p. 1–26, 2007.

[26] JIANG, Y.; KURATH, P. Characteristics of the armstrong-frederick type plasticity models. *International Journal of Plasticity*, v. 12, n. 3, p. 387 – 415, 1996.

[27] SIMO, J.; HUGHES, T. *Computational Inelasticity*. [S.l.: s.n.], 1998.

[28] NETO, E. A. S. A fast, one-equation integration algorithm for the lemaitre ductile damage model. *Communications in Numerical Methods in Engineering*, John Wiley & Sons, Ltd., v. 18, n. 8, p. 541–554, 2002.

[29] FISH, J.; BELYTSCHKO, T. *A first course in finite elements*. [S.l.]: John Wiley & Sons, 2007.

[30] BONET, J.; WOOD, D. *Nonlinear continuum mechanics for finite element analysis*. [S.l.: s.n.], 2005.

[31] BELYTSCHKO, T.; LIU, W.; MORAN, B. *Nonlinear Finite Elements for Continua and Structures*. [S.l.: s.n.], 2005.

[32] COOK, R. D. et al. *Concepts and Applications of Finite Element Analysis*. [S.l.]: John Wiley & Sons, 2007. ISBN 0470088214.

[33] PAN, B. et al. Two-dimensional digital image correlation for in-plane displacement and strain measurement: a review. *Measurement Science and Technology*, v. 20, n. 6, p. 062001–, 2009.

[34] SUTTON, M. A.; ORTEU, J.-J.; SCHREIER, H. W. *Image Correlation for Shape, Motion and Deformation Measurements: Basic Concepts, Theory and Applications*. [S.l.]: Springer, 2009.

[35] BORNERT, M. et al. Assessment of digital image correlation measurement errors: Methodology and results. *Experimental Mechanics*, Springer Boston, v. 49, p. 353–370, 2009. ISSN 0014-4851.

[36] BING, P. et al. Performance of sub-pixel registration algorithms in digital image correlation. *Measurement Science and Technology*, v. 17, n. 6, p. 1615, 2006.

[37] VASSOLER, J. M.; FANCELLO, E. A. Error analysis of the digital image correlation method. *Mecánica Computacional*, XXIX, p. 6149–6161, Noviembre 2010.

[38] COPPIETERS, S. et al. Identification of the post-necking hardening behaviour of sheet metal by comparison of the internal and external work in the necking zone. *Journal of Materials Processing Technology*, v. 211, n. 3, p. 545 – 552, 2011.

[39] MATWORKS. *Constrained Nonlinear Optimization Algorithms: Optimization Algorithms and Examples MatLab R2012a Documentation*. Http://www.mathworks.com/help/toolbox/optim/ug/brnoxzl.html#brnpd5f Last Access: 05/14/2012.

[40] BYRD, R. H.; HRIBAR, M. E.; NOCEDAL, J. An interior point algorithm for large-scale nonlinear programming. *SIAM Journal on Optimization*, SIAM, v. 9, n. 4, p. 877–900, 1999.

[41] BYRD, R. H.; GILBERT, J. C.; NOCEDAL, J. A trust region method based on interior point techniques for nonlinear programming. *Mathematical Programming*, Springer Berlin / Heidelberg, v. 89, p. 149–185, 2000.

[42] WALTZ, R. et al. An interior algorithm for nonlinear optimization that combines line search and trust region steps. *Mathematical Programming*, Springer Berlin / Heidelberg, v. 107, p. 391–408, 2006.

[43] ASTM INTERNATIONAL. *ASTM E8M-04 Standard Test Methods for Tension Testing of Metallic Materials [Metric].*

APPENDIX A – APPARATUS FOR FULL-FIELD MEASUREMENTS

Figure A.1 shows the apparatus that was employed in this study in order to carry out the experimental procedures. One can see two CCD cameras and two auxiliary lighting sources that are properly assembled in a mechanical support. The CCD cameras are connected to a microcomputer wherein the DIC software is responsible for registering the tensile test images, as well as for post-processing them. The maximum resolution of the CCD camera is 1288x964 pixels. Figures A.2 and A.3 display respectively the painted specimen and after, when it is assembled to the tensile test machine.

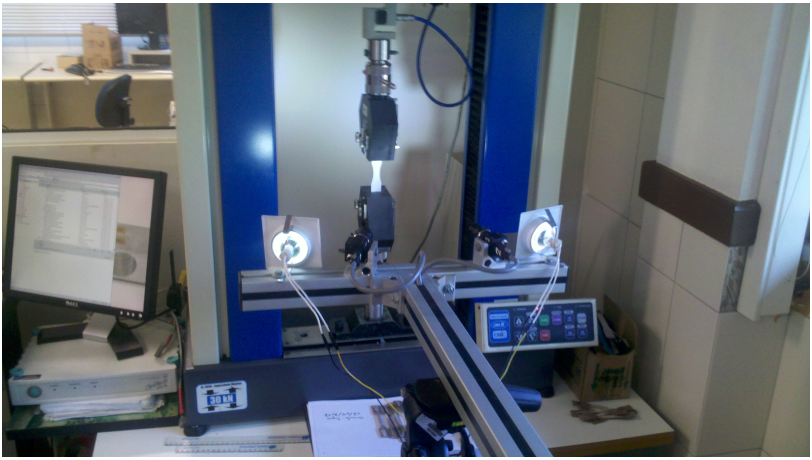

Figure A.1: The DIC apparatus and the test machine.

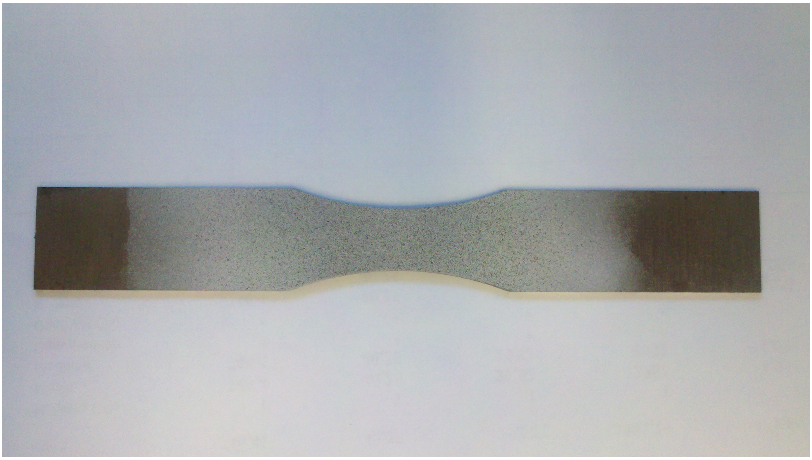

Figure A.2: Specimen used in the mechanical test and its texture after being painted by airbrush.

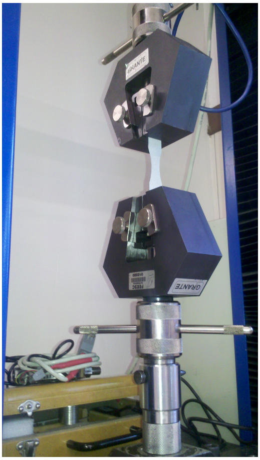

Figure A.3: Specimen after being assembled to the test machine.

APPENDIX B – TANGENT OPERATOR

According to [19, 28], the elastoplastic consistent tangent operator for the simplified version of Lemaitre's model is given by

$$\begin{aligned}\mathbf{D} =& c_1\, \mathbf{I}_{\mathrm{d}} + c_2\, \bar{\mathbf{s}}_{n+1} \otimes \bar{\mathbf{s}}_{n+1} + c_3\, \bar{\mathbf{s}}_{n+1} \otimes \mathbf{I} \\ &+ c_4\, \mathbf{I} \otimes \bar{\mathbf{s}}_{n+1} + c_5\, \mathbf{I} \otimes \mathbf{I}\,,\end{aligned} \tag{B.1}$$

where $\bar{\mathbf{s}}_{n+1}$ is the normalised stress deviator, i.e

$$\bar{\mathbf{s}}_{n+1} = \frac{\mathbf{s}_{n+1}}{\|\mathbf{s}_{n+1}\|}\ , \tag{B.2}$$

and c_1, c_2, ..., c_5 are scalar values which are calculated from the converged variables $(\cdot)_{n+1}$ as follows:

$$\begin{aligned} c_1 &= \frac{2G\, \omega_{n+1}\, \sigma_y(\breve{\varepsilon}^p_{n+1})}{\tilde{q}^{trial}_{n+1}} \\ c_2 &= 2G \left(a_1\, H\, \omega_{n+1} + a_4\, \sigma_y(\breve{\varepsilon}^p_{n+1}) - \frac{\omega_{n+1}\, \sigma_y(\breve{\varepsilon}^p_{n+1})}{\tilde{q}^{trial}_{n+1}} \right) \\ c_3 &= K\sqrt{\frac{2}{3}}\left[a_2\, H\, \omega_{n+1} + a_3 \sigma_y(\breve{\varepsilon}^p_{n+1})\right] \\ c_4 &= 2G\sqrt{\frac{3}{2}}\, \tilde{p}_{n+1}\, a_4 \\ c_5 &= K\left(\omega_{n+1} + a_3\, \tilde{p}_{n+1}\right) \end{aligned} \tag{B.3}$$

In B.3, the updated slope of the hardening curve is given by

$$H = \left.\frac{\mathrm{d}\sigma_y}{\mathrm{d}\breve{\varepsilon}^p}\right|_{\breve{\varepsilon}^p_{n+1}}\ . \tag{B.4}$$

And, the constants a_1, a_2, a_3, a_4 are defined as

$$\begin{aligned}
a_1 &= \frac{1}{F'}\left[\frac{\omega_{n+1}}{\tilde{q}^{trial}_{n+1}-\sigma_y(\breve{\varepsilon}^p_{n+1})}-\frac{1}{3G}\left(\frac{-Y_{n+1}}{\mathrm{r}}\right)^{\mathrm{S}}\right]\\
a_2 &= -\frac{\mathrm{S}\,\tilde{p}_{n+1}\left[\tilde{q}^{trial}_{n+1}-\sigma_y(\breve{\varepsilon}^p_{n+1})\right]}{3G\,\mathrm{r}\,K\,F'}\left(\frac{-Y_{n+1}}{\mathrm{r}}\right)^{\mathrm{S}-1}\\
a_3 &= a_2\,\omega'\\
a_4 &= a_1\,\omega'-\frac{\omega_{n+1}}{\tilde{q}^{trial}_{n+1}-\sigma_y(\breve{\varepsilon}^p_{n+1})}\;.
\end{aligned} \tag{B.5}$$

We also have that F' and ω' are respectively defined as

$$\begin{aligned}
F' =&\omega'-\frac{H}{3G}\left(\frac{-Y_{n+1}}{\mathrm{r}}\right)^{\mathrm{S}}\\
&+\frac{\mathrm{S}\,H\,\sigma_y(\breve{\varepsilon}^p_{n+1})\left[\tilde{q}^{trial}_{n+1}-\sigma_y(\breve{\varepsilon}^p_{n+1})\right]}{9G^2\mathrm{r}}\left(\frac{-Y_{n+1}}{\mathrm{r}}\right)^{\mathrm{S}-1}
\end{aligned} \tag{B.6}$$

$$\omega' = \frac{3G+\omega_{n+1}H}{\tilde{q}^{trial}_{n+1}-\sigma_y(\breve{\varepsilon}^p_{n+1})} \tag{B.7}$$

And finally, the definitions of the deviatoric projection tensor $\mathbf{I}_{\mathrm{d}}$ and the second-order identity matrix $\mathbf{I}$ are respectively

$$\mathbf{I}_{\mathrm{d}} = \mathbf{I}_{\mathrm{S}} - \frac{1}{3}\mathbf{I}\otimes\mathbf{I}\,, \tag{B.8}$$

$$\mathbf{I} = \delta_{ij}\;, \tag{B.9}$$

where

$$(\mathbf{I}_{\mathrm{S}})_{ijkl} = \frac{1}{2}\left(\delta_{ik}\delta_{jl}+\delta_{il}\delta_{jk}\right)\;, \tag{B.10}$$

and δ_{ik} is the Krönecker delta

$$\delta_{ij} = \begin{cases} 0, \text{ if } i\neq j\\ 1, \text{ if } i=j\;. \end{cases} \tag{B.11}$$

APPENDIX C – SMOOTHING TECHNIQUES

C.1 TIME SMOOTHING OF DISPLACEMENTS

Let us define for each marker a sequence of points $\{s_k\} = \{(u_k,t_k)\}$ for $k = 1,2,...,N$, where N is the total number of time steps, and u_k is the displacement of the marker at the time t_k. Then, let us consider s_n a subsequence of s_k, being n the number of elements in s_n. Let n be an odd number, $n \leq N$. For each set s_n, we can write an overdetermined linear system of the form

$$\begin{bmatrix} 1 & t_{k-j} \\ \vdots & \vdots \\ 1 & t_k \\ \vdots & \vdots \\ 1 & t_{k+j} \end{bmatrix} \left\{ \begin{array}{c} a_0^{(k)} \\ a_1^{(k)} \end{array} \right\} = \left\{ \begin{array}{c} u_{k-j} \\ \vdots \\ u_k \\ \vdots \\ u_{k+j} \end{array} \right\} , \tag{C.1}$$

where k indicates the central element of s_n; j is defined as $j = \frac{n-1}{2}$; and $a_0^{(k)}$, $a_1^{(k)}$ are unknown linear coefficients. Solving this system through a linear least-square scheme, we can compute

$$u_k^\star = a_0^{(k)} + a_1^{(k)} t_k \ , \tag{C.2}$$

where $u_k^\star$ is the smoothed value of u_k. Thus, once a value has been established for n, $u_k^\star$ is computed for each point $\frac{n-1}{2} < k < \left(N - \frac{n-1}{2}\right)$, which leads to the smoothed value for each u_k within this interval. Furthermore, in cases where $k \leq \frac{n-1}{2}$, we make $n = 2$ for $k = 1$; and $n = (2k-1)$ for $1 < k \leq \frac{n-1}{2}$. And, in cases where $k \geq \left(N - \frac{n-1}{2}\right)$, we make $n = 2(N-k)+1$ for $\left(N - \frac{n-1}{2}\right) \leq k < N$, and $n = 2$ for $k = N$. Solving the system for these last conditions, we complete the smooth for each sequence s_k.

Taking $n = 9$, the smoothing procedure was carried out for all markers, which led to a first set of smoothed data. Figure C.1 illustrates the local fitting for a single marker at time $t_{k=78} = 124.80$s, i.e. the time corresponding to the 78th time step. Moreover, Figure C.2 shows the final smoothing curve within the interval of time of $t_{k=69} = 110.4$s up to $t_{k=83} = 139.20$s; and lately Figure C.3 presents the complete smoothed curve.

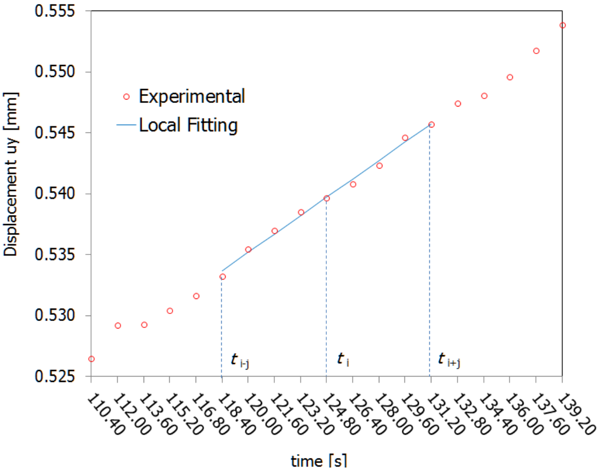

Figure C.1: Illustration of the local fitting applied to the displacement of a selected marker, aiming at the time smoothing of displacements.

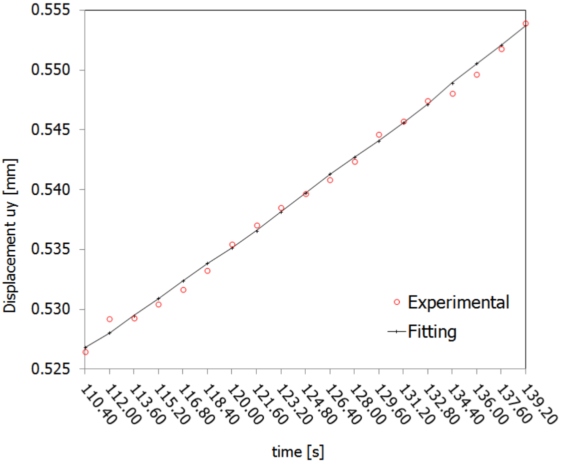

Figure C.2: Example 1: illustration of the global fitting applied to the displacement of a selected marker, aiming at the time smoothing of displacements.

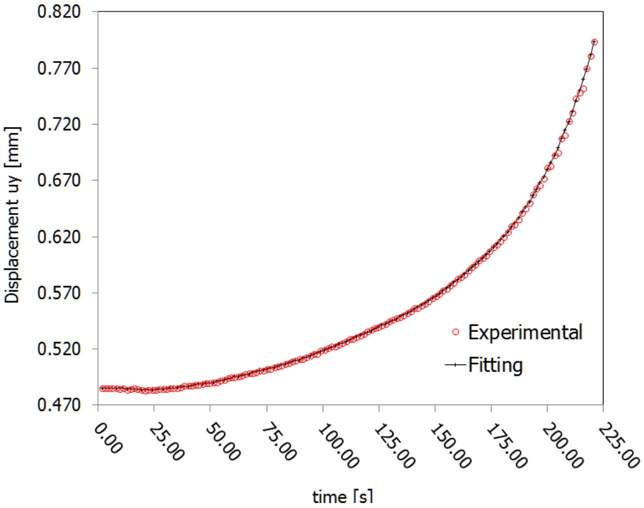

Figure C.3: Example 2: illustration of the global fitting applied to the displacement of a selected marker, aiming at the time smoothing of displacements.

C.2 DISPLACEMENT FIELD SMOOTHING

In this section the procedure used for smoothing the displacement field at each time step is presented. Let us consider a mesh containing only quadrilateral defined by a grid of markers provided by DIC (Fig. C.4). Furthermore, let us classify the markers as shown in Fig. C.4. There, χ_9[1] represents the sets in central positions that are formed with 9 markers, χ_6 are the sets on the edges that are formed with 6 elements and finally χ_4 are the sets at the corners of the mesh that are formed with 4 elements.

Starting with those sets of markers in central positions χ_9, we can write

---

[1] $\chi_n$are sets of nodes defined in a grid of markers, where n is the number of nodes in the set.

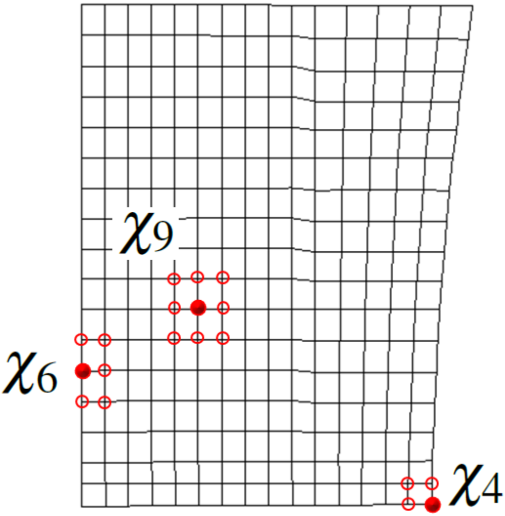

Figure C.4: Sets of nodes χ_n defined in a grid of markers aiming at the displacement field smoothing procedure.

$$\begin{bmatrix} 1 & x_{(i-1,j-1)} & y_{(i-1,j-1)} \\ 1 & x_{(i+1,j-1)} & y_{(i+1,j-1)} \\ 1 & x_{(i+1,j+1)} & y_{(i+1,j+1)} \\ 1 & x_{(i-1,j+1)} & y_{(i-1,j+1)} \\ 1 & x_{(i,j)} & y_{(i,j)} \\ 1 & x_{(i,j-1)} & y_{(i,j-1)} \\ 1 & x_{(i+1,j)} & y_{(i+1,j)} \\ 1 & x_{(i,j+1)} & y_{(i,j+1)} \\ 1 & x_{(i-1,j)} & y_{(i-1,j)} \end{bmatrix} \begin{Bmatrix} a_0 \\ a_1 \\ a_2 \end{Bmatrix} = \begin{Bmatrix} u_{(i-1,j-1)} \\ u_{(i+1,j-1)} \\ u_{(i+1,j+1)} \\ u_{(i-1,j+1)} \\ u_{(i,j)} \\ u_{(i,j-1)} \\ u_{(i+1,j)} \\ u_{(i,j+1)} \\ u_{(i-1,j)} \end{Bmatrix} \tag{C.3}$$

where i and j are indices that indicate the position of the marker within the mesh, being (i,j) the position of the markers to be evaluated, x and y are the coordinates of each marker, u is the corresponding displacement, and the coefficients a_0, a_1 and a_2 are unknowns. Solving this overdetermined system through a linear least-square scheme, we can compute

$$u^{\star}_{(i,j)} = a_0 + a_1 x_{(i,j)} + a_2 y_{(i,j)} \ , \tag{C.4}$$

where $u^{\star}_{(i,j)}$ is the smoothed value of $u_{(i,j)}$. Repeating this procedure for each set of markers χ_9, we obtain the smoothed field related to the central region of the mesh. Following a similar operation in order to establish the overdetermined systems related to those sets of markers on the edges χ_6 and at the corners χ_4, we can compute the smoothed full displacement field for a single time step. Finally, we conducted such calculations for all time steps, which generated the overall smoothed data to be employed in the identification procedure.

APPENDIX D – RESUMO ESTENDIDO (EM PORTUGUÊS)

Neste apêndice, descreve-se de forma sucinta o texto da presente dissertação, fazendo-se as devidas referências aos capítulos e seções que compõem o trabalho. Sempre que necessário, são indicadas as figuras, tabelas e equações para uma melhor compreensão do texto.

D.1 INTRODUÇÃO (CAPÍTULO 1)

O presente trabalho apresenta uma proposta de um método particular para a identificação de parâmetros constitutivos. Tal método faz uso de dados de medição de campos de deslocamentos obtidos por meio da técnica de Correlação de Imagens Digitais (do inglês: *Digital Image Correlation*, DIC). Deformações elásticas e plásticas, bem como o dano elastoplástico [1, 2, 19] são os fenômenos mecânicos em foco.

D.1.1 Identificação de parâmetros de material

Diferentes tipos de abordagem podem ser utilizados na identificação de paramâtros de material. Tais técnicas são comumente designadas como técnicas de solução para o problema inverso. O processo de identificação é usualmente realizado através da minimização de uma função objetivo, função essa que considera a diferença (erro) entre valores calculados numericamente e aqueles obtidos experimentalmente. Diversas técnicas que empregam dados de medição de campos de deslocamentos podem ser encontradas na literatura. As técnicas mais usuais estão listadas a seguir.

D.1.1.1 Métodos de identificação baseados em medições de campos de deslocamento

O artigo [3] traz uma revisão dos principais métodos de identificação baseados em medições de campos de deslocamentos. Abaixo, estão relacionados alguns desses métodos e referências bibliográficas complementares.

1. Método da Atualização do Modelo de Elementos Finitos
   (Finite Element Method Update, [4, 5])
2. Método da Diferença de Equações Constitutivas
   (Constitutive Equation Gap Method, [6, 7] [8])
3. Método de Campo Virtual
   (Virtual Filed Method, [9, 10, 11])
4. Método da Diferença de Equilíbrio
   (Equilibrium Gap Method, [12, 13, 14])
5. Método da Diferença de Reciprocidade
   (Reciprocity Gap Method, [15, 16, 17, 18])

Ressalta-se que os termos que descrevem os métodos acima ainda não se encontram completamente consolidados, podendo assim, sofrer variações e diferenças de tradução para o português.

Com o intuito de abranger as diversas áreas de conhecimento envolvidas neste trabalho, o mesmo apresenta dois capítulos de fundamentação, sendo esses relacionados respectivamente à Mecânica do Dano (Capítulo 2) e ao método de Correlação de Imagens Digitais (Capítulo 3). Então, na sequência, é apresentada uma proposta de método para identificação de parâmetros constitutivos (Capítulo 4). O capítulo de resultados (Capítulo 5) mostra o desempenho e aplicabilidade do procedimento descrito no capítulo que o antecede. Finalmente, o último capítulo (Capítulo 6) apresenta as vantagens, dificuldades e as possibilidades para trabalhos futuros. Uma breve explanação de cada um dos capítulos mencionados acima é apresentada a seguir.

D.2 MECÂNICA DO DANO (CAPÍTULO 2)

O fenômeno de dano é descrito como aquele relacionado à criação e crescimento de microvazios e microtrincas em um meio sólido resultando na redução da capacidade do corpo de suportar as solicitações as quais está submetido [19]. Os modelos para dano são uma opção a ser considerada quando se pretende abordar a problemática que envolve a variação das propriedades do material e sua degradação em decorrência de um determinado tipo de solicitação e mecanismo de falha. Diferentes tipos de dano podem então ser identificados, tais como: dano dúctil; dano frágil (ou quase-frágil); dano por fluência e dano por fadiga de baixo ou alto ciclo [1, 2]. Neste trabalho, cencentra-se a atenção para o caso de dano dúctil.

Dentro do contexto da modelagem computacional e relações constitutivas, é possível identificar diferentes modelos para tratar tal fenômeno. O processo de danificação está sempre associado a mecanismos irreversíveis. Como consequência, o tratamento matemático dado às relações constitutivas que envolvem dano se dá através de princípios termodinâmicos e do uso de variáveis internas, que descrevem o histórico do processo de deformação, considerando os aspectos dissipativos envolvidos. Entre diversas possibilidades, o modelo de Lemaitre para dano elastoplástico foi o modelo constitutivo escolhido para o desenvolvimento do presente estudo. Esse modelo se fundamenta em conceitos como área efetiva, tensão efetiva e na hipótese de deformação equivalente. Essa hipótese, tal como enunciada em [19], afirma que a deformação de um material com dano pode ser representada pelas equações constitutivas do material virgem através da substituição da tensão real pela tensão efetiva. Desta forma, apresenta-se a formulação do modelo constitutivo de Lemaitre para o caso de deformações infinitesimais e seu respectivo algoritmo de integração (seções 2.1, 2.2 e 2.2.1), tal como descrito em [19]. Além disso, apresenta-se a versão simplificada do modelo, na qual são desconsideros efeitos de encruamento cinemático (seções 2.3 e 2.3.1). A versão simplificada foi a versão utilizada neste trabalho.

D.3 CORRELAÇÃO DE IMAGENS DIGITAIS (CAPÍTULO 3)

O método de correlação de imagens digitais é um método de medição não intrusiva (sem contato) que se baseia em princípios ópticos, sendo empregado na medição de movimento e/ou deformação de um objeto por meio do processamento de uma sequência de imagens digitais desse objeto, onde cada imagem dessa sequência registra o estado de deformação do objeto ao longo do tempo. O método DIC tem sido usado especialmente na substituição de técnicas de medição pontuais, tais como as tradicionais técnicas de extensometria.

Ao se empregar o método DIC, é usual utilizar-se espécimes dos quais a superfície apresente uma textura cuja imagem resulte em uma distribuição randômica de escalas de cinza (Fig. 3.1). Além disso, é comum estabelecer uma região de interesse (do inglês: *region of interest*, ROI) para que sejam efetuadas as devidas medições de deslocamentos. Nessa região, define-se uma grade de pontos (marcadores), os quais serão pontos de referência para o cálculo dos campos de deslocamentos (Fig. 3.2). Para uma melhor compreensão, considere duas imagens de um ROI, antes e depois de ser deformado (Fig. 3.3). Para cada marcador da imagem indeformada, é definido um subconjunto de pixels, tendo como centro o próprio marcador. Esse subconjunto de pixels, que é caracterizado por uma distribuição própria de escalas de cinza, irá ocupar uma nova posição na imagem deformada. Então, pelo método de correlação de imagens digitais, procura-se pelo mapeamento que permita correlacionar a distribuição de cinza da primeira imagem com a da segunda. O procedimento de correlação é realizado por meio de um processo de otimização que procura os devidos parâmetros de mapeamento para cada subconjunto de pixels, por meio da minimização (ou maximização) de um critério de correlação (função de correlação). Desta forma, uma vez estabelecido tal mapeamento, é possível então obter o vetor deslocamento relacionado a cada marcador, e por conseguinte, o campo de deslocamento na região desejada.

D.4 IDENTIFICAÇÃO DE PARÂMETROS DE MATERIAL A PARTIR DE DADOS ÓPTICOS (CAPÍTULO 4)

No Capítulo 4, descrito nesta seção, é apresentado uma proposta de um método para identificação de parâmetros de material. Esse método pode ser classificado como um caso particular do método de campos virtuais, uma vez considerado o campo virtual $\delta\mathbf{u}$ da Eq. (1.4), como sendo aquele descrito pelas funções de forma de uma malha de elementos finitos, convenientemente definida em relação a uma grade de marcadores proveniente do método DIC. Essa proposta de identificação de parâmetros é similar àquela encontrada em [38]. Contudo, a versão aqui apresentada se diferencia pela forma como as funções objectivo são definidas.

D.4.1 Considerações iniciais sobre dados experimentais

Considere um espécime prismático e uma grade de pontos (marcadores) definida sobre a imagem frontal desse espécime (Fig. 4.1). Durante um ensaio mecânico, cada ponto dessa grade é rastreado por meio do método DIC, enquanto os dados de corregamento é simultaneamente registrado. Assim, obtém-se o histórico do campo de deslocamentos e o correnpondente histórico de carregamento. Desta forma, por meio da aplicação de uma hipótese apropriada, como por exemplo a de um estado plano de tensões, pode-se extrapolar os dados obtidos, referentes à superfície, para todo o volume do espécime.

D.4.2 Problema de minimização do erro

Considerando-se o problema de equilíbrio em sua forma fraca (Eq. 4.1), e tomando-se o campo de deslocamento $\mathbf{u} = \mathbf{u}^t$ como conhecido (campo medido experimentalmente), onde $\mathbf{u}^t$ corresponde à história do campo de deslocamento até o instante de tempo t, obtém-se respectivamente os trabalhos virtuais inteno (Eq. 4.2) e externo (Eq. 4.3). Fazendo $\delta\mathbf{u} = \mathbf{N}_i$, com $\mathbf{N}_i$, i=1,NDOF sendo as correspondentes funções de forma globais e NDOF o número de graus de liberdade devido à malha de elementos finitos, associada à grade de pontos fornecida pelo método DIC, e finalmente, pela substituição de $\delta\mathbf{u}$ em Eq. (4.2) e Eq. (4.3), obtém-se as equações residuais (4.4), (4.5), (4.6), respectivamente reproduzidas abaixo.

$$\mathbf{R}_i(\mathbf{u}^t) = \mathbf{F}_i(\mathbf{u}^t) - \mathbf{Q}_i(\mathbf{u}^t) = \mathbf{0}$$

$$\mathbf{F}_i(\mathbf{u}^t) = \int_{\Omega^t} \mathbf{B}_i^T \boldsymbol{\sigma}(\mathbf{u}^t)\, \mathrm{d}\Omega^t$$

$$\mathbf{Q}_i(\mathbf{u}^t) = \int_{\Omega^t} \mathbf{N}_i^T \mathbf{b}(\mathbf{u}^t)\, \mathrm{d}\Omega^t + \int_{\Gamma^t} \mathbf{N}_i^T \mathbf{f}(\mathbf{u}^t)\, \mathrm{d}\Gamma^t$$

onde a matrix $\mathbf{B}_i = \mathcal{D}\mathbf{N}_i$ contém as componentes de deformação associadas à função de forma $\mathbf{N}_i$; $\mathcal{D}$ é o operador deformação; e $\mathbf{F}_i$ e $\mathbf{Q}_i$ são as forças internas e externas do i-th DOF (grau de liberdade) das equações discretas de elementos finitos. O equacionamento acima leva ao vetor resíduo nulo $\mathbf{R}_i$, caso o equilíbrio seja satisfeito. Assim, o problema de identificação de parâmetros pode ser definido como a minimização de uma função objetivo Ψ, definida com base no resíduo proveniente do equilíbrio entre forças internas (calculadas) e externas (mensuradas). Então, temos Eq. (4.7)

$$\mathbf{p}^\star = \arg\min_{\mathbf{p}\in\mathcal{P}} \left\|\Psi(\mathbf{p};\mathbf{u}^t)\right\|^2$$

onde $\mathbf{p}$ é um vetor de parâmetros de material, os quais pertencem a um conjunto de valores admissíveis $\mathcal{P}$.

Por fim, escolhendo-se um conjunto apropriado de elementos e/ou nós, calculado-se as respectivas forças internas e o resíduo do erro entre carregamento externo e forças internas, pode-se propor formas variadas para função objetivo. Dois exemplos de função, denomindas função objetivo A (seção 4.2.1) e função objetivo B (seção 4.2.2), foram propostos.

No primeiro caso (função objetivo A), tomando o conjunto de nós mostrados na Fig. 4.2 e descritos na Tab. 4.1, mais as funções resíduo definidas na Tab. 4.2, teremos para cada passo de tempo a função Eq. (4.8), que é reproduzida a seguir:

$$\boldsymbol{\psi}^t = \sum_{i=1}^{n} \alpha_i^t \left\|\mathbf{R}_i^t\right\|^2$$

onde os termos α_i^t são pesos, e no caso exemplificado $n = 4$ (número de funções resíduo, Tab. 4.2).

Finalmente, teremos como função objetivo global a Eq. (4.9), i.e

$$\Psi = \sum_t \boldsymbol{\psi}^t$$

No caso da função objetivo B, segue-se procedimento similar ao adotado para a função A. Uma vez definidos os conjuntos de elementos/nós, tal como mostrado na Fig. 4.3, calcula-se a diferença entre a soma das forças internas para cada conjunto Γ^i (definido conforme Fig 4.3) em relação ao carregamento P^t medido experimentalmente. Assim, chega-se a Eq. (4.10):

$$\mathbf{R}_i^t = \left[\sum_{j=1}^{m} F_y^{(ij)}(\mathbf{u}^t)\right]_i - P^t$$

onde m é o número total de nós pertencentes à Γ^i. E mais uma vez, emprega-se as equações (4.8) e (4.9) no computo da função objetivo.

D.5 RESULTADOS (CAPÍTULO 5)

Na seção de resultados, relata-se o processo de avaliação do método de identificação de parâmetros proposto. O método foi avalido por meio de diversos testes numéricos e experimentais.

Iniciou-se o processo de avaliação por testes numéricos, a fim de se verificar o algoritmo proposto no Capítulo 5. Assim, em primeiro lugar, um modelo de elementos finitos foi elaborado, de tal forma que, por meio de uma simulação numérica de um ensaio de tração uniaxial de um corpo de prova não padronizado (Fig. 5.1), e utilizando-se parâmetros de um material hipotético, foi posssível gerar os dados de entrada necessários à execução do processo de identificação de parâmetros. Então, partindo-se desses dados gerados numericamente, realizou-se uma avaliação prévia do desempenho do algoritmo de identificação de parâmetros. Os resultados desta avaliação podem ser vistos nas tabelas (5.2) e (5.4), bem como, nas figuras de (5.10) à (5.15) e de (5.16) à (5.27). Os resultados baseados nos experimentos numéricos demonstraram a eficácia do método proposto.

Em uma segunda etapa, um teste mecânico de tração uniaxial foi realizado em um corpo de prova não padronizado de uma amostra de aço baixo-carbono, e através do método de correlação de imagens digitais, obteve-se o campo de deformação associado à região de interesse escolhida. Com base nos dados obtidos experimentalmente, prosseguiu-se com o processo de identificação de parâmetros do material. Os resultados obtidos estão apresentados nas tabelas (5.5) e (5.6), bem como nas figuras de (5.33) à (5.38), e de (5.39) à (5.46). Após concluido o processo de identificação, os parâmetros obtidos foram utilizados em uma simulação por elementos finitos no intuito de se reproduzir o teste de tração, e para se avaliar a qualidade dos parâmetros idetificados. A simulação do modelo de elementos finitos, baseada nos parâmetros obtidos, reproduziu a curva de carregamento com erros consideráveis, quando tal curva foi comparada à experimental. Suspeita-se fortemente que a origem desse problema esteja no uso da formulação infinitesimal.

D.6 CONCLUSÕES (CAPÍTULO 6)

Nesta dissetação foram abordados os seguintes tópicos:

- estudo de métodos de identificação baseado em medições de campos de deslocamento e/ou deformação;
- estudo da formulação e implementação de um modelo elastoplástico com dano;
- estudo do método de correlação de imagens digitais;
- proposta de um método de identificação de parâmetros de material;
- realização de um conjunto de testes numéricos e experimentais que proveram resultados importantes para a avaliação do método proposto.

Deste trabalho, extrai-se informações importantes, tais como:

- necessidade de atenção na definição da grade de marcadores e na escolha de planos de simetria;
- bom desempenho no processo de identificação por meio do método de otimização baseado em gradiente (ponto interior);
- sensibilidade do modelo de Lemaitre ao tamanho do incremento de carga;
- os resultados baseados em experimentos numéricos demonstraram a eficácia do método proposto;
- a simulação do modelo de elementos finitos, baseada nos parâmetros obtidos, reproduziu a curva de carregamento com erros consideráveis, quando tal curva foi comparada à experimental; suspeita-se fortemente que a origem desse problema esteja no uso da formulação infinitesimal;
- o uso de uma técnica de suavização foi essencial para o processo de identificação, contudo, deve-se ter atenção ao empregarmos tal procedimento, especialmente no que concerne à perda de informações locais.

Sugestões para trabalhos futuros:

- formulação baseada em deformações finitas;
- avaliação de outros tipos de materiais;
- melhoria do código para acelerar o processo de identificação;
- emprego de campos tridimensionais, bem como modelos de elementos finitos 3-D;
- estender o procedimento para uso em condições de carregamentos cíclicos.